Soft X-ray emissivity profile inversion in quasi-axisymmetric equilibria

Jonathan Rossel

February 2005

Supervisor: Jean-Marc Moret
Resp. professor: M. Q. Tran
Sciences de base
CRPP, EPFL

Contents

1 Abstract **5**

2 Introduction **7**
2.1 Basic phenomenology and theoretical background 7
2.1.1 Tokamak principle 7
2.1.2 X-ray emission in a tokamak plasma 9
2.1.3 Tomography inversion problem 9
2.1.4 MHD perturbations - Magnetic islands 11
2.2 The DMPX at TCV 13
2.3 Motivations, aims and objectives 15

3 Model of the magnetic islands and their emissivity **17**
3.1 Current perturbation 17
3.2 Reconstruction of the island geometry 18
3.3 Position of the magnetic islands 19
3.4 Time dependence of the perturbation 20
3.5 Emissivity function and island isolation 21
3.6 Summary of the model 25

4 Inversion method description **27**
4.1 Used tools 27
4.2 General approach 27
4.3 Signal pre-processing 27
4.4 Average filter 29
4.5 Bandpass filter 29
4.6 SVD filter 29
4.7 Time selection 29
4.8 Fourier transform filter 32
4.9 Stationary plasma profile inversion 32
4.9.1 Inversion procedure description 32
4.9.2 Modification of the equilibrium 33
4.10 Fit of the magnetic island parameters 35
4.10.1 General aspects 35
4.10.2 Inversion of SVD or bandpass signals 38
4.10.3 Inversion of signals in frequency space 41
4.10.4 Optimized interval of possible values of ρ_s 44
4.10.5 Optimized fit of the orientation in the case of SVD or bandpass signals 44
4.10.6 Determination of the width of the islands 44

4.10.7 Determination of the *rms* current perturbation 45
4.11 Phantom signal generator 46

5 Results and discussion **47**
5.1 Stationary profile inversion 47
5.1.1 Phantoms 47
5.1.2 Real signals 49
5.1.3 Discussion 52
5.2 Perturbation profile inversion 54
5.2.1 Phantoms 55
5.2.2 Assessment of the stability of the ρ_s search procedure . 58
5.2.3 Shot 22621 60
5.2.4 Shot 24141 64
5.2.5 Shot 27481 at 0.4 seconds 68
5.2.6 Shot 27481 at 0.875 seconds 71
5.2.7 Discussion of the perturbation inversion process 74
5.3 Further developments 75

6 Conclusion **77**

7 Acknowledgments **78**

8 Appendix **79**
8.1 Additional theory 79
8.1.1 Regularization by the second order derivative 79
8.1.2 Regularization by the Fisher information. 79
8.1.3 Straight field line angle θ^* 80
8.1.4 Toroidal and helical flux 82
8.2 Additional descriptions of the data processing blocks 83
8.2.1 Signal pre-processing 83
8.2.2 Bandpass filter 84
8.2.3 SVD 84
8.2.4 Time selection 85
8.2.5 Fourier transform filter 85
8.2.6 Stationary inversion: further considerations 86
8.2.7 Determination of $\rho_{\mathbf{lufs}}$ 87
8.2.8 Fit $\mathbf{A}$ to a given radial limit 88
8.3 Dictionary of the developed *Matlab* routines 88

1 Abstract

A complete method of tomographic inversion accounting for the presence of magnetic islands and based on the measurements of a single pin-hole soft X-ray camera is presented. The method divides the signals into a low frequency component used for the determination of the stationary emissivity, and a high frequency component used for the parametric determination of the magnetic island emissivity. The magnetic islands are simulated by a simple model based on the concentration of a current perturbation on a resonance surface. A method of correction of the magnetic equilibrium using the tomographic inversion is also described. The inversion method results in a very accurate determination of the position of the resonance surface, as well as a precise estimation of the island width. Due to the high degree of automation of the method, only a minimal prior knowledge of the parameters of the magnetic islands is required. A possible application could be the assessment of models of the dynamics of the island growth.

2 Introduction

2.1 Basic phenomenology and theoretical background

2.1.1 Tokamak principle

In order to achieve the production of energy using fusion reaction, a device called *tokamak* has been developed. Its purpose is to create a plasma and to confine it using a particular magnetic field configuration. The plasma state is required because of the high temperature that is needed to obtain a sufficient fusion rate.

The basic principle of the tokamak is to create a toroidal magnetic field that confines the plasma particles. The confinement requires also a poloidal magnetic field. A loop current created by induction in the plasma assures the main component of the latter, but a set of poloidal coils is also needed to achieve plasma control and equilibrium.

The usual modelisation of the underlying physics uses the axisymmetry assumption. In this hypothesis, all the processes can be fully described at a single poloidal cross-section of the tokamak. The imposed magnetic geometry can be described by an infinite set of nested toroidal magnetic surfaces, called *flux surfaces* (see figure 1).

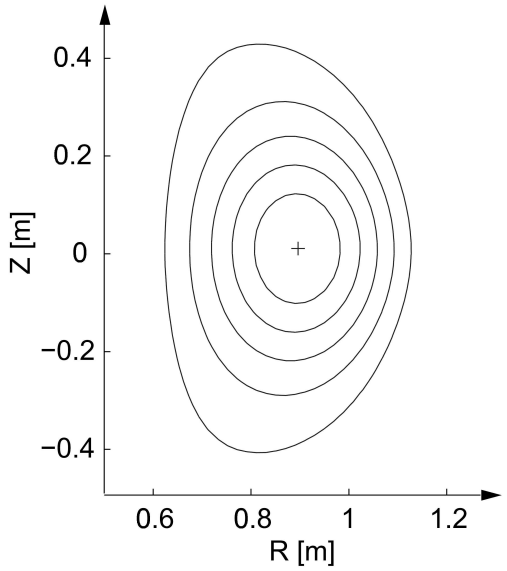

Figure 1: Example of a magnetic equilibrium of the TCV tokamak. Five nested flux surfaces are represented. Courtesy of Reimerdes [5].

The *poloidal flux* ψ_p at point (R, Z) in cylindrical coordinates is defined

as the magnetic flux passing through a disc that is centered on the symmetry axis, perpendicular to this axis, and which contains (R, Z) as a point of its circumference. ψ_p is set to 0 at the last closed flux surface of the plasma. The axisymmetry assumption results in a correspondence between the magnetic surfaces and the poloidal flux surfaces, explaining the given name. The magnetic surfaces are equivalently described by the *safety factor* q. q is defined by:

$$q := \frac{\Delta\varphi}{2\pi} \tag{1}$$

where $\Delta\varphi$ is the toroidal angle covered by a magnetic field line when the poloidal angle covered by the latter is equal to 2π. If $q = m/n$, with m and n being integers, the magnetic field line joins up on itself after m toroidal and n poloidal rotations. These particular surfaces can be sites of instabilities since constructive interferences can take place on them. Figure 2 shows the 3-D geometry of a magnetic field line on the surface $q = 2$. The poloidal flux can

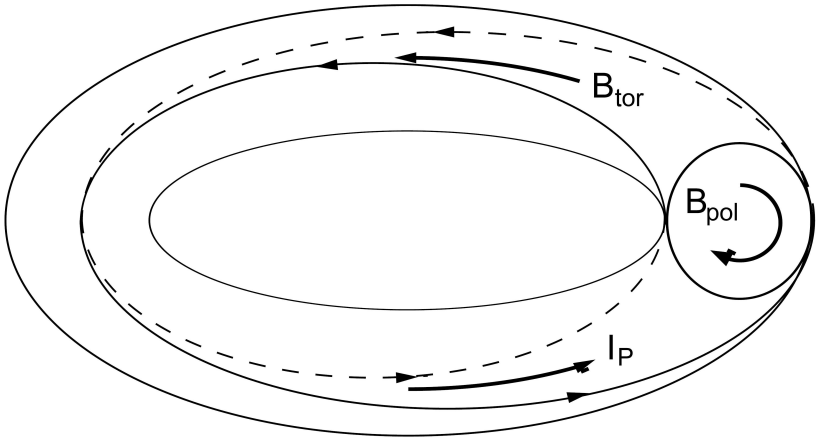

Figure 2: A schematic of a magnetic field line on the $q = 2$ magnetic surface. I_p is the plasma current, B_{pol} and B_{tor} the poloidal and toroidal magnetic fields. Courtesy of Reimerdes [5].

be used to define a new coordinate system, the *flux coordinates*, such that the flux surfaces expressed in this system are circular. Basically, the flux coordinate system is a toroidal coordinate system where the small radius is replaced by the dimensionless variable ρ defined by:

$$\rho := \sqrt{\psi_{p,01}} \quad \text{where} \quad \psi_{p,01} := 1 - \frac{\psi_p}{\psi_p(R_{mag}, Z_{mag})} \tag{2}$$

where (R_{mag}, Z_{mag}) is the coordinate of the *magnetic axis* and $\psi_{p,01}$ is the *normalized poloidal flux*. The magnetic axis corresponds to the center of the flux surfaces, where ψ_p is maximum.

2.1.2 X-ray emission in a tokamak plasma

The Brehmstrahlung emission relative to the acceleration of the electrons during particle interactions is inherent to the existence of the plasma state. The corresponding spectral emissivity function $G(\mathbf{x}, \nu)$ [W/m^3 Hz^{-1}] is isotropic. In the core of tokamak plasmas, the temperatures often reach the order of the keV and correspond to radiation in the X-ray spectral region.

Since the particles follow the magnetic field lines, the transport coefficients are much higher in the direction parallel to the field than perpendicular. As the Brehmstrahlung radiation results from the collisions between particles, the assumption of constant emissivity on magnetic surfaces is often made. In this framework, it is thus equivalent to determine the X-ray emissivity or the magnetic topology. However, we must point out the article by Granetz and Borrás [2] claiming that there exist small, but real, discrepancies between the X-ray emissivity contours and the magnetic flux surfaces.

2.1.3 Tomography inversion problem

Computerized tomography is a technique to reconstruct the local properties, for example, emission or absorption, of an object from line integrated measurements. The measurements of the emitted radiation G described in this report are confined to one poloidal cross-section of the tokamak (axisymmetry assumption). The detectors are placed behind a pin-hole situated at the bottom of the section wall. For the electron and ion densities commonly present in tokamak plasmas, the plasma is optically thin for soft X-ray radiation and refraction is negligible. Therefore, each detector measures the emissivity integrated along a well-defined cone inside the plasma. The cones will be further approximated by line of sights. The total power measured by detector l is:

$$P_l = \int d^3x \int d\nu \, \frac{\Omega_l(\mathbf{x})}{4\pi} G(\mathbf{x}, \nu) \eta_l(\nu) \quad [W] \tag{3}$$

where Ω_l is the solid angle subtended by the cone of sight, and η_l is the detection efficiency. Writing $A(s)$ the cross-section of the cone in function of the line coordinate s along its symmetry axis, d^3x may be written $d^3x = A(s)ds$. Recalling that $A(s) \propto s^2$ and that $\Omega_l \propto s^{-2}$, we can write:

$$P_l \approx \frac{(A\Omega)_l}{4\pi} \int_{S_l} ds \int d\nu \, G\eta_l \quad [W] \tag{4}$$

The *optical throughput* $(A\Omega)_l$ ("étendue géométrique") is a constant that can be taken outside the integral. S_l is the line of sight of the detector l. The *chord brightness* f_l is may be defined as:

$$f_l := \frac{P_l}{(A\Omega)_l/(4\pi)} \approx \int_{S_l} ds\, g \quad [W/m^2] \tag{5}$$

where $g = \int d\nu\, G$. Equation (5) is called a Radon transform of the function $g(\mathbf{x})$, from the name of the person who first found the analytical formulation of the inverse transform. To implement this theory, two possibilities are given: either to use a numerical approximation of the analytical inversion (*transform tomography methods*) or to start by discretizing the integral (5) and to invert it by linear algebra methods (*series expansion methods*). In plasma physics, the number of chords (or line of sights) that is used is small. Therefore, the inversion process requires the addition of assumptions on the shape of g that are easily introduced within the series expansion methods.

In the following section, a general solving method for the series expansion methods is presented (see Ingesson *et al.* [3] for more details). Writing explicitly the imaging properties of the detection system as a space dependent function $K_l(\mathbf{x})$, equation (5) becomes:

$$f_l = \int d^3x\, g(\mathbf{x}) K_l(\mathbf{x}) \tag{6}$$

The series expansion of g is given by $g(\mathbf{x}) = \sum_j g_j b_j(\mathbf{x})$, where g_j are the coefficients of the base functions $b_j(\mathbf{x})$. Equation (6) becomes:

$$f_l = K_{lj} g_j \tag{7}$$

where $K_{lj} := \int d^3x\, K_l(\mathbf{x}) b_j(\mathbf{x})$. The very general aspect of this description relies in the fact that $b_j(\mathbf{x})$ can be any kind of finite element description (pixel, pyramidal, ...) or base function description (e.g. sine and cosine functions along the poloidal coordinate, defined in the flux coordinate system, ...). To solve (7), the first constraint that must be satisfied is:

$$C(\mathbf{g}) := \|\mathbf{f} - \mathbf{K}\cdot\mathbf{g}\|^2 - \|\epsilon\|^2 \leq 0 \tag{8}$$

where ϵ is the authorized estimated error. Since the problem is ill-posed (i.e. small variations in f_l, due to noise for instance, lead to large variations in $g(\mathbf{x})$), the length of $\mathbf{g}$ must exceed the number of chords and the solution must be smoothed by a minimization constraint of an object function $O(\mathbf{g})$. The expression that must be minimized is thus:

$$\|\mathbf{f} - \mathbf{K}\cdot\mathbf{g}\|^2 + \alpha O(\mathbf{g}) \tag{9}$$

where α is equivalent to a Lagrange multiplier. The minimization constraint is expressed as:

$$\frac{\partial}{\partial \mathbf{g}} C(\mathbf{g}) + \alpha \frac{\partial}{\partial \mathbf{g}} O(\mathbf{g}) = 0 \tag{10}$$

A solution $g(\mathbf{x})$ that satisfies (10) is said to be a *regularized* solution. Generally, the emissivity function would be expected to be smooth. The object function may then be defined with respect to the norm of $\mathbf{g}$ or to a parameter describing the overall "unsmoothness". In addition, the resolution is greatly simplified if $O(\mathbf{g})$ is *quadratic*, i.e.:

$$O(\mathbf{g}) = \mathbf{g}^T \cdot \mathbf{H} \cdot \mathbf{g} \tag{11}$$

In that case, equation (10) becomes:

$$(\mathbf{K}^T \cdot \mathbf{K} + \alpha \mathbf{H}) \cdot \mathbf{g} = \mathbf{K} \cdot \mathbf{f} \tag{12}$$

α may be adjusted to get a compromise between the smoothness of the solution and its accuracy with respect to the measurements. A good start value is given by:

$$\alpha = \frac{Trace(\mathbf{K}^T \cdot \mathbf{K})}{Trace(\mathbf{H})} \tag{13}$$

In sections 8.1.1 and 8.1.2 of the appendix, we describe two object functions used in this work, namely the norm of the second order derivative and the Fisher information.

2.1.4 MHD perturbations - Magnetic islands

Many kinds of perturbations of the magnetic equilibrium occur in a tokamak plasma. The study of these perturbations is of crucial importance for the understanding of magnetic confinement quality and plasma stability. The perturbations that are dealt with here are called MHD perturbations because they are successfully described by the MHD theory. MHD is the basic theory that accounts for macroscopic behaviour of the plasma. There are many kinds of MHD perturbations: internal or external, resistive or ideal. The focus is given here to a resistive MHD perturbation called *magnetic islands*. In ideal MHD, the magnetic flux is frozen into the plasma and the magnetic field lines move with it. A deviation with respect to the equilibrium may, thus, result only in a change of curvature of the lines. In resistive MHD, this conservation no longer holds and the lines are allowed to break and reconnect, forming magnetic islands, regions of the plasma nearly isolated from the main core. Even if the magnetic perturbation has a small impact on the modulus of the magnetic field or on its local direction, it has a strong impact on its

topology, resulting in an important increase of the perpendicular diffusion coefficient. In three dimensions, the islands are situated along a resonance flux surface and can be seen as a unique flux tube winded up around the flux surface, following the geometry of the equilibrium field lines. The term "island" comes from the figures revealed by a poloidal cross-section of a flux tube making several toroidal turns before closing on itself.

A simple theoretical description of the magnetic islands can be given in the ideal case of a toroidal plasma of circular cross-section, on which the toroidal magnetic field is constant. As said above, the perturbation can only occur on a flux surface where $q_s = m/n$. Let us call r the distance to the magnetic axis, θ the poloidal angle coordinate, and φ the toroidal angle coordinate. A change of coordinate $\xi = \theta - \frac{n}{m}\varphi$ is performed in order to work in a coordinate system $(\hat{e}_r, \hat{e}_\xi, \hat{e}_\varphi)$ that corresponds to the magnetic field line geometry. $\hat{e}_\xi$ is perpendicular to $\mathbf{B}$ (on the q_s surface) and to $\hat{e}_r$, and ξ is constant along the magnetic field lines of the mentioned flux surface. By definition, the ξ-component of the equilibrium field is given by:

$$B_\xi(r) = B_\theta \cdot \left(1 - \frac{q(r)}{q_s}\right) \approx - \left(B_\theta \frac{q'}{q}\right)\Big|_s (r - r_s) \tag{14}$$

where r_s is the radius of the resonance surface. Note that $B_\xi(r_s) = 0$. In (14), q' is the derivative of q with respect to r. A current perturbation along the field lines of the q_s surface causes a radial perturbation $\delta B_{r,mn}$ of the magnetic field. In the simplest case,

$$\delta B_{r,mn} = \delta \hat{B}_r(r) sin(m\xi) \tag{15}$$

$\delta \hat{B}_r$ is a function of r because it is created by a current situated on the resonance surface. In order to find an analytical expression for the trajectory of the perturbed field line, $\delta \hat{B}_r$ is assumed to be constant. To find the trajectory of the perturbed field lines in the (r, ξ) space, the condition $\mathbf{B}_{total} \propto d\mathbf{l}$ is written. Expressing $\mathbf{B}_{total}$ as $\mathbf{B}_{total} := B_\xi \hat{e}_\xi + \delta B_{r,mn} \hat{e}_r$, and integrating the differential equation results in the following expression for the field lines:

$$(r - r_s)^2 = \frac{2}{m B_\theta(r_s) q'(r_s)} \delta \hat{B}_r r_s q_s (\cos(m\xi) + K) \tag{16}$$

where K is an integration constant. The resulting topology is shown in figure (3). The lines corresponding to $0 \leq K < 1$ are those inside the islands, the separatrix is given by $K = 1$, and the lines for the other values of K do not show any change in their topology. The width w of the islands is given by

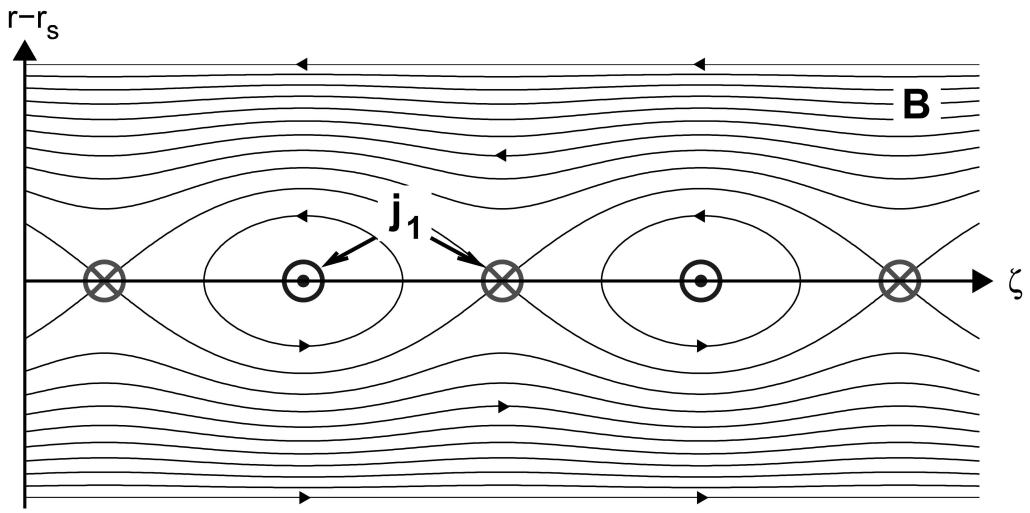

Figure 3: Sketch of the island formation resulting from a radial perturbation of the magnetic field. The perturbation is caused by a helical current density perturbation $\mathbf{j}_1$, along the magnetic field lines on a resonance flux surface at r_s. Courtesy of Reimerdes [5].

equation (16) with $K = 1$ and ξ corresponding to the maximum of the cosine term. It yields:

$$w = 4\sqrt{\frac{\delta\hat{B}_r r_s q_s}{mB_\theta(r_s)q'(r_s)}} \tag{17}$$

The detection of MHD activity in tokamak plasmas relies on the motion of the plasma as a whole. In fact, although the magnetic islands appear because of resistivity, we can consider that the magnetic islands are frozen into the plasma. Due to the thermal activity of the plasma, or to particular ways of heating the plasma (e.g. neutral beam injection), the latter always rotates on itself both poloidally and toroidally. This motion makes the magnetic islands pass in front of the detectors (magnetic pick-up coils, soft X-ray cameras, etc) and they are observed as high frequency fluctuations (in the range of the kHz on **TCV** (Tokamak à Configuration Variable)).

2.2 The DMPX at TCV

The Multiwire Proportional X-ray camera (**MPX**) is the main device used to furnish the data analysed in this project (see figure 4). It consists of a 1D camera placed behind a pin-hole and observing a poloidal cross-section of the plasma from the bottom. The X-ray detection system is based on a multiwire proportional counter, consisting of 64 parallel anode wires situated between

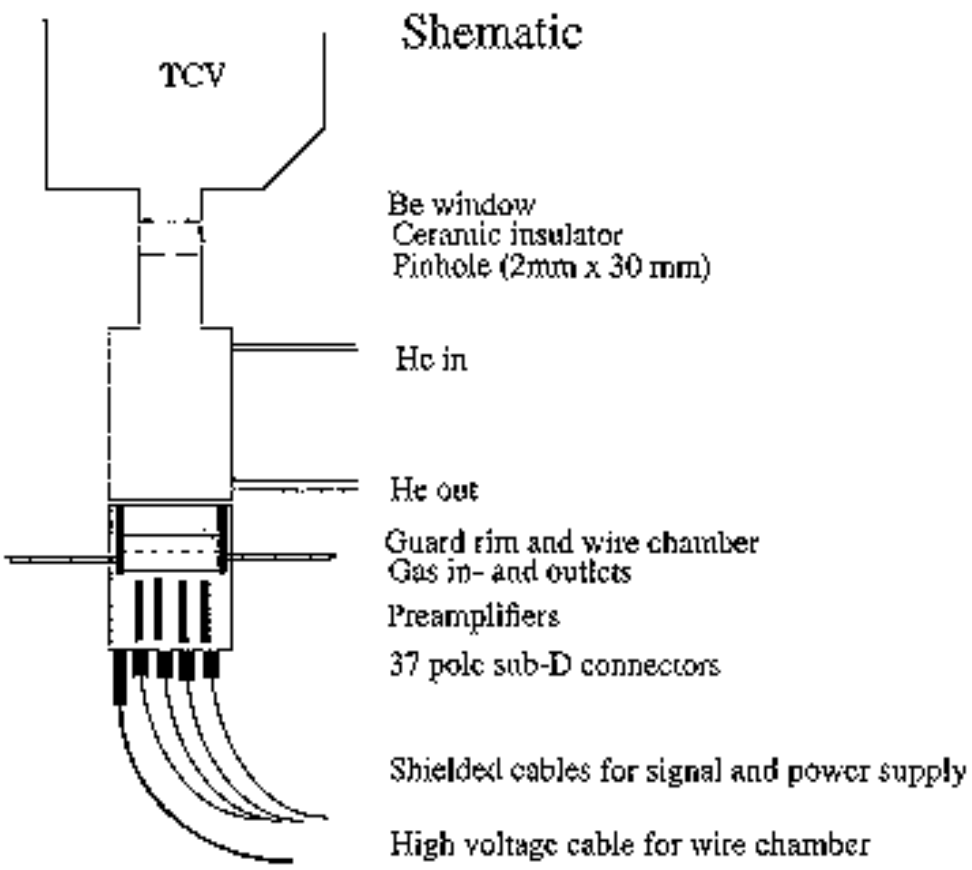

Figure 4: Schematic of the MPX device at TCV.

two cathode grids in a common gas chamber filled by an argon-methane, krypton-methane, or xenon-methane gas mixture at atmospheric pressure. The detector views the plasma through an helium chamber and a beryllium window, and provides measurements of the plasma core X-ray emission in the 3-30 keV range with a 50 kHz bandwidth. The sampling rate of the acquisition is of 200 kHz. The radial spatial resolution is approximately 8 mm at the mid-plane of the vacuum vessel. The Dual Multiwire Proportional X-ray camera (**DMPX**) is an extension of the MPX where the detection system has been enhanced by a second detection system working in another energy range and constituted of 32 wires, with a radial spatial resolution of 16 mm at the mid-plane of the vacuum vessel. Between the first and the second detection system, there is a versatile filter window that allows the selection of the energy spectrum to the second detection system.

The principle of detection is based on the ionisation of the gas mixture by the X-rays. The liberated electrons are then accelerated by the imposed electric field and create an localized current avalanche gathered by the anode wires. The latter current is a measurement of the X-ray flux. The X-ray emissivity is proportional to $n_e T_e^\alpha$ where $\alpha \approx 1 - 1.5$, n_e is the electron density and T_e is the electronic temperature.

2.3 Motivations, aims and objectives

Historically, a lot of work has been done to build theoretical and numerical models of magnetic islands, but much less to link these models with experimental data and to integrate them within the sets of usual data analysis methods. Among the pioneers, Reimerdes [5] has given a model simulating the magnetic effects of the islands at the magnetic probes of the TCV tokamak in order to allow a comparison with experiments and to determine the parameters of the real magnetic islands. The uncertainty on the obtained parameters is large because the reconstruction of the magnetic islands from the magnetic signal measured at the edge of the plasma is intrinsically not adequate to determine the exact position of the islands or their width. The latter are in fact determined by the magnetic topology, which is here only a secondary result of the obtained approximative current distribution. Other methods are based on the radiation emitted by the plasma. Inside magnetic islands, the radiation is different from the rest of the plasma and a tomographic inversion of the signals can reveal the islands. However, until now, the assumptions taken for these particular inversions are still the same as those generally made for tomographic inversion of tokamak plasmas (type of base functions, smoothness, etc) and do not give sufficient resolution to determine the parameters of the magnetic islands accurately (see Bessenrodt-

Weberpals *et al.* [1], Yoshimura *et al.* [8]).

The main aim of this project is to obtain a method based on the plasma radiation allowing the characterization of the magnetic islands appearing experimentally in TCV. This method should be applicable to different shots (term used for a complete experiment on TCV) with a minimal prior knowledge of the parameters of the perturbation. The used diagnostic is the DMPX because of its high bandwidth and high spatial resolution. As described above, the DMPX has a single pin-hole. In this case, the inversion process requires important assumptions on the emissivity profile, such as constant emissivity on flux surfaces. In a stationary plasma, such assumptions are valuable and often lead to reliable results. In the presence of MHD perturbations, the equilibrium is no longer axisymmetric and these assumptions become false. Consequently, we need to find an inversion process that can take the break of symmetry into account to obtain the perturbed emissivity profile, and give an accurate characterization of the magnetic islands. This process could rely on a combination with signals from other diagnostics or on a model of the prevalent MHD instabilities. The ultimate objectives that lie behind this project are to obtain a better knowledge of the instabilities, and thus to improve the plasma confinement.

3 Model of the magnetic islands and their emissivity

With the DMPX, the inversion problem may not be solved without imposing a shape for the magnetic perturbations, restricted here to the magnetic islands.

The purpose of this section consists in giving a model that can be used to generate any kind of magnetic islands, staying coherent with the description given in section 2.1.4. The input parameters of this model should allow the specification of the geometry of the islands in the poloidal cross-section: i.e. the toroidal mode number m, the width w, and the orientation Φ. The model presented here is based on those given in Reimerdes [5] and Schittenhelm *et al.* [7]. The principle is to work on a current perturbation localized on the desired resonance surface, and flowing along the magnetic field lines. This current is considered as the unique source of magnetic perturbation. As it is force-free, it does not change the equilibrium. After the description of the model for the magnetic islands, some considerations about the emissivity function relative to these islands are given.

3.1 Current perturbation

Considering a unique Fourier component with poloidal and toroidal mode numbers m and n for the current perturbation, and recalling that the latter is assumed to flow in the direction of the magnetic field, one can write:

$$\delta\mathbf{j}(\varphi, \theta^*, \psi_p) = c(\psi_p) \cdot e^{i(m\theta^* - n\varphi)} \cdot \mathbf{B} \tag{18}$$

where θ^* is the straight field line angle (see appendix, section 8.1.3). Since $\nabla \cdot \mathbf{j} = 0$ in the MHD model, B_R and B_Z are obtained from the derivatives of ψ_p, and if the toroidal symmetry holds, equation (18) leads easily to:

$$m\mathbf{B} \cdot \nabla\theta^* - n\mathbf{B} \cdot \nabla\varphi = 0 \tag{19}$$

Comparing with equation (82), it can be seen that equation (19) holds only at the surface $q = m/n$, showing that the assumed current perturbation (18) can exist only at this particular surface. This surface thus fulfills the condition of resonance for the current defined in (18).

The perturbed current density in A/m^2 has to be transformed into a perturbed current density in A/m to obtain a sheet current $\mathbf{j}_s$ on the resonance surface. $\mathbf{j}_s$ is the concentrated version of the current perturbation flowing between two neighbouring surfaces on each side of the resonance surface. These surfaces are separated by a dimensionless "distance" $d\psi_{p,01}$. The

current perturbation is concentrated on the resonance surface by writing:

$$\mathbf{j}_s d\psi_{p,01} = \delta\mathbf{j} dr \tag{20}$$

Since $d\psi_{p,01} \propto RB_p dr$ where B_p is the poloidal magnetic field and using equation (18), yields:

$$\mathbf{j}_s \propto \frac{1}{RB_p} \cdot e^{i(m\theta^* - n\varphi)} \cdot \mathbf{B} \tag{21}$$

In order to reconstruct the poloidal component of the field perturbation, only the toroidal component of the current density perturbation has to be taken into account. With $B_\varphi \propto 1/R$, the toroidal current density perturbation is proportional to:

$$j_{s,\varphi} \propto \frac{1}{R^2 B_p} \cdot e^{i(m\theta^* - n\varphi)} \tag{22}$$

For a numerical reconstruction of the magnetic field perturbation, it is necessary to discretise the model. The resonance flux surface is divided into toroidal filaments. In the following, the flux surface filaments are labelled with k. The toroidal component of the current perturbation is given by:

$$I_k = j_{s,\varphi,k} \Delta l_k \tag{23}$$

where Δl_k is the width of the filaments in the poloidal plane.

3.2 Reconstruction of the island geometry

The magnetic island geometry appear when the equilibrium helical flux and the flux perturbation induced by the current perturbation are combined. The equilibrium helical flux is expressed by (see section 8.1.4 of the appendix for details):

$$\psi_0^* = \psi_{p,0} - \frac{1}{q_s}\psi_{t,0} \tag{24}$$

where $\psi_{p,0}$ and $\psi_{t,0}$ are the equilibrium poloidal and toroidal flux, respectively. An important feature of ψ_0^* is its extremum at the resonance flux surface.

In order to give a consistent model of the magnetic islands, the flux perturbation should also be a helical flux. This would involve the calculation of the flux through complicated twisted surfaces, whose geometry is based on the magnetic field line trajectories. The difficulty of such a calculation and the intrinsic uncertainty in its result coming from the uncertainty on the description of the surfaces leads to approximate the helical flux perturbation by a poloidal flux perturbation. Its calculation is done as follows: the mutual

inductances M_{pk} between the points x_p of the plasma and the points x_k of the resonance surface are calculated through:

$$M_{pk} = \left(\frac{\mu_0}{4\pi}\right)^2 \oint_{T_p} \oint_{T_k} \frac{d\mathbf{l}_p \cdot d\mathbf{l}_k}{|\mathbf{r}_p - \mathbf{r}_k|} \tag{25}$$

where T_p and T_k are the toroidal filaments passing by x_p and x_k. Using equation (23), the flux perturbation is given by:

$$\psi_1^*(x_p) = \sum_k M_{pk} I_k \tag{26}$$

Contrary to Schittenhelm [7], Reimerdes [5] proposes to correct the expression (26) by projecting the currents on the magnetic field lines in order to give a better approximation of the helical flux perturbation:

$$\psi_{1,Rei}^*(x_p) = \sum_k M_{pk} I_k \cdot \frac{\sqrt{B_t(x_k)^2 + B_p(x_k)^2}}{B_t(x_k)} \tag{27}$$

where B_t and B_p are respectively the toroidal and the poloidal components of the magnetic field. This trick is strange from the point of view of the definition of the flux, because the currents no longer flow on the trajectories used for the calculation of the mutual inductances. In addition, it changes only very weakly the shape of the islands and does not lead to better results in the solving of the inversion problem. Therefore, we have not used it, and have retained the expression (26) as the best approximation of the helical flux perturbation.

3.3 Position of the magnetic islands

The position ρ_s of the islands in flux coordinate is an important input parameter of the model. It arises in the expressions of ψ_0^* and ψ_1^*. In ψ_0^*, contrary to ψ_1^*, the arbitrariness on ρ_s is problematic, because the resonance surface must coincide with the extremum of ψ_0^*. If the resonance condition given by $q_s = m/n$ is fulfilled, then ψ_0^* has its extremum well positioned. Therefore, the q-profile must evolve in function of ρ_s such that the condition $q(\rho_s) = m/n$ is always fulfilled. We may describe the new q-profile as a linear function of the old one:

$$q_{new}(\rho) := \frac{m}{n q_{old}(\rho_s)} q_{old}(\rho) \tag{28}$$

ψ_0^* is then calculated with q_{new}. Obviously, if the new position of the resonance surface is far away from the initial one, the q-profile will be notably

modified and the magnetic equilibrium conditions risk to be unfulfilled. Consequently, this solution appears to be well adapted for cases where the modifications applied on q stay in the limit of the uncertainty of the magnetic equilibrium reconstruction.

3.4 Time dependence of the perturbation

Until now, the time evolution of the perturbation has not been taken into account. In fact, as our detection system only works in the poloidal cross-section, no information is obtained on the toroidal behaviour, and the $n\varphi$ term appearing in equation (18) can be replaced by a phase function $\Phi(t)$ where t is the time variable. Due to the evolution of the rotation frequency of the plasma in function of time, it is difficult to give an exact expression of $\Phi(t)$. A relevant general shape can still be given:

$$\Phi(t) = 2\pi f_\Phi(t)t + \Phi_0 \tag{29}$$

On small time interval, f_Φ is roughly constant. Using equations (22), (23) and (26), and introducing a proportionality factor A, the flux perturbation may be written:

$$\psi_1^*(x_p, t) = A \sum_k M_{pk} \frac{1}{R_k^2 B_{p_k}} \cdot e^{i(m\theta_k^* - \Phi(t))} \Delta l_k \tag{30}$$

Taking the real part,

$$\psi_1^*(x_p, t) = A[\psi_c(x_p)\cos(\Phi(t)) + \psi_s(x_p)\sin(\Phi(t))] \tag{31}$$

where

$$\psi_c(x_p) := \sum_k M_{pk} \frac{1}{R_k^2 B_{p_k}} \cdot \cos(m\theta_k^*) \Delta l_k \tag{32}$$

and

$$\psi_s(x_p) := \sum_k M_{pk} \frac{1}{R_k^2 B_{p_k}} \cdot \sin(m\theta_k^*) \Delta l_k \tag{33}$$

As the different effects of rotation are not obvious, a brief description is given here. As said in section 2.1.4, the rotation of the plasma permits the detection of the magnetic islands. This rotation can be both toroidal and poloidal. In our case, no direct knowledge of the components of the motion of the plasma can be deduced from the DMPX signals. Without information from the magnetic probes surrounding the plasma, the problem is reduced to a motion that is apparently uniquely poloidal, where the n number is only involved in the determination of the position of the resonance surface. The

perturbation frequency f_{sig} measured by the Fourier transform of the signals of the DMPX thus only corresponds to this apparent motion. Consequently, the frequency f_{rot} of the apparent poloidal rotation of the plasma as a whole is simply given by $f_{rot} = f_{sig}/m$.

In the simulation of the magnetic islands, the expression (31) is used. Due to the multipole geometry of ψ_c and ψ_s, the variation of Φ over a whole period (using definition (29)) does not correspond to a whole rotation of the poloidal cross-section. In fact, the islands move until they reach, for the first time, a position equivalent to their departure position. Hence, $f_\Phi = f_{rot} \cdot m = f_{sig}$.

Finally, the global position of the plasma has been assumed to be constant with ψ_0^* written independent of time. This is reasonable since the characteristic time for a change in the equilibrium position of the plasma (order of 5 ms) is much larger than that corresponding to the rotation period of the magnetic islands (order of 0.1 ms).

3.5 Emissivity function and island isolation

Using the assumption of constant emissivity on the flux surfaces, the emissivity function $g(\mathbf{x}, t)$ corresponding to the soft X-ray may be written as:

$$g = g(\psi_{tot}^*) \tag{34}$$

where

$$\psi_{tot}^*(x_p, t) = \psi_0^*(x_p) + \psi_1^*(x_p, t) \tag{35}$$

With g_1 as a perturbation in the emissivity due to the presence of magnetic islands and g_0 the background emissivity, we have:

$$g = g(\psi_0^* + \psi_1^*(t)) = g_0(\psi_0^*) + g_1 \tag{36}$$

It is tempting to write $g_1 = g_1(\psi_1^*(t))$, and to further approximate that relation by $g_1(x_p, t) = A\psi_1^*(x_p, t)$ where A is a constant that can be combined with the proportionality constant already appearing in the equation (31). This would have the advantage of permitting a linear fit of both the orientation of the islands and the amplitude of the emissivity. This would also avoid the whole discussion about the helical flux and the positioning of the magnetic islands. Nevertheless, from a physical point of view, this does not make sense, since the change of topology in the magnetic field lines due to the islands creates a quasi isolation of the islands to the rest of the plasma. The extension of the island is, therefore, a critical parameter and must be accounted for in the expression of g_1. To resume, it is more the change of topology in the magnetic field than the amplitude of the flux perturbation that matters for our problem.

Let us call $\psi_i(x_p,t)$ the part of ψ^*_{tot} that is inside the islands. It is evaluated as follows: according to our convention for the extremum of ψ^*_0, ψ_i is given by the part of ψ^*_0 that is above the value ψ_{sp} of the flux at the *island separatrix* (i.e. last flux surface of the magnetic islands). As the position of the resonance surface is known in the model, the value of ψ_{sp} is given by the minimum of ψ^*_{tot} on this surface. Once the position of the islands is identified, it is then easy to select them, set their surrounding to zero and subtract ψ_{sp} to obtain a continuous function. Formally, it yields:

$$\psi_i(x_p,t) = \psi^*_{tot}(x_p) \cdot H_{\psi^*_{tot},\psi_{sp}}(x_p) - \psi_{sp} \cdot H_{\psi^*_{tot},\psi_{sp}}(x_p) \tag{37}$$

where H is defined by:

$$H_{\psi^*_{tot},\psi_{sp}}(x_p) = \begin{cases} 1 & \text{if } \psi^*_{tot}(x_p) \geq \psi_{sp} \\ 0 & \text{otherwise} \end{cases} \tag{38}$$

Figures 5 and 6 are examples of the shape that ψ_i can have in the cases $m = 1$, $m = 2$ and $m = 3$ respectively. The last closed flux surface is also represented. In these figures, ψ_i is normalised to 1.

As ψ_i is the part of ψ^*_{tot} that really determines the topology of the islands, it is necessary to see how it can appear in the expression of g. We can write:

$$\psi^*_{tot} = [\psi^*_0 + \underbrace{\psi^*_1(t) - \psi_i(t)}_{=:\Delta(t)}] + \psi_i(t) \tag{39}$$

Calculation shows that $||\Delta(t)|| \simeq ||\psi_i(t)||$. Therefore, Δ cannot be removed from the expression of ψ^*_{tot} on the basis of the norm. The determining element here is the effect on topology. Some tests have revealed that even though ψ^*_0 and $\psi^*_0 + \Delta$ have contour lines that differ a bit in their exact geometry, the topology of both contour lines are exactly the same. Consequently, we can write the following approximation:

$$g = g(\psi^*_{tot}) \simeq g(\psi^*_0 + \psi_i(t)) \simeq g_0(\psi^*_0) + g_1(\psi_i(t)) \tag{40}$$

A further approximation is made by: $g_1(\psi_i(t)) \propto \psi_i(t)$. Recalling that the time average of the perturbation of the emissivity must be equal to zero, g_1 may finally be written:

$$g_1(x_p,t) = P[\psi_i(x_p,t) - < \psi_i > (x_p)] \tag{41}$$

where the RHS term is normalised such that P is the peak value of g_1. Note that the time average of the magnetic islands can be again found in the background emissivity g_0. Since the topology of this time average is the same as the topology without islands, the expression $g_0 = g_0(\psi^*_0)$ still holds. Figure 7 shows an example of g_1 corresponding to figure 5 (bottom).

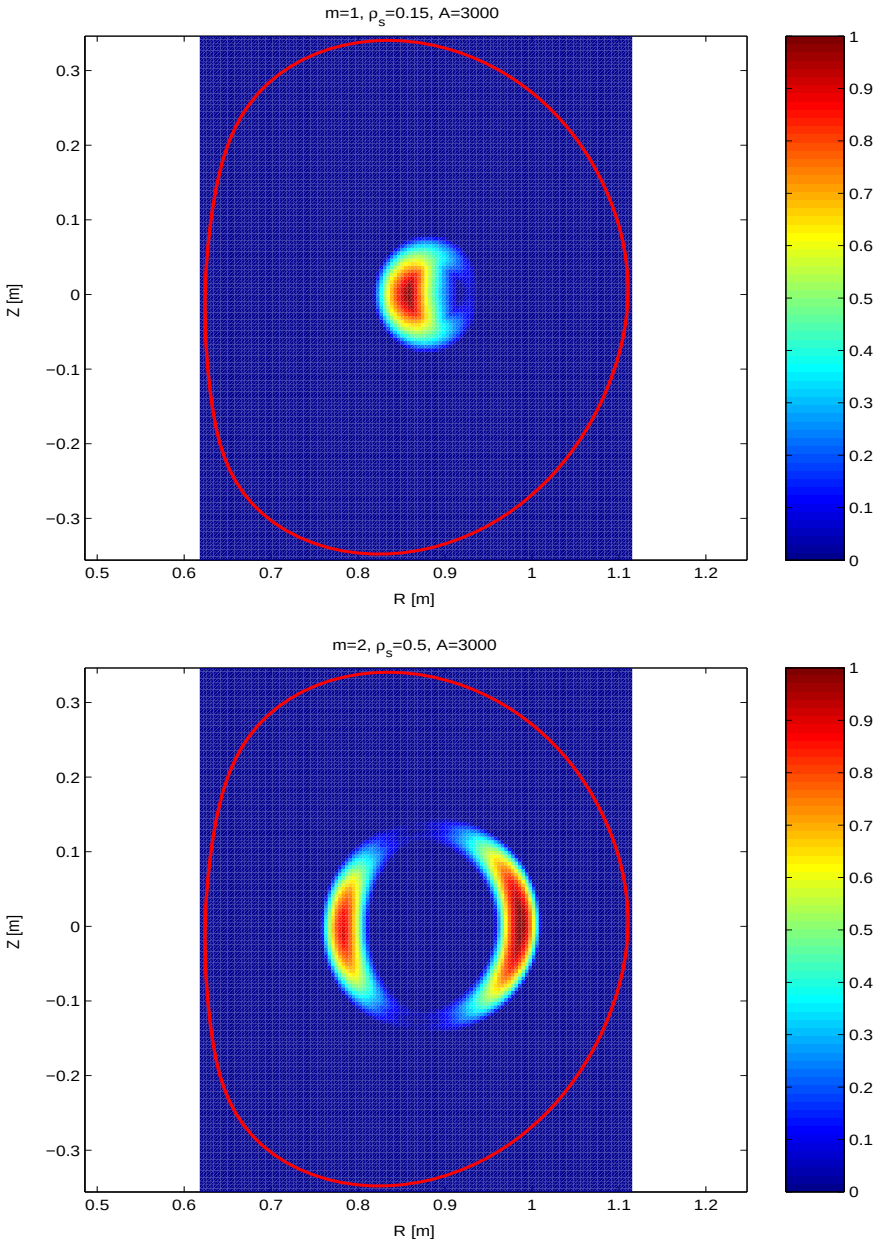

Figure 5: **Top.** Representation of the normalised isolated island in the case $m = 1$, $\rho_s = 0.15$ and $A = 3000$. **Bottom.** Case $m = 2$, $\rho_s = 0.5$ and $A = 3000$. The last closed flux surface is represented in red.

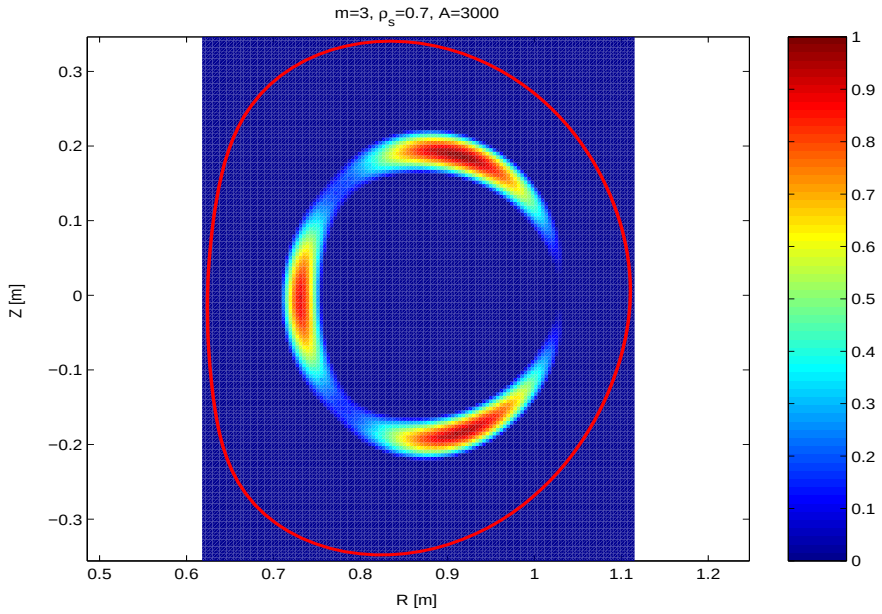

Figure 6: Representation of the normalised isolated islands in the case $m = 3$, $\rho_s = 0.7$ and $A = 3000$. The last closed flux shell is represented in red.

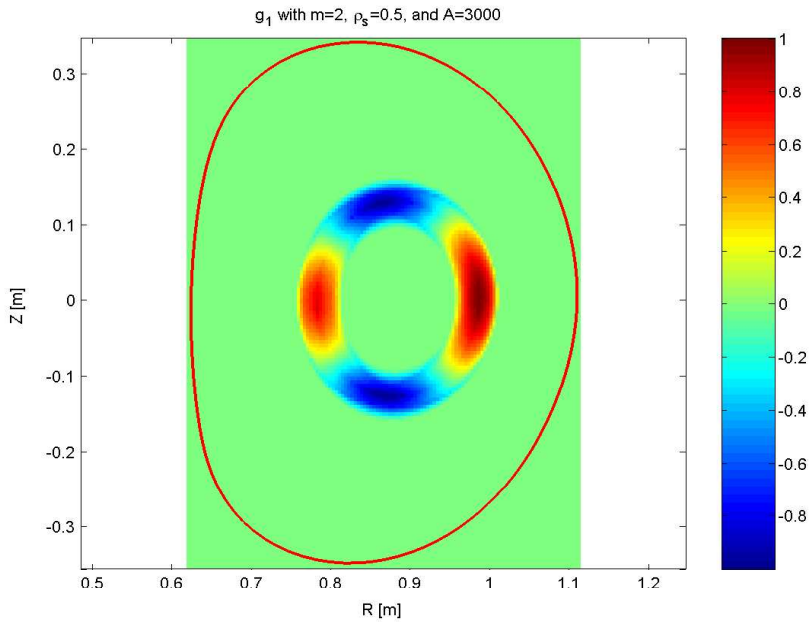

Figure 7: Representation of the normalised perturbation in the case $m = 2$, $\rho_s = 0.5$ and $A = 3000$. The last closed flux surface is represented in red.

3.6 Summary of the model

The development described above enables the construction of physically relevant magnetic islands, using the combination of a stationary helical flux and a flux perturbation. The islands are then isolated from the rest of the total helical flux function and are used to generate the emissivity perturbation function. The input parameters of the model are the following:

ψ_p : poloidal flux of the magnetic equilibrium.

q : safety factor of the magnetic equilibrium.

m, n : mode numbers describing the islands.

ρ_s : position of the resonance surface in flux coordinate.

$\Phi(t)$: initial orientation of the islands and time evolution.

A : amplitude of the flux perturbation. A is linked to the amplitude of the current perturbation. There is no direct way to specify the width of the islands, but the latter is a one-to-one function of A.

P : peak amplitude of the perturbed emissivity.

In the implementation, care has been taken to prevent non physical islands from being generated. For example, in the case $m > 1$, a test assures that the magnetic axis is not covered by the islands. Another test checks that the islands do not go too close to the last closed flux surface.

In order to complete the description given above, one can wonder what happens outside the field of the assumptions that have been used. Schittenhelm *et al.* [7] claim that the current perturbation does not vanish completely in the rest of the plasma. Outside the resonance surface, the magnetic field and the current perturbation do not have the same shear and the perturbation is no longer force-free. Thus, the magnetic equilibrium is changed and the plasma interacts with the perturbation. A comparison made between the simplified model and the complete one in a simple cylindrical geometry reveals that the island width corresponding to a localized current perturbation is overestimated by up to 14%. In our case, the width is fitted with respect to the measurements. Consequently, the current perturbation that is calculated *a posteriori* is underestimated.

4 Inversion method description

4.1 Used tools

The entirety of the inversion process has been written with the mathematical software *Matlab* version 6.5.0 from the *MathWorks* company, running under *AIX*.

The *ψ-toolbox* has also been intensively used in this work. Under this name is gathered a set of object-oriented routines running under *Matlab* and created by Jean-Marc Moret for the solving of problems occurring commonly in tokamak geometry. For instance, the ψ-toolbox allows the definition of grids in many types of coordinate systems and the passage from one to another. It also enables the definition of functions on these grids. Many kinds of operations are possible on the latter like for example interpolation, derivation or integration. The ψ-toolbox is particularly well suited for many operations involving the poloidal flux and the flux coordinate system, as well as the geometrical description of a set of chords.

4.2 General approach

The work has been designed in the structure of a block diagram representing the different functions of signal processing and their links. The base approach consists in dividing the components of the signal corresponding to the stationary plasma and the perturbation, to use different inversion process for each, and then combine them at the end. A block diagram of the procedure is presented in figure 8. The only information that cannot be deduced from the DMPX signals is the value of the mode number n. As some tools based on the magnetic probe signals already existed for the mode analysis, we have used them to obtain the value of n. These tools also allow to obtain an approximate value $t_{a,approx}$ of the time of analysis and $f_{sig,approx}$ of the frequency of the mode, as well as the value of m (see [5]). The next sections describe in detail the different blocks.

4.3 Signal pre-processing

The DMPX signals are already calibrated, and no work was performed on this subject. They contain frequent spikes that are a serious handicap for fulfilling the requirement of automatic signal processing. These spikes do not only extend in time, but also between the detectors. They are due to electric arcs that are sometimes created between the detection wires and the vessel of

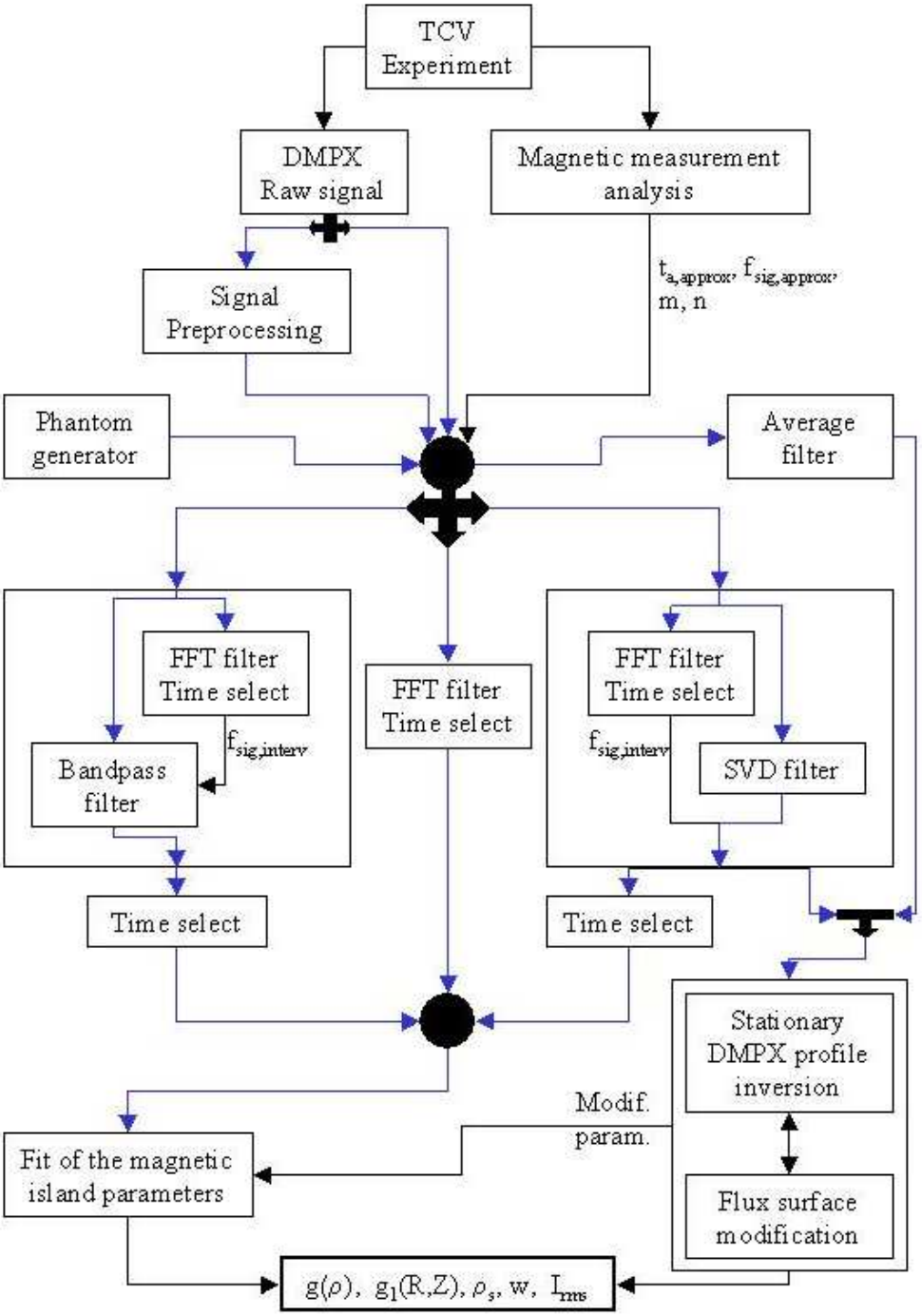

Figure 8: Block diagram of the inversion process. The blue arrows represent paths that hold DMPX data, whereas the black one hold some useful parameters only. Bold arrows are placed at positions where only one direction can be taken. $t_{a,approx}$ is the approximated time of analysis.

the DMPX when an X-ray passes. These spikes can extend over more than 5 wires and last several microseconds.

This block has been designed to remove these spikes, while keeping the modification of the signals as minimal as possible. The routine identifies each spike and replaces it by a local interpolation of the signals. It also allows the interpolation of the detectors on which no signal has been recorded. The details of the routine are given in section 8.2.1 of the appendix. Two examples of the efficiency of the routine are given in figures 9 and 10.

4.4 Average filter

The DMPX signal corresponding to the stationary plasma is obtained from the average of the signals on a small time window (some milliseconds) around the desired time of analysis. The obtained results are very robust.

4.5 Bandpass filter

The bandpass filter block is made of a bandpass filter feeding the block designed for the perturbation inversion. The frequency limits of the filter are given by the FFT block. This block has the advantage of differentiating the harmonics of a mode or the signals produced by other modes. However, if there are modes evolving at signal frequencies close to one another, their respective signal will be mixed. The details of the routine are given in section 8.2.2 of the appendix.

4.6 SVD filter

Our main interest in using the SVD (see appendix section 8.2.3) relies in the decomposition of the different temporal behaviours that can be performed. If the magnetic island is the dominant perturbation of the plasma equilibrium, then the first component of the SVD corresponds to the stationary behaviour of the plasma and the second one to the magnetic islands. The only limitation of this method appears when two modes are present at the same time, and at the same frequency in the DMPX signals. In that case, the SVD results in the mixing of both modes. Note however that this particular limitation also occurs for all the other methods presented here.

4.7 Time selection

This block is designed to select the time t_a where the signals present the largest MHD mode amplitude and a maximal number of oscillations along

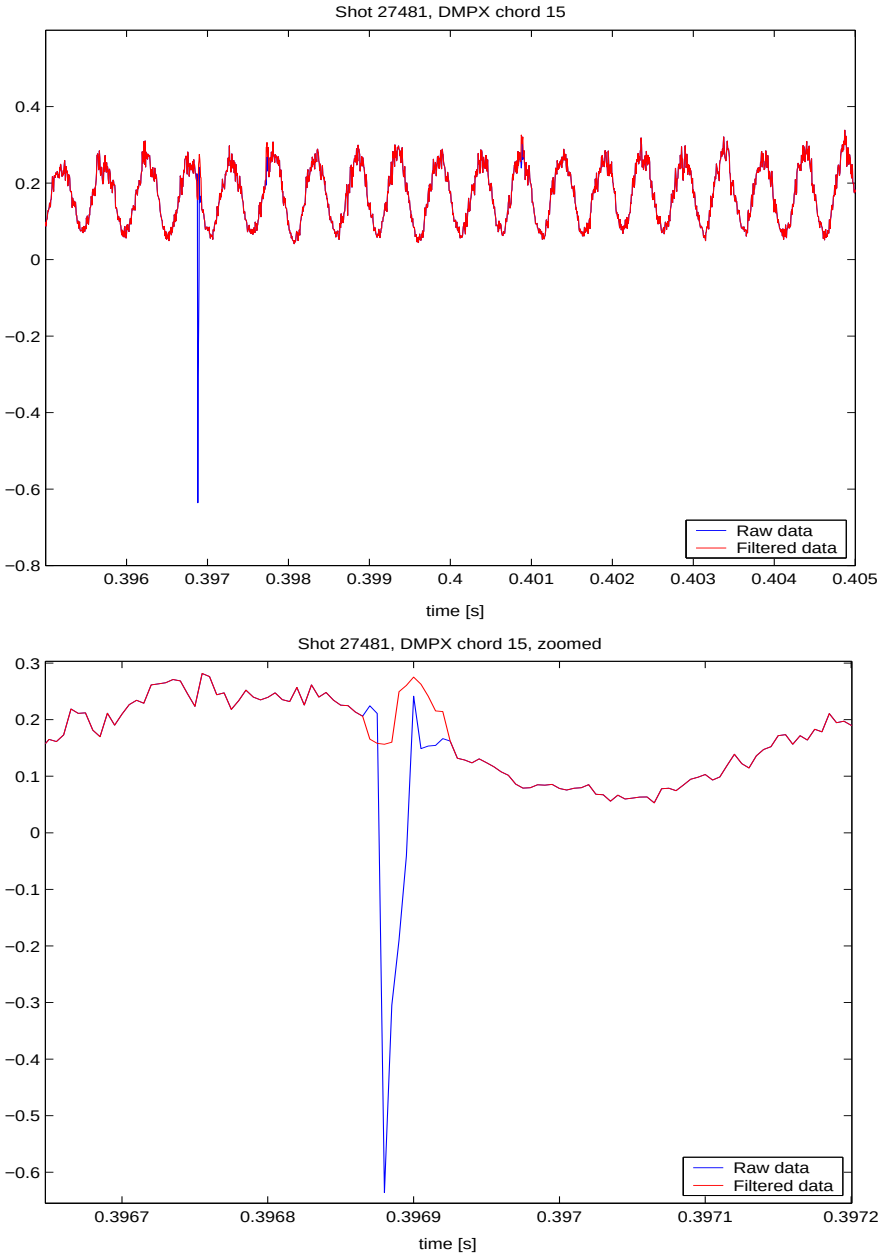

Figure 9: **Top.** Example of the efficiency of the pre-processing routine for the spike removal on shot 27481, DMPX wire number 15. **Bottom.** Zoom on the spike region.

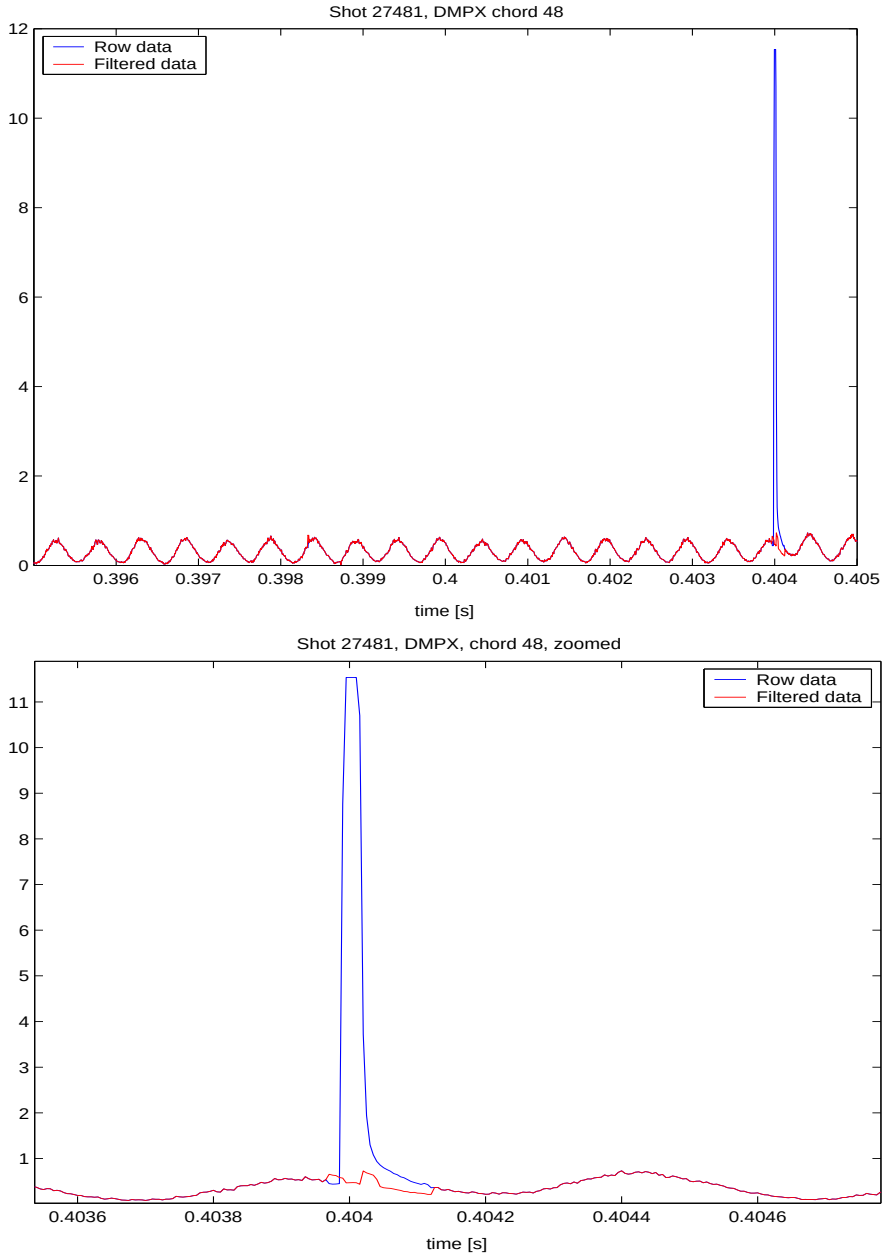

Figure 10: **Top.** Example of the efficiency of the pre-processing routine for the spike removal on shot 27481, DMPX wire number 48. **Bottom.** Zoom on the spike region.

the detector array. The routine analyses the filtered (bandpass or SVD filter) DMPX signals on a small time interval around $t_{a,approx}$ (see appendix, section 8.2.4 for details).

4.8 Fourier transform filter

This block has mainly two outputs: the Fourier transform of the DMPX signals and the frequency limits of the MHD mode. The Fourier transform is performed around the time t_a on a time interval whose length is defined with respect to the desired frequency resolution of the calculated spectra. Only the positive frequencies of the spectra are kept. See section 8.2.5 of the appendix for a detailed explanation of the routine.

4.9 Stationary plasma profile inversion

4.9.1 Inversion procedure description

We call stationary plasma the plasma seen on a time scale larger than that of the MHD perturbations that are studied here. The method presented here is dedicated to the inversion at a particular time, but it could be easily extended to the inversion at several different times.

The origin of the signals is either a local average of the DMPX signals or the first topos of a SVD analysis of the signals on a small time interval (typically 2 ms). The errors are given by the standard deviation of the DMPX signals on the given time interval. At this time scale, the magnetic flux surfaces are toroidally symmetric. The tomographic inversion requires the choice of a set of base functions b_j whose combination is fitted to the recorded signals (see section 2.1.3). The quality of the result is improved if the base functions respect the geometry of the problem. Due to the assumption of constant emissivity on flux surfaces, a possible choice is $b_j = b_j(\rho)$ where ρ is the radial flux coordinate. For simplicity, the base functions are defined as pixels along ρ:

$$b_j(\rho) = \begin{cases} 1 & \text{if } \rho_j \leq \rho \leq \rho_{j+1} \\ 0 & \text{else} \end{cases} \tag{42}$$

where ρ_j, $j = 1, ..., N_p + 1$ with $\rho_1 = 0$ and $\rho_{N_p+1} = 1$, are the radial flux coordinates of the flux surfaces delimiting the pixels, and N_p is the number of pixels. In order to allow a smoothing of the emissivity profile without deteriorating too much the accuracy of the fit, N_p is defined by $N_p = N_c + 1$, where N_c is the number of chords that pass inside the plasma.

The inversion of the profile requires the calculation of the matrix $\mathbf{K}$ appearing in equation (7). It mainly consists in determining the distance that

each chord of the DMPX covers in each pixel. This calculation is made by the routine *psitbxdxp* of the ψ-toolbox. The inversion itself is based on equation (12). The application of the minimum Fisher information condition is not sufficient to obtain a good solution. The results present always artificial sharp oscillations. The minization based on the second order derivative leads to smooth emissivity profiles, but too flat with respect to those obtained via the Fisher information. Since both types of problems cancel themselves, the final solution consists in combining the object function of both methods. In order to allow a comparison of weights between both object functions, the latter are normalized by their maximal singular value (standard norm proposed by *Matlab*). The new inversion equation may be written:

$$\left[\mathbf{K}^T \cdot \mathbf{K} + \alpha \left(\beta \mathbf{H_D} + \mathbf{H_F}^{(n)}\right)\right] \cdot \mathbf{g}^{(n+1)} = \mathbf{K}^T \cdot \mathbf{f} \tag{43}$$

where $\mathbf{H_D}$ and $\mathbf{H_F}$ are the normalized versions of the operators defined in (75) and (79) respectively. The superscript n indicates the iteration number (see section 8.1.2). The factor β, set to 0.1, is constant during the solving process. The given value corresponds to a majority of inversions where the obtained profiles are just the smoothed versions of those obtained only by minimization of the Fisher information. Of course $\mathbf{K}$ and $\mathbf{f}$ are pre-multiplied by a diagonal matrix of weights inversely proportional to the errors on the measurements. In addition, two edge conditions on $\mathbf{g}$ are imposed, namely:

$$g_{N_p} = 0 \text{ and } \left.\frac{\partial g}{\partial \rho}\right|_{\rho=0} = 0 \tag{44}$$

The derivative at the origin is approximated by the difference between the first two values of $\mathbf{g}$. A weight ten times superior to the maximal weight is attributed to these edge conditions to assure their fulfillment.

Further considerations on the choice of α are given in section 8.2.6 of the appendix. A routine testing the presence of oscillations in the obtained emissivity profile is also described there.

4.9.2 Modification of the equilibrium

Since the position of the pixels is determined by the plasma equilibrium reconstruction, the accuracy of the inversion is limited by the accuracy of the equilibrium reconstruction. Yann Camenen, engineer in charge of the DMPX at CRPP, has developed a method to decrease the impact of the latter. The trick is to consider that the chords of the DMPX that are on the **HFS** (High Field Side) and those that are on the **LFS** (Low Field Side) of the magnetic axis are two sets of redundant chords that can be used separately

to calculate an emissivity profile. The difference between both profiles may be summed up by a parameter d_p defined by:

$$d_p := (\mathbf{g}_{HFS} - \mathbf{g}_{LFS})^T \cdot (\mathbf{g}_{HFS} - \mathbf{g}_{LFS}) \tag{45}$$

where $\mathbf{g}_{HFS}$ and $\mathbf{g}_{LFS}$ are the profiles reconstructed using the HFS and LFS set of chords respectively. d_p is then minimized by changing the geometry of the flux surfaces. At present, this modification can be performed in four different ways:

mode 1: radial translation The whole plasma is translated radially by redefining the coordinate grid on which the poloidal flux is defined.

mode 2: radial deformation The last flux surface remains unchanged, but the flux surfaces are radially moved by a factor that is maximal at the magnetic axis and null at the last flux surface. Formally, it is written:

$$\psi_{new}(R + h(R,Z) \cdot dR \cdot [1 - \rho(R,Z)], Z) := \psi_p(R,Z) \tag{46}$$

where dR is the radial displacement of the magnetic axis and $h(R,Z)$ a function that equals 1 inside the plasma and 0 outside.

mode 3: radial translation and deformation A combination of mode 1 and 2.

mode 4: radial and vertical translation The whole plasma is translated radially and vertically. As the vertical resolution of the DMPX is poor (the camera is placed at the bottom of the vacuum vessel), this mode is not very advised.

The minimization process is performed by the *Matlab fminsearch* function. This function allows to find a local minimum of a scalar function of several variables. Our contribution to that particular work consisted in expressing the modification of the flux surfaces in terms of poloidal flux in order to use the ψ-toolbox. This required among others the development of a routine calculating the function $h(R,Z)$. In addition to that, the starting condition of the minimization process has been refined by setting the initial radial displacement such that the chord receiving the maximal signal passes by the magnetic axis. In the case of mode 3, the initial radial displacement is divided equally between both kind of modifications.

4.10 Fit of the magnetic island parameters

4.10.1 General aspects

The block concerning the inversion process of the perturbation signal is based on the model of the magnetic islands. The inversion consists in finding the parameters of the perturbation emissivity function g_1 (see equation (41)) that gives the best solution to equation (47), where the variable $f_{l,1}$ is the perturbed part of f_l, the signal recorded on chord l:

$$f_{l,1}(t) = \int d^3x \; g_1(\mathbf{x}, t) K_l(\mathbf{x}) \tag{47}$$

There are different ways to fit the parameters of the model, depending on the kind of filter that we use for the signal, the execution speed that is desired and the accuracy of the solution. In order to minimize the number of operations, the fit is always done in the following order: the position ρ_s of the resonance surface, the amplitude A of the perturbed flux, the initial orientation of the island Φ_0, and finally the peak amplitude P of the perturbed emissivity. That means that the fit of one element of the list is done keeping the previous elements constant. Depending on the way the fit is performed, some of these elements can be fitted simultaneously.

Like equation (6) has been transformed into its matricial equivalent (7), equation (47) can be reexpressed by:

$$\mathbf{y} = \mathbf{M} \cdot \mathbf{z} \tag{48}$$

where $\mathbf{y}$ contains the perturbation signals, $\mathbf{M}$ is the equivalent of $\mathbf{K}$ and $\mathbf{z}$ contains the coefficients of the functions integrated in $\mathbf{M}$. The perturbation signals obtained from the DMPX present, at time t_a, large oscillations along the detector array. These oscillations correspond to the geometry of the magnetic islands. The position of the peaks, for instance, is a one-to-one function of the real ρ_s. The parameters of the model correspond better to those of the real modes when the global behaviour of these oscillations is reproduced than when the data are directly fitted in a least square sense. These considerations are accounted for by fitting both the DMPX profiles and their derivative along the chords. It may be written:

$$\begin{bmatrix} \mathbf{y} \\ w_g \cdot \mathbf{dy} \end{bmatrix} = \begin{bmatrix} \mathbf{M} \\ w_g \cdot \mathbf{dM} \end{bmatrix} \cdot \mathbf{z} \tag{49}$$

where $\mathbf{dy}$ and $\mathbf{dM}$ are the derivatives of $\mathbf{y}$ and $\mathbf{M}$ along the detector array. Both are normalised to be comparable to $\mathbf{y}$ and $\mathbf{M}$ respectively, by using the ratio of the maximum of $\mathbf{y}$ and the maximum of its derivative. The factor w_g

sets the relative importance of the data and their derivative. The solution of equation (49) is found with the *Matlab backslash* function. A parameter χ^2_{mean} describing the overall badness of the fit may be defined by:

$$\chi^2_{mean} = \frac{1}{2N_c - 1} \sum_{i=1}^{2N_c-1} \left(\left(\begin{bmatrix} \mathbf{M} \\ w_g \cdot \mathbf{dM} \end{bmatrix} \cdot \mathbf{z} \right)_i - \begin{bmatrix} \mathbf{y} \\ w_g \cdot \mathbf{dy} \end{bmatrix}_i \right)^2 \tag{50}$$

Since the model is non-linear with respect to ρ_s and A, their interval of possible values must be determined before solving equation (49).

Interval of possible values of ρ_s. An estimation of ρ_s can be deduced from the value of the position ρ_{lufs} of the last unperturbed flux surface, when looking from outside the plasma. ρ_{lufs} is the flux coordinate of the flux surface that would contain completely the islands and be tangent to them. Its determination is based on the study of the signal along the chords (at time t_a), and more precisely on the separation of the chords that are inside the perturbation from those that are outside the perturbation. We note ρ_{min} the radial flux coordinate at which a chord is the closest to the magnetic axis. Since ρ_{min} is unique for a given chord, the transition from the chord selection to ρ_{lufs} is direct. Section 8.2.7 of the appendix describes the method used to determine ρ_{lufs} and its uncertainty $\Delta\rho_{lufs}$.

If $m > 1$ where m is the mode number, there is a certain symmetry of the islands on both side of ρ_s. Thus, the interval of possible ρ_s may be defined as:

$$\frac{\rho_{lufs}}{2} \leq \rho_s \leq \rho_{lufs} \quad \text{if} \quad m > 1 \tag{51}$$

If $m = 1$, the mode can spread over the magnetic axis and the inferior limit can go close to zero. In our work, we have set:

$$\frac{\rho_{lufs}}{10} \leq \rho_s \leq \rho_{lufs} \quad \text{if} \quad m > 1 \tag{52}$$

These limits are here rather to increase the execution speed of the inversion process than to limit the latter. Therefore, the error on ρ_{lufs} is not necessary in (51) and (52). The *Matlab fminbnd* function is used to fit the value of ρ_s. It works in the same way as *fminsearch* but finds the minimum of a function with only one varying parameter, and needs the limits of the interval of possible values. Compared to *fminsearch*, the localization of the minimum is generally faster and better. It is less sensitive to small local minima or to flat zones. If the process converges towards one of the limits, an error message is given.

First estimation of the flux perturbation amplitude and the width of the island. The islands are generated on 2-D grids whose cells must have dimensions adapted to the width of the islands. It is thus important to have a good approximation of the latter.

For a given ρ_s, the width is estimated as follows. Using the ψ-toolbox, we can generate an object containing the definition of the flux surfaces corresponding to ρ_s and ρ_{lufs}. It is then possible to determine the mean distance d_m between both surfaces. In the case $m = 1$, the mean distance d_{lufs} from the magnetic axis to the ρ_{lufs} surface is more interesting. We obtain the first estimation of the width w by:

$$w = 0.8 \cdot min\{2 \cdot d_m, d_{lufs}\} \tag{53}$$

The 0.8 factor is added because it is advantageous to use a grid cell a bit smaller than to restart the whole process of fitting of A because the expected width was too large. The dimensions of the grid cell are set such that there are at least 10 grid points across the islands at the position where they are the largest. This condition is a good compromise between the smoothness of the islands and the computational time. When the islands are small, the number of grid points can become very large. In order to reduce a bit the computational time, the dimension of the grids are set to be tangent to the flux surface $\rho = \rho_{lufs} + 3 \cdot \Delta\rho_{lufs}$. With the same aim in view, the width used for the definition of the grid size cannot be smaller than 1 cm.

Knowing the approximate width, it is then possible to generate the stationary helical flux and the flux perturbation on the good grid. The equation of the approximated width of the island (17) can be rewritten in terms of flux:

$$w = 4 \sqrt{\frac{\psi_1^*(r_s)}{\left| \frac{d^2\psi_0^*}{dr^2}\Big|_{r=r_s} \right|}} \tag{54}$$

Equations (31), (53) and (54) show that A is approximatively a quadratic function of w. The second derivative appearing in (54) is calculated by using the expression of the helical flux in toroidal coordinates. An approximate value A_{approx} of A can thus be calculated and used to generate an island structure. In case it is necessary, A_{approx} is divided by 2 repetitively until the island passes the width test (see section 3.6). If A_{approx} has been decreased, a new approximative width is calculated with equation (54) and a new grid is defined.

Interval of possible values of A. In this process, three values of A are searched. The first value, A_{min}, is the value that gives an island whose

radial extension corresponds to $\rho_{lufs} - 2\Delta\rho_{lufs}$. A_{min} is the reference for the eventual definition of a new grid cell size. Its search is initiated with A_{approx}. Of course, it is searched only if this is relevant according to the given ρ_s. Otherwise, A_{min} is given by a tenth of the second A, A_{lufs}. A_{lufs} corresponds to an island radial extension limited by ρ_{lufs}. The last value, A_{max} corresponds to $min\{\rho_{lufs} + \Delta\rho_{lufs}, 0.99\}$. The routine that fits the value of A to the desired last perturbed flux surface is described in section 8.2.8.

Logic of the global fit. The complete fit of the parameters operates as follows:

- ρ_{lufs} is determined.
- The interval of possible ρ_s values is deduced.
- An arbitrary value of ρ_s is taken from that interval and the limits of the interval of possible A values are determined, as well as the grid cell size.
- A, Φ and P are fitted by minimization of χ^2_{mean} (linear or non-linear).
- The lowest value of χ^2_{mean} is attributed to the given ρ_s and the process is started again with another ρ_s until the global minimum of χ^2_{mean} is found.

In the next sections, the different elements relative to each resolution path are described.

4.10.2 Inversion of SVD or bandpass signals

As SVD signals and bandpass signals have the same behaviour, there are dealt with in the same way. Since the orientation of the island Φ and the amplitude A of the flux perturbation must be fitted simultaneously, the *fminsearch* function must be used to achieve the fit. This function needs start values for A and Φ_0. For A, the initial value is given by A_{lufs}. Although *fminsearch* does not take limits on the input variables, we can define limits inside the function that is minimized, and replace the calculated value of χ^2_{mean} by *realmax* (the largest real value existing in *Matlab*) if *fminsearch* proposes an input value that exceeds the desired limits. Of course, A_{min} and A_{max} are used as limits. Limiting the search has many advantages: the computational time is decreased; the generation of too large islands is avoided; and A cannot be negative. For Φ_0, some new developments are required.

First estimation of the orientation of the islands. Here the problem consists in finding a first estimation of Φ_0. Since we only look for a rough approximation of Φ_0, the perturbation emissivity may be written $g_1(\mathbf{x},t) = A\psi_1^*(\mathbf{x},t)$ (see section 3.5). The finished expansion of the islands in space can be simulated by truncating ψ_1^* such that only its extrema are kept. This is performed by defining a relative cut level l_r, and by only keeping the parts of ψ_c and ψ_s that exceeds l_r positively or negatively. In our work, a good compromise has been found with $l_r = 0.5$. Let us call $\tilde{\psi}_c$ and $\tilde{\psi}_s$ the truncated versions of ψ_c and ψ_s. A rough approximation $\tilde{g}_1$ of g_1 may then be defined by:

$$\tilde{g}_1(\mathbf{x},t) = A\left[\tilde{\psi}_c(\mathbf{x})\cos(\Phi(t)) + \tilde{\psi}_s(\mathbf{x})\sin(\Phi(t))\right] \tag{55}$$

Within this approximation, the factors A, $\cos(\Phi)$ and $\sin(\Phi)$ appearing in equation (47) can be taken outside the integral. The terms appearing in the generic equation (49) may then be described as:

y: $N_c \times n_t$ matrix of the filtered DMPX signals. n_t is the number of time samples.

M: $N_c \times 2$ matrix containing the line integrals of $\tilde{\psi}_c$ and $\tilde{\psi}_s$.

z: $2 \times n_t$ matrix containing $A\cos(\Phi(t))$ and $A\sin(\Phi(t))$.

w_g**:** set here to 4.

Up to now, there is no constraint on the $\pi/2$ phase shift that must appear between both lines of $\mathbf{z}$. Unfortunately, this condition is not fulfilled spontaneously by the fit and must be introduced to obtain a consistent solution. The rotation sense of the islands is determined by comparing the first and the second line of $\mathbf{z}$, that usually present a small phase shift. The problem is solved on a time interval of two periods after t_a with the addition of 3 iterative constraints to the equation system (49). The first one is a constraint of continuity in time and is expressed as:

$$\mathbf{C_1} = \begin{bmatrix} z_{12} & z_{13} & \cdots & z_{1,n_t} & z_{11} \\ z_{22} & z_{23} & \cdots & z_{2,n_t} & z_{21} \end{bmatrix} \tag{56}$$

The second constraint is a constraint of periodicity and is expressed as:

$$\mathbf{C_2} = \begin{bmatrix} z_{1,n_p+1} & z_{1,n_p+2} & \cdots & z_{1,n_t} & z_{11} & z_{12} & \cdots & z_{1,n_p} \\ z_{2,n_p+1} & z_{2,n_p+2} & \cdots & z_{2,n_t} & z_{21} & z_{22} & \cdots & z_{2,n_p} \end{bmatrix} \tag{57}$$

where n_p is the number of time samples corresponding to a time period of the perturbation. The last constraint is the constraint of $\pi/2$ phase shift. It is written:

$$\mathbf{C_3} = \gamma \cdot \begin{bmatrix} z_{2,rnd(n_p/4)+1} & z_{2,rnd(n_p/4)+2} & \cdots \\ -z_{1,rnd(n_p/4)+1} & -z_{1,rnd(n_p/4)+2} & \cdots \\ \cdots & z_{2,n_t} \quad z_{2,1} \quad z_{2,2} & \cdots & z_{2,rnd(n_p/4)} \\ \cdots & -z_{1,n_t} \quad -z_{1,1} \quad -z_{1,2} & \cdots & -z_{1,rnd(n_p/4)} \end{bmatrix} \tag{58}$$

where *rnd* is the *Matlab round* function. γ represents the rotation sense and is defined by:

$$\gamma = \begin{cases} +1 & \text{if } \frac{d\Phi}{dt} > 0 \\ -1 & \text{else} \end{cases} \tag{59}$$

The constraints are added in the equation system (49) as follows:

$$\mathbf{W} \cdot \begin{bmatrix} \mathbf{y} \\ w_g \cdot \mathbf{dy} \\ \mathbf{C_1}^{(n)} \\ \mathbf{C_2}^{(n)} \\ \mathbf{C_3}^{(n)} \end{bmatrix} = \mathbf{W} \cdot \begin{bmatrix} \mathbf{M} \\ w_g \cdot \mathbf{dM} \\ \mathbf{1}_2 \\ \mathbf{1}_2 \\ \mathbf{1}_2 \end{bmatrix} \cdot \mathbf{z}^{(n+1)} \tag{60}$$

where (n) is the iteration number, $\mathbf{1}_2$ is a 2×2 identity matrix and $\mathbf{W}$ is a weight matrix that account for the difference of magnitude between the signal and the coefficients of $\mathbf{z}$. It also gives the relative weight of the constraints and the data. The difference of magnitude is compensated by a factor obtained from the maximum of $\mathbf{y}$ and $\mathbf{z}$. The results are satisfying if the importance of the constraints with respect to the data are set to 1 for $\mathbf{C_1}$, 2 for $\mathbf{C_2}$ and 5 for $\mathbf{C_3}$. The iterative process is initiated with a null weight on the constraints. It is stopped when the difference between $\mathbf{z}^{(n+1)}$ and $\mathbf{z}^{(n)}$ falls under a certain level.

If the rotation sense cannot be determined with sufficient certainty, the system is solved with both senses and the sense that gives the better fit is kept. Φ_0 is the orientation angle corresponding to t_a. It is estimated using z_{11} and z_{21}.

Fit of A and $\mathbf{\Phi_0}$. Once the initial values of Φ_0 and A are available, the *fminsearch* function can enter into play. It calls a function that generates g_1 and solves equation (49) with the following definitions:

y: $N_c \times 1$ matrix of the filtered DMPX signals at t_a.

M: $N_c \times 1$ matrix containing the line integrals of g_1.

z: 1×1 matrix containing P.

w_g**:** set here to 5.

fminsearch normally finds the best values for the fit. There is however a whole set of tests that check whether the process converged towards a limit of the allowed intervals, that assures that the found solution does not correspond to a flat zone of χ^2_{mean}, and that checks that the size of the grid cell is adapted.

4.10.3 Inversion of signals in frequency space

Due to the periodic behaviour of the perturbation, the analysis of the signals in frequency space is particularly well adapted to our problem. Since the Fourier transform is a linear operation, we can take a Fourier transform of equation (47) on the time:

$$\hat{f}_{l,1}(\nu) = \int d^3x \; \hat{g}_1(\mathbf{x}, \nu) K_l(\mathbf{x}) \tag{61}$$

where a hat symbolizes the Fourier transform and ν is the frequency variable. Due to the shape of g_1 (see equation (41)), it may not be possible to obtain a usable analytical expression of $\hat{g}_1$. This mainly comes from the complicated time dependence of the function H appearing in ψ_i. The next paragraph establishes of way of solving this problem.

Approximation of $\mathbf{g_1}$. A numerical Fourier transform of g_1 ends to an amplitude spectrum containing a main peak at f_Φ and secondary peaks at harmonics of f_Φ. The latter are not interesting since the DMPX spectra is filtered to keep only the frequencies close to the dominant frequency of the mode f_{sig}. Therefore, a useful approximation of g_1 can result from its projection on a single component of a Fourier series:

$$g_{1,appr}(\mathbf{x}, t) := P \cdot [g_r(\mathbf{x}) \cos(2\pi f_{sig} t) + g_i(\mathbf{x}) \sin(2\pi f_{sig} t)] \tag{62}$$

The functions g_r and g_i are the components of the projection of g_1 on the cosine and sine functions. They can be found as follows: for a given value of A, 8 regularly spaced values of Φ are defined and the 8 corresponding g_1 are generated. For each value of $\mathbf{x}$, a least square fit of $g_r(\mathbf{x})$ and $g_i(\mathbf{x})$ is done to minimize the difference between g_1 and $g_{1,appr}$ in each angular orientation. Here, g_1 and $g_{1,appr}$ have an absolute peak value of 1 and P does not come into play. An example of $g_{1,appr}$ is shown in figure 11. The Fourier transform

of $g_{1,appr}$ is given by:

$$\begin{aligned}\hat{g}_{1,appr}(\mathbf{x},\nu) &= P\left[g_r(\mathbf{x})\int_{-\infty}^{+\infty} dt\, e^{-i2\pi\nu t}\cos(2\pi f_{sig}t)\right.\\ &\left. + g_i(\mathbf{x})\int_{-\infty}^{+\infty} dt\, e^{-i2\pi\nu t}\sin(2\pi f_{sig}t)\right] \end{aligned} \tag{63}$$

With P' as the product of P with the integration constant, we have:

$$\hat{g}_{1,appr}(\mathbf{x},\nu) = P'\left[g_r(\mathbf{x}) - i\cdot g_i(\mathbf{x})\right] \tag{64}$$

Note that in the reasoning, we have lost the information on the sign of f_{sig}, because if f_{sig} were negative and expressed as such in equation (62), then $\hat{g}_{1,appr}(\mathbf{x},\nu)$ would be given by the complex conjugate of the actual expression.

In expression (62), there is also no initial phase given to the islands. g_r and g_i are independent of the frequency and also of Φ_0, but the latter is involved in the sine and cosine functions and results in the multiplication of P' by a term $e^{i\Phi_0}$.

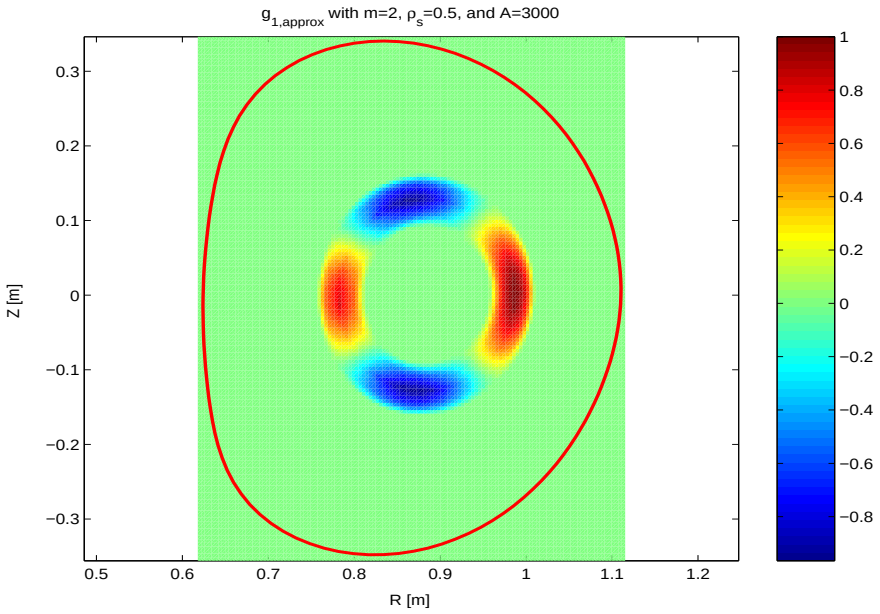

Figure 11: Representation of the approximative form $g_{1,appr}$ of the function g_1 appearing in figure 7. Comparison shows only weak differences.

Inversion. Although we work in frequency space, equation (49) still holds. It is solved here with the following definitions:

y: $N_c \times 1$ matrix of the Fourier transform of the DMPX signals at f_{sig}.

M: $N_c \times 1$ matrix containing the line integrals of $\hat{g}_{1,approx}$.

z: 1×1 matrix containing $V := P' \cdot e^{i\Phi_0}$.

w_g**:** set here to 5.

The rotation sense is accounted for by solving (48) twice; the first time as it is written, and the second time using the complex conjugate of **M** and **dM**. Both values of χ^2_{mean} are compared and the rotation sense giving the lowest one is kept. The initial phase Φ_0 is equal to the phase of V. The calculation of P requires the calculation of the integral appearing in the Fourier transform. Writing W the window used in the Fourier transform, the integral may be written:

$$F := \int_{-\infty}^{+\infty} dt\, e^{-i\cdot 2\pi f_{sig} t} W(t) \cos(2\pi f_{sig} t) \tag{65}$$

In terms of numerical calculation, it yields:

$$F \approx \sum_{n=-N/2}^{N/2} W(n) \cos^2(2\pi f_{sig} n \Delta t) \tag{66}$$

where N is the number of time increments in the time interval used for the analysis. Note that the dt has no numerical equivalent because it does not appear in the definition of the discrete Fourier transform. We finally have:

$$P = \frac{|V|}{F} \tag{67}$$

In the method presented above, the inversion is done for the dominant frequency only. Note that it suffices to add columns to **y** and **V** to extend the method to several frequencies fitted independently. Some tests have been done in that direction using artificial signals but the results have shown that the best information was in the dominant frequency only, and that the combination of the different frequencies resulted in a worse solution.

For a given ρ_s, only A is a non linear variable of $g_{1,appr}$, so that the function *fminbnd* can be used with the limits A_{min} and A_{max}. As in the previous case, a whole set of tests is in place to check that the final solution is a real solution and that it is obtained on the good grid.

4.10.4 Optimized interval of possible values of ρ_s

The computational time is quite important in this work and any possibility to reduce it is appreciated. In equation (55), we have given a rough approximation of g_1 based on a truncation of ψ_1^*. This expression allows a linear fit of A and Φ_0, P being comprised in A. Despite the roughness of this model, it gives finer limits of the interval of possible values of ρ_s at a low cost in computational time. The latter is low because the fit of A and Φ_0 is linear, the question of the grid cell dimension vanishes, and no islands are generated. The implementation is done by using $\tilde{\psi}_c$ and $\tilde{\psi}_s$ in the definition of $\mathbf{M}$ (see equation (49)) and works for any kind of signals (SVD, bandpass or FFT). In the case of time signals, the phase shift constraints are not used and the solving of (49) is performed for the time t_a only.

4.10.5 Optimized fit of the orientation in the case of SVD or bandpass signals

The combination of the functions g_r and g_i defined in equation (62) is a reliable approximation of g_1. With them, the fit of the orientation passes from non-linear to linear, and *fminbnd* may be used for the fit of A.

The inversion procedure is the same as that described in section 4.10.2 for the first estimation of the orientation of the islands. $\tilde{\psi}_c$ and $\tilde{\psi}_s$ must only be replaced by g_r and g_i in the definition of $\mathbf{M}$, and w_g must be set to 10 instead of 4. Note that the constraint on the phase shift has been tested to be still necessary. Φ_0 is determined by z_{11} and z_{21}, and P is determined by:

$$P = \sqrt{z_{11}^2 + z_{22}^2} \tag{68}$$

4.10.6 Determination of the width of the islands

The knowledge of the width of the islands matters for the question of transport and energy confinement because the superposition of neighbour islands causes stochastic diffusion of the magnetic field lines and the plasma particles. There exist also some models of the perturbation dynamics and these models could later be compared with the results given by our analysis. Here, the width is determined in the flux and cylindrical coordinate systems.

Extension in flux coordinates. Knowing the parameters ρ_s and A of the islands, its extension in terms of the flux coordinate ρ is determined as follows: the islands are generated and isolated as described in section 3.5. The extrema of $\psi_{p,01}$ in the zone of the poloidal cross-section covered by the

islands are determined. The square root of these extrema gives the interval $[\rho_1; \rho_2]$ of values of ρ that contains the islands. This determination is very accurate and reliable.

Width in cylindrical coordinates. The width of the islands is measured perpendicularly to the resonance flux surface. In section 8.1.3 of the appendix, we show that the level curves of θ^* are perpendicular to the flux surfaces. The determination of the width consists then in calculating θ^* in cylindrical coordinates (done with the tools of the ψ-toolbox), in using the *Matlab contourc* function to generate the level curves of θ^*, in projecting the islands on these level curves, in determining the limits of the islands on them, and finally in calculating the width. The limits are determined by a level condition of 1% of the peak value of the islands.

For the cases with the mode number m larger than one, the average of the islands on the orientation is used in order to find a function $w(\Phi)$ giving the width for any orientation. The returned width is the mean of $w(\Phi)$.

For the case $m = 1$, the determination of the width is a bit harder because the island generally covers the magnetic axis. In that case, the island orientation is chosen such that the island has its maximum under the magnetic axis on a vertical axis passing by it. This position is chosen because the corresponding width has an intermediary value there. The island is projected only on the level curves $\theta^* = -\pi/2$ and $\theta^* = \pi/2$, which are the curves that would correspond to the vertical axis if the magnetic field was circularly symmetric around the magnetic axis. As before, the determination of the width is done via the determination of the crossing points between the island projection and the said level. However, the level curve $\theta^* = \pi/2$ usually crosses the ends of the island. Therefore, the routine looks for the first minima (going from bottom to top) of the projection between the limits found previously. The upper limit is redefined by the position of this minima. However, in the case $m = 1$, there is a certain probability that the island overlaps itself in the central zone. Consequently, if the value of the island at this minima is above the reference level, the projection is interpolated to simulate the end of the island without overlapping, in order to calculate an approximative width. This interpolation is done by selecting the first part of the projection (until the minimum), by calculating the mean value of the second order derivative during the downhill and by using it as an edge condition of the interpolation.

4.10.7 Determination of the *rms* current perturbation

Once A is fitted, it is possible to come back to an estimation of the current perturbation. As said in section 3.6, the current obtained that way is

underestimated. Developing equation (23), we have:

$$I_k = \frac{A \cdot \Delta l_k}{R_k^2 \cdot B_{p,k}} \left(\cos(\varphi)\cos(m\theta_k^*) + \sin(\varphi)\sin(m\theta_k^*)\right) \tag{69}$$

I_k is a function of φ. The root mean square value I_{rms} of the total current perturbation is then defined by:

$$I_{rms} := \sum_k \sqrt{\frac{1}{2\pi}\int_0^{2\pi} d\varphi \, I_k^2} \tag{70}$$

4.11 Phantom signal generator

The best way to check the consistency of the results is to know what they have to be. This is the reason why a routine allowing the generation of artificial signals, also called *phantoms*, has been created. The routine is made of two routines, one for the generation of stationary signals and the other for the generation of perturbation signals. Both kind of signals are then merged with the possibility to add absolute or relative gaussian noise on the final signals.

The block that generates the stationary signals takes as inputs the definition of a magnetic configuration and the emissivity profile in flux coordinates. It uses the ψ-toolbox to calculate the transfer matrix $\mathbf{K}$.

The block that creates the perturbation signal takes as input the parameters of the islands that are simulated. Since the value of A has no intuitive sense, the input of A is replaced by the input of the desired island width. The corresponding A is found by an iterative process based on the approximative relation (17) between A and the width. Once the right A is found, the base functions g_r and g_i of the approximative perturbed emissivity defined in equation (62) are calculated, and used to build the matrix $\mathbf{M}$ (see equation (49)). $\mathbf{z}$ is defined by:

$$\mathbf{z} := \begin{bmatrix} \cos(2\pi \cdot m \cdot f_{rot} \cdot \mathbf{t}_b - \Phi_0) \\ \sin(2\pi \cdot m \cdot f_{rot} \cdot \mathbf{t}_b - \Phi_0) \end{bmatrix} \tag{71}$$

where $\mathbf{t}_b$ is a line vector representing the time basis. The perturbation signals are then given by:

$$\mathbf{f}_1(t) := \mathbf{G} \cdot \mathbf{z} \tag{72}$$

By merging the stationary and the perturbation signals, we can use the complete inversion process as if the signals were raw DMPX signals, thus assuring to have a comprehensive testing.

5 Results and discussion

The results of the stationary and the perturbation profile inversions are presented below. In each case, examples with phantoms are also given to assess the reliability of the processes.

5.1 Stationary profile inversion

5.1.1 Phantoms

Figures 12 and 13 present the results obtained for a phantom corresponding to the profile given in figure 12. The signal is free of noise, but a 0.5% relative error has been added since the inversion routine needs a certain value for the error on the signal. The process using the modification of the flux surfaces has not been used.

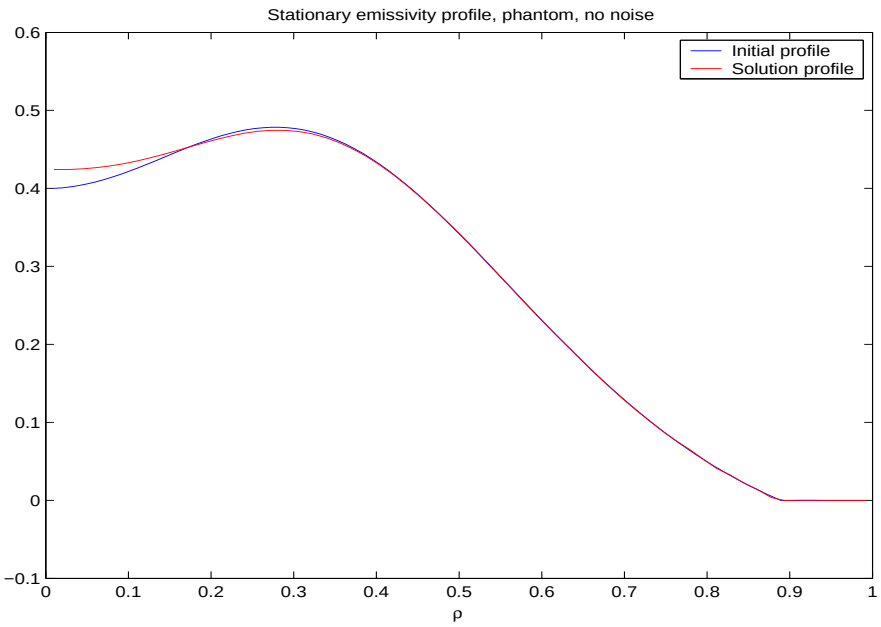

Figure 12: Profile $g(\rho)$ obtained from the inversion of the phantom DMPX signal using all the chords. No noise added on the signal.

Figures 14 and 15 present the results obtained for a phantom corresponding to the profile given in figure 14. A 2% relative gaussian noise has been added to the signal. The process using the modification of the flux surfaces has not been used.

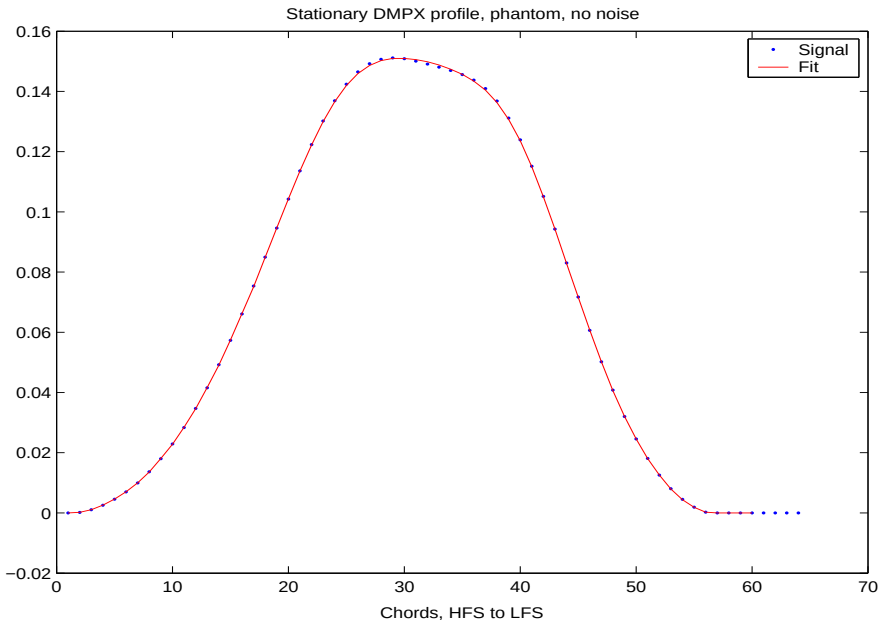

Figure 13: Phantom DMPX signal and fit generated by the reconstructed emissivity profile. No noise added on the signal.

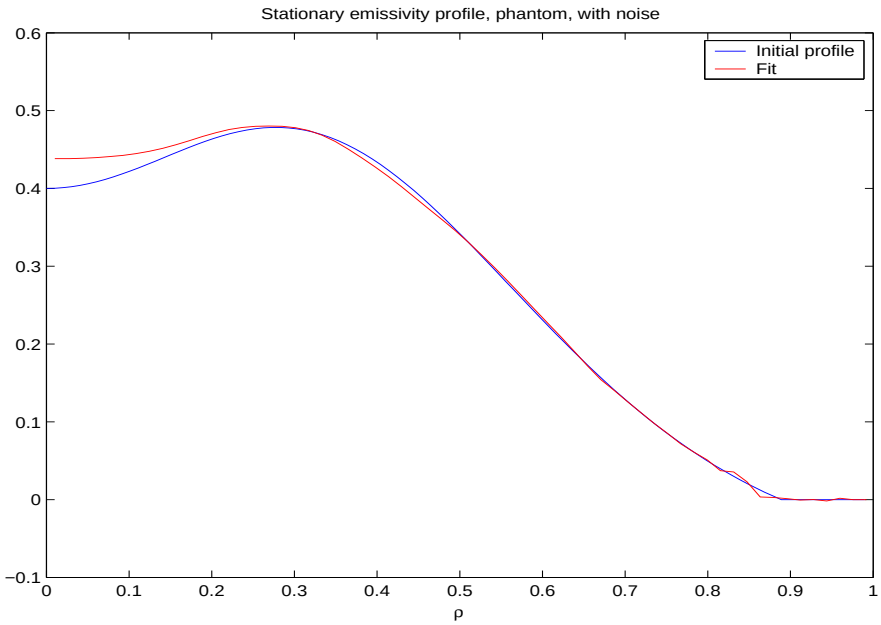

Figure 14: Profile $g(\rho)$ obtained from the inversion of the phantom DMPX signal using all the chords. 2% noise added on the signal.

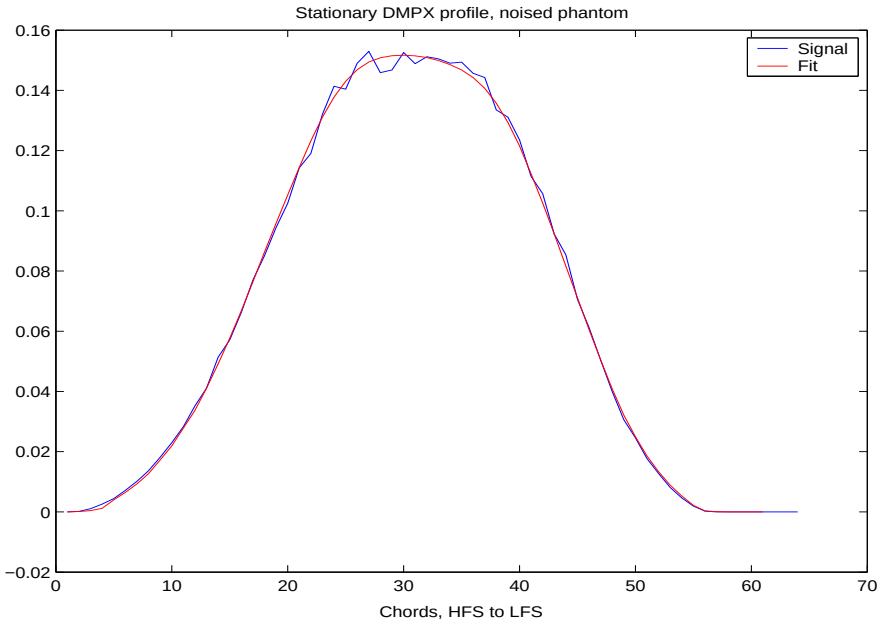

Figure 15: Phantom DMPX signal and fit generated by the reconstructed emissivity profile. 2% noise added on the signal.

5.1.2 Real signals

We present in figures 16 and 17 the results of the inversion of the stationary DMPX profile obtained for the shot 27481 at 0.4 seconds. The results obtained with or without the process using the modification of the flux surfaces can be compared. A 2 ms average of the signals has been used to generate the DMPX profile.

In order to improve the results obtained from the perturbation profile inversion, the stationary profile inversion has been performed for all the interesting shots using the modification of the flux surfaces of type 3. The obtained parameters are given in table 1. One of the interesting discharges is the shot 22621. However, at the time of that shot, the DMPX was much closer to the plasma than today. So all the chords passed close to the central zone of the plasma. As the signal corresponding to the periphery of the plasma is always mixed with the signal coming from the central zone, the stationary inversion is hard to obtain. Thus, we have decided not to modify the flux surface description for this shot.

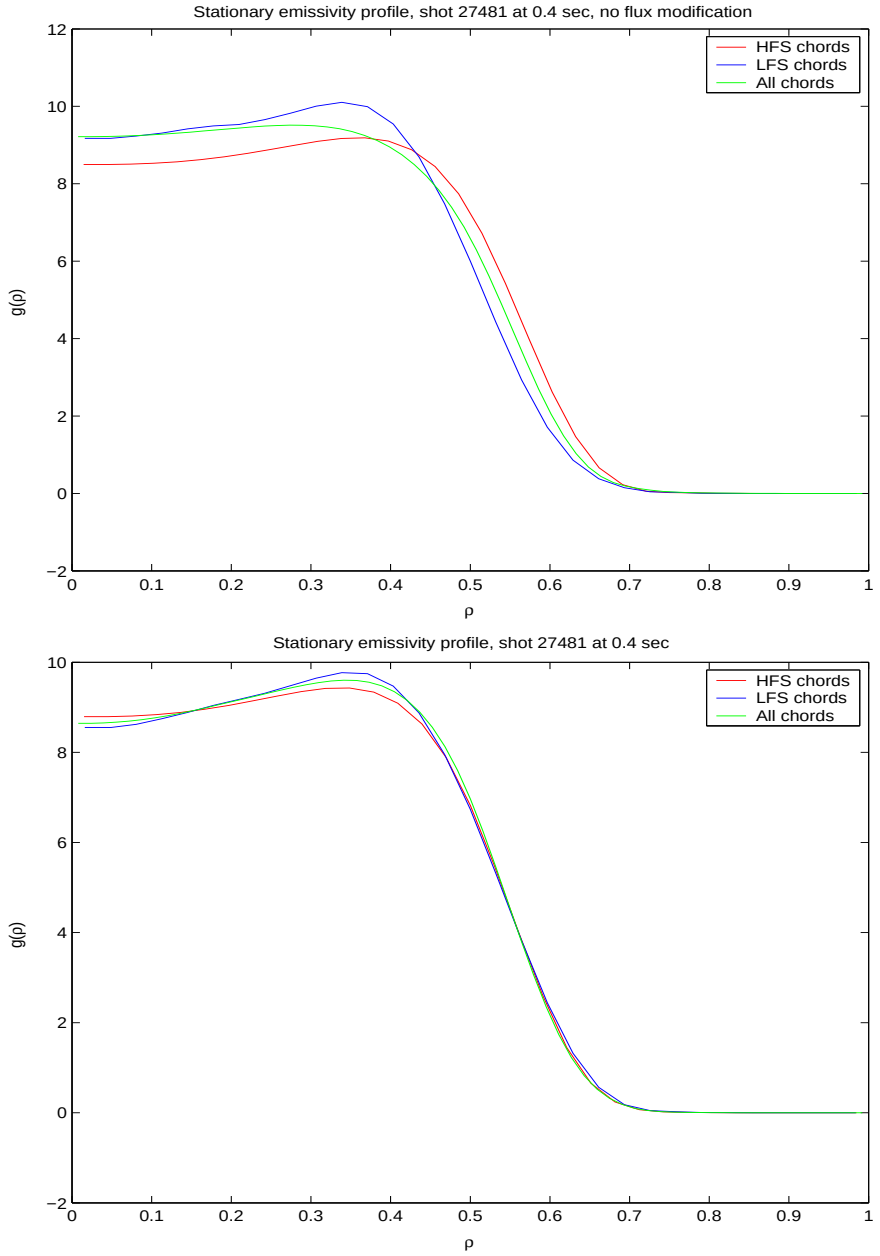

Figure 16: **Top**. Profiles $g(\rho)$ obtained from the inversion of the 2 ms average of the DMPX signals using the HFS chords only, the LFS chords only or all the chords. Here, the flux surfaces are not modified. **Bottom**. Same figure but the flux surfaces are modified according to the mode 3 defined in section 4.9.2, with a global radial shift of -0.22 cm and a radial deformation of -0.31 cm. Shot 27481 at 0.4 seconds.

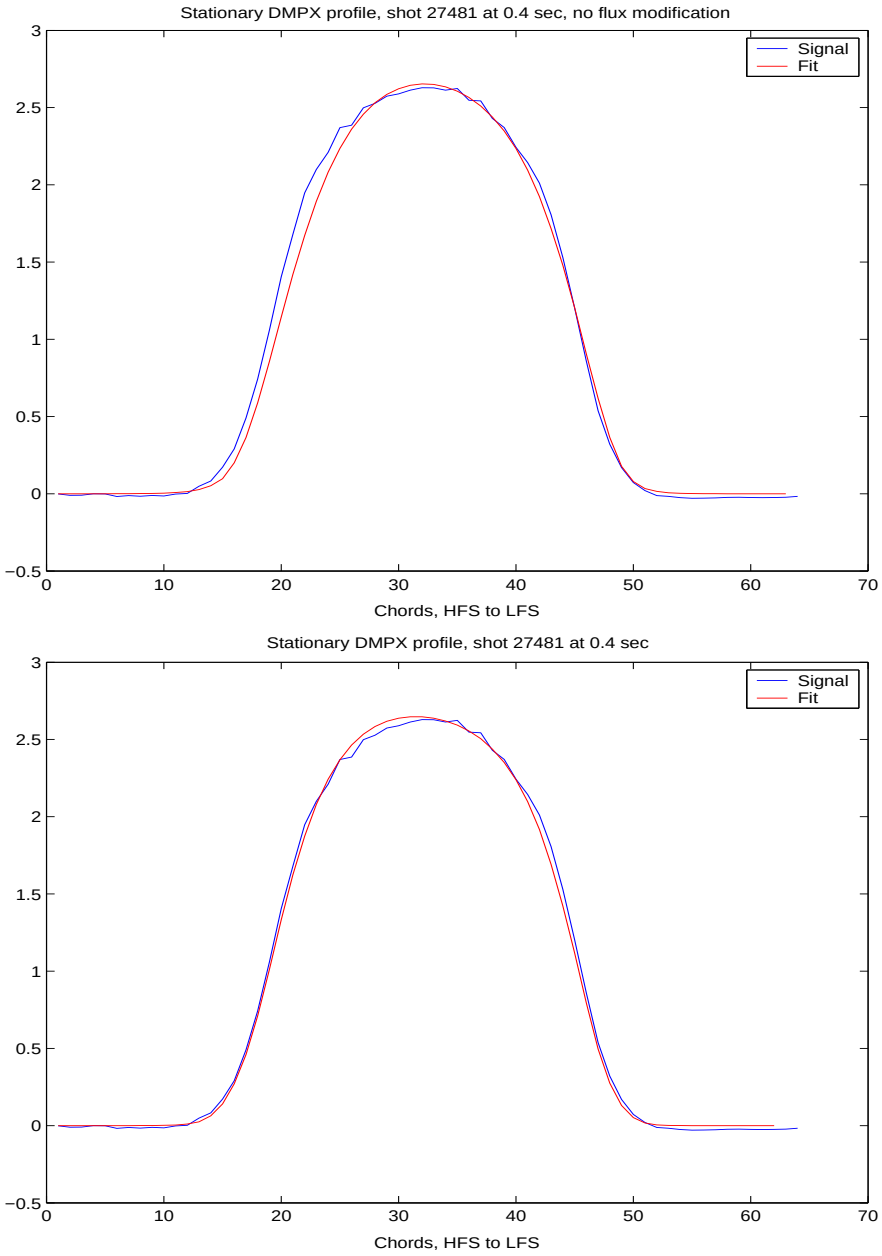

Figure 17: **Top**. 2 ms average of the DMPX signals and fit generated by the reconstructed emissivity profile. Here, the flux surfaces are not modified. **Bottom**. Same figure but the flux surfaces are modified according to the mode 3 defined in section 4.9.2, with a global radial shift of -0.22 cm and a radial deformation of -0.31 cm. Shot 27481 at 0.4 seconds.

Shot	time [s]	dR_1 [cm]	dR_2 [cm]
24141	1.375	1.45	-0.38
27481	0.4	-0.22	-0.31
27481	0.875	-0.18	0.00

Table 1: Values obtained for the modification of the flux surfaces using the mode 3 of the procedure based on the constraint of correspondence between the profile reconstructed with the HFS chords and the LFS chords. dR_1 is the radial translation and dR_2 the radial deformation of the plasma.

5.1.3 Discussion

When looking at the results obtained for the phantoms, we can see on the DMPX profiles (fig. 13 and 15) that the fits and the phantoms are in excellent agreement. On the signals with additional noise, the fit follows nearly exactly the noiseless shape, demonstrating the weak sensitivity of the process to the noise. However, as far as the emissivity profiles are concerned, we can see that although the general trends are respected, the obtained solution is not very good in the low ρ region. At first, we thought that this was only due to the component of the regularization that minimizes the second derivative of the profile. Therefore, we tried to invert the DMPX profile by using only the minimization of the Fisher information. We obtained exactly the same results, with only less local smoothing. The origin of this behaviour has finally been found in the definition of the error for the phantoms. With an error relative to the signal, the smoothing uses the large error allowed close to $\rho = 0$ to decrease the second order derivative or the Fisher information there at the cost of accuracy. In the case of the phantom without noise, the profile obtained by setting an absolute error on the signal is much better in the low ρ region (see figure 18). It can be wondered wether the errors on the real signals are absolute or relative, since if they are relative, the reconstructed emissivity profile will always be too flat in the low ρ regions. In the DMPX, the main part of the error on the signal comes from the electronics and should thus be an absolute error. However, in our analysis, the error is calculated as the standard deviation of the signal on the time window used for the average. All the perturbations occurring in the plasma during that time interval will appear as errors in our treatment, but their relative or absolute feature cannot be known. It is thus hard to say whether the flattening of the profile is spread on the whole profile or concentrated in the low ρ region.

The effect of the procedure of flux modification shown in figures 16 and 17 is striking. Although the deviation between the DMPX signals and the fit is not taken into account in the process, we see that the deviation is reduced after the latter. The comparison between both pairs of figures demonstrates

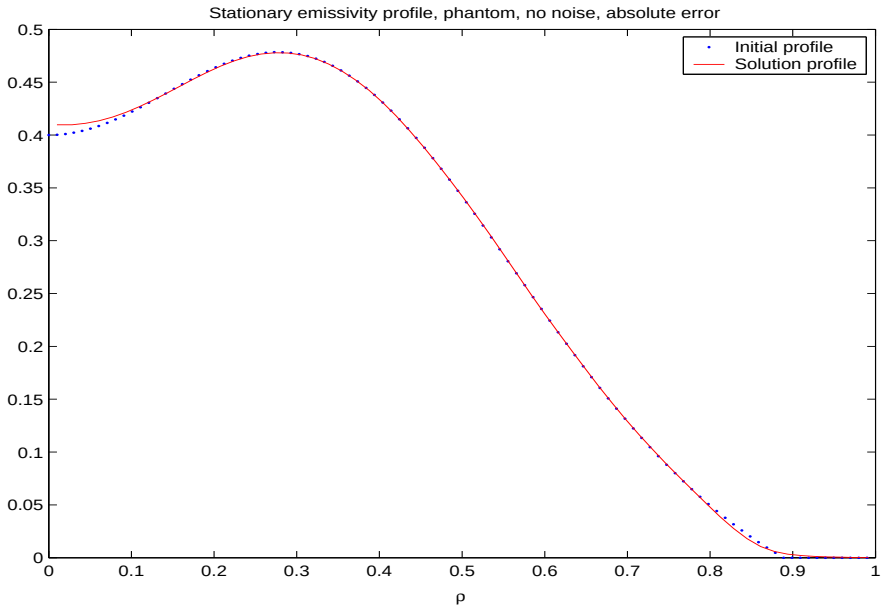

Figure 18: Profile $g(\rho)$ obtained from the inversion of the phantom DMPX signal using all the chords. No noise added on the signal and error set as 0.5% of the mean of the signal. Compare with figure 12.

the relevance of the procedure.

The values given in table 1 are small but exceed the error of the equilibrium reconstruction process, above all in the shot 24141. Nevertheless they have been retained for the rest of the analysis. As the reconstruction process is especially accurate at the edge of the plasma, it could have been interesting to develop a new mode of deformation based on the mode 3 but allowing also vertical deformation. Serious developments and testings of this deformation procedure should be envisaged in order to establish which mode provides the best compromise between the DMPX and the magnetic reconstructions. In this discussion, the argument given by Granetz [2] on the evidence of a discrepancy between the X-ray emissivity contours and the magnetic flux surfaces should not be forgotten. If this argument really holds, it is possible that the procedure of deformation of the flux surfaces simply converges towards the real emissivity level curves without any need of correspondence with the initial flux surfaces (to a certain limit).

5.2 Perturbation profile inversion

The results presented here mainly consist in the tables of values found for the parameters of the islands appearing in three shots, at four different times. The different paths of resolution described in section 4 have all been used, and their respective results are a good indication of the sensitivity and the reliability of the method. All the analysis have been performed with the use of the flux modifications given in table 1. As before, phantoms have been used to assess our work. In table 2, a list of all the parameters of interest that appear in our treatment is given.

Parameters	**Definition**
$\mathbf{t_a}$ [s]	Time of analysis given by the time selection block, see section 4.7.
$\rho_{\mathbf{s,appr}}$	Approximative value of ρ_s found by the process described in section 4.10.4
$\rho_{\mathbf{s}}$	Position of the resonance surface in flux coordinates.
$\rho_{\mathbf{1}}$	Smallest ρ reached by the island. Univocally determined by the value of A (see section 4.10.6).
$\rho_{\mathbf{2}}$	Largest ρ reached by the island. Univocally determined by the value of A (see section 4.10.6).
$\rho_{\mathbf{lufs}}$	ρ value of the last unperturbed flux surface seen from the outside (see section 4.10.1).
$\mathbf{\Delta}\rho_{\mathbf{lufs}}$	Uncertainty on $\Delta\rho_{lufs}$.
$\mathbf{A}$	Factor linked to the amplitude of the flux perturbation (see equation (30)).
$\mathbf{w}$ [m]	Width of the island, obtained from the procedure described in section 4.10.6. Symbol * means that the width is approximative
$\mathbf{I_{rms}}$ [A]	Estimation of the total *rms* value of the current perturbation (see section 4.10.7).
$\mathbf{P}$	Peak value of the perturbation emissivity (see equation (41)).
γ	Rotation sense of the islands (see equation (59)).
$\mathbf{\Phi_0}$	Angle describing the orientation of the islands at the analysed time.

Table 2: Definition of the parameters used in the tables of results.

5.2.1 Phantoms

The behaviour of our inversion procedure has been tested with many phantoms representing different magnetic islands: various mode numbers, width, positions and noise. All gave satisfying results. The results presented below correspond to a mode simulated with the following parameters:

$$\begin{aligned} m &= 2 \\ f_{rot} &= 2000\,[\text{Hz}] \\ \rho_s &= 0.5 \\ w &= 0.05\,[\text{m}] \\ P &= 0.3 \end{aligned}$$

The stationary emissivity profile is defined by:

$$g_{stat} = \left(1 - \rho^2\right)^{1.5} \tag{73}$$

The flux geometry corresponds to shot 27481 at 0.4 seconds. After adding the stationary and the perturbation parts, a relative gaussian noise of 10% has been added to the phantom. Figures 19, 20 and 21 show the results obtained for the FFT, the SVD, and the bandpass filters respectively. Table 3 gives the values obtained for each path of resolution.

Parameters	**FFT**	**SVD**	**Bandpass approx**	**Real**
$\rho_\mathbf{s}$	0.500	0.496	0.504	0.500
A	2051	2298	2279	2176
w [m]	0.048	0.050	0.051	0.050
$\Delta\Phi_0$ [rad]	0.01	0.52	0.09	0.00
P	0.30	0.46	0.33	0.30
γ	+1	-1	+1	+1

Table 3: Table of results for the phantom. The results are presented for the fits of signals produced by the FFT, the SVD and the bandpass filters. The last column gives the real value of the parameters. The parameters are defined in table 2.

Discussion. The uncertainty allowed on ρ_s in the options of *fminbnd* is set to 0.01. As we can see in table 3, all the paths results in a ρ_s value that is comprised in the uncertainty interval. The values of A vary more from one path to the other, but the impact of this variation on the obtained

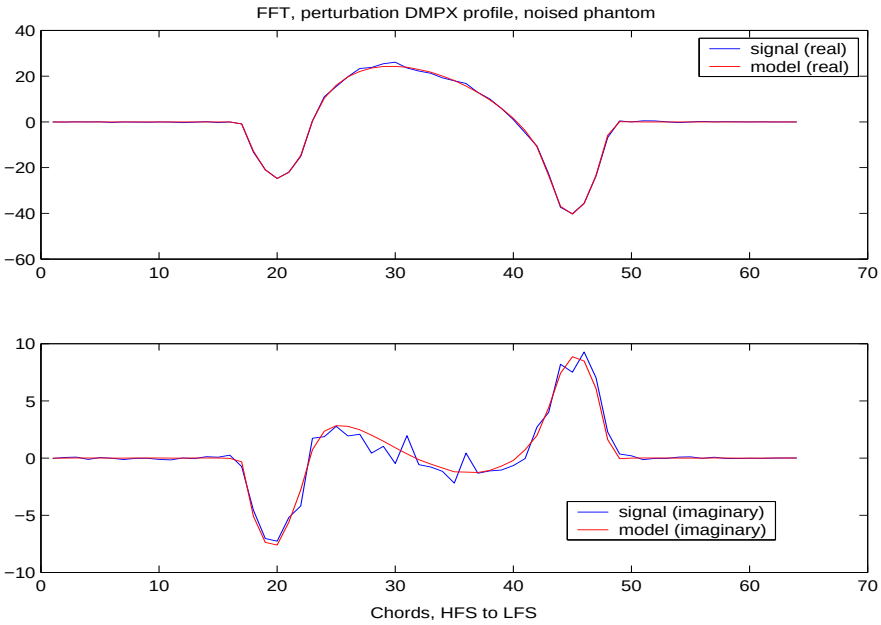

Figure 19: Real and imaginary parts of the dominant frequency component of the FFT of a phantom DMPX signal. The signals corresponding to the fitted perturbation emissivity are drawn in red. Note that both scales of the vertical axis are not the same.

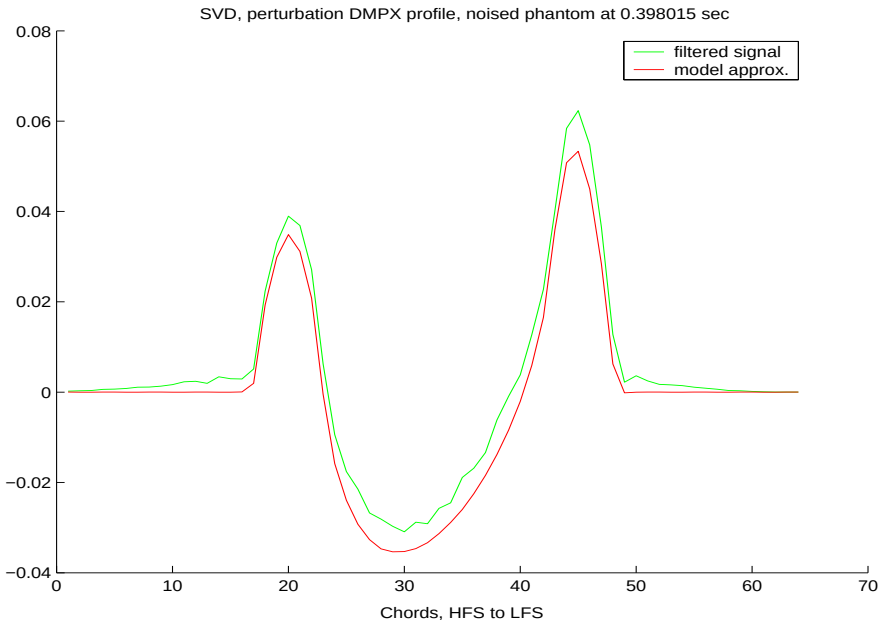

Figure 20: Signal given by the SVD filter of a phantom DMPX signal. The signal corresponding to the fitted perturbation emissivity is drawn in red.

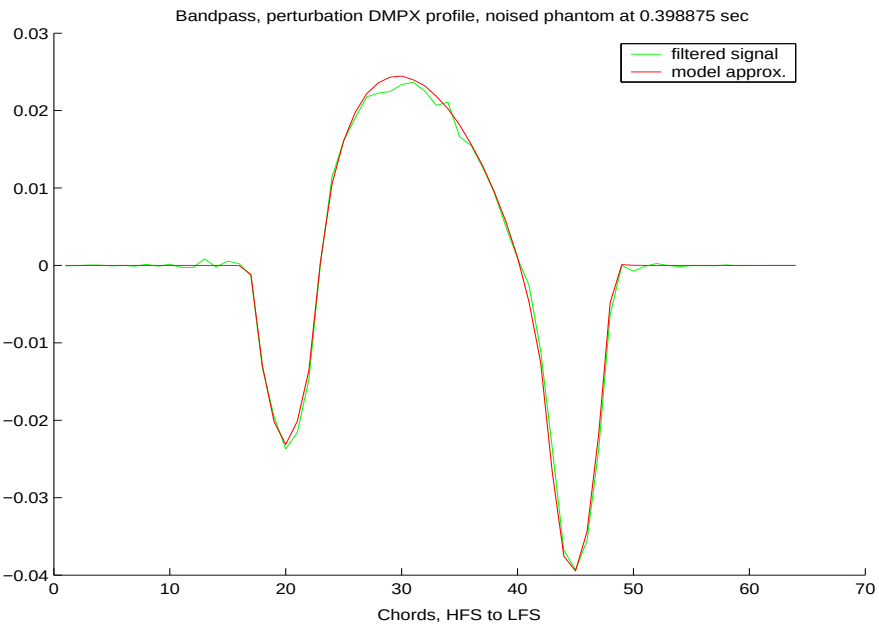

Figure 21: Signal given by the bandpass filter of a phantom DMPX signal. The signal corresponding to the fitted perturbation emissivity is drawn in red.

widths is small and the latter are also very close to the real value. The peak value of the perturbation emissivity function is best estimated in the FFT and the bandpass paths, as well as the initial orientation of the island and the rotation sense. On figure 20, we see that the fit is not excellent because the filtered signal does not exactly correspond to the signal of the originally simulated island. The SVD filter mixes here some other information with the real perturbation signal. It is thus not surprising that the peak value given by the SVD path is wrong.

5.2.2 Assessment of the stability of the ρ_s search procedure

ρ_s is the ultimate parameter of the model. Its exactitude determines that of the others. Its search is based on the minimization of the parameter χ^2_{mean} by *fminbnd*. In order to find a correct value, χ^2_{mean} must be quite smooth in function of ρ_s. Figures 22 and 23 show χ^2_{mean} in function of ρ_s in fits using $\tilde{g}_1$ and g_1 respectively. The signals come from the bandpass block for shot 27481 at 0.4 seconds.

Discussion. The examples of profiles of χ^2_{mean} in function of ρ_s given in figures 22 and 23 have the same behaviour as those of other shots. Therefore, the process of minimization of χ^2_{mean} can be used without any fears on the reliability of the result. Note that taking the fit of the derivative of the signal along the chords into account in the definition of χ^2_{mean} drastically improves the $\chi^2_{mean}(\rho)$ profiles.

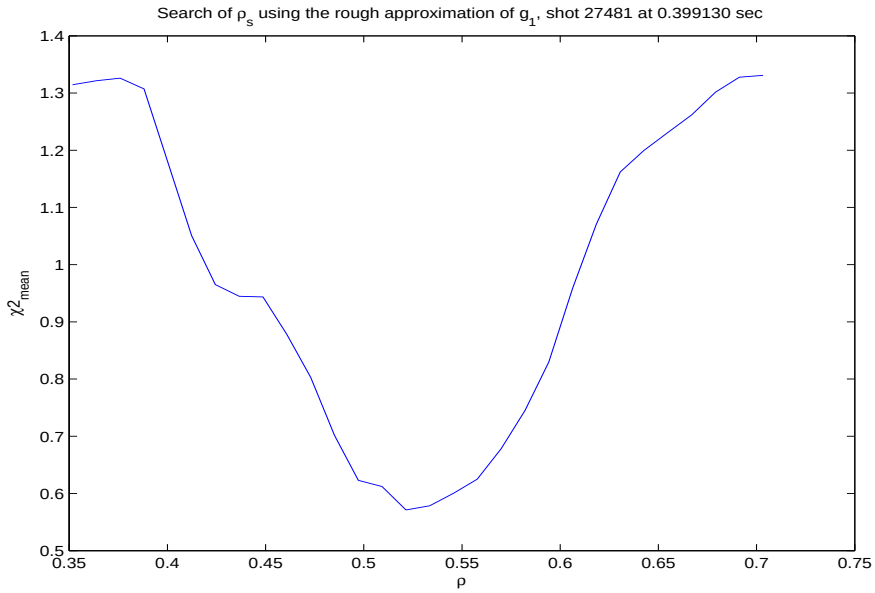

Figure 22: χ^2_{mean} in function of ρ_s using the rough approximation $\tilde{g}_1$ for shot 27481 at 0.399130 seconds.

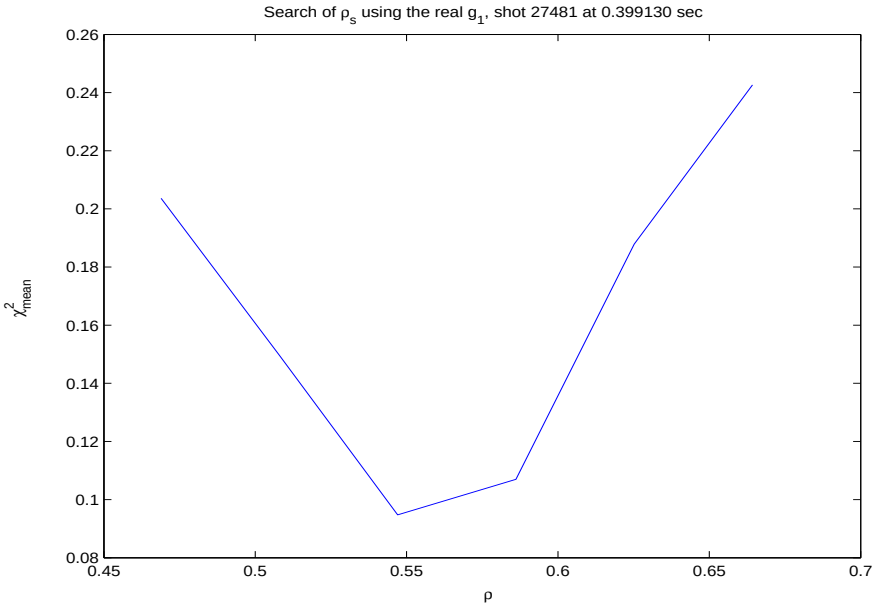

Figure 23: χ^2_{mean} in function of ρ_s using the complete model of g_1 for shot 27481 at 0.399130 seconds.

5.2.3 Shot 22621

Shot 22621 has a mode $m = 1$ with a large amplitude in the vicinity of 1.075 seconds. Its signal frequency is centered at 6050 Hz. This shot has been analyzed by our inversion process and the results are presented below.

Parameters	**FFT**	**SVD**	**Bandpass**	**Bandpass approx**
$\mathbf{t_a}$ [s]	1.0767	1.0766	1.075575	1.075575
$\rho_{\mathbf{s,appr}}$	0.157	0.152	0.153	0.153
$\rho_{\mathbf{s}}$	0.148	0.149	0.155	0.150
$\rho_{\mathbf{1}}$	0.007	0.007	0.011	0.011
$\rho_{\mathbf{2}}$	0.374	0.374	0.379	0.379
$\rho_{\mathbf{lufs}}$	0.388	0.388	0.388	0.388
$\mathbf{\Delta}\rho_{\mathbf{lufs}}$	0.021	0.021	0.021	0.021
A	5698	5779	5881	5881
w [m]	*0.189	*0.189	*0.190	*0.190
$\mathbf{I_{rms}}$ [A]	7821	7931	8075	8075
P	2.77	3.24	3.15	3.15
γ	+1	-1	+1	+1

Table 4: Table of results for shot 22621 at times close to 1.075 seconds. The results are presented for the fits of signals produced by the FFT, the SVD and the bandpass filters. The second and the last columns correspond to linear fits of Φ_0, i.e. fits realized with $g_{1,appr}$. The parameters are defined in table 2.

Parameter	**Rough linear**	**Non-linear**	**Fine linear**
$\mathbf{\Phi_0}$ [rad]	3.72	3.25	3.25

Table 5: Results of the determination of Φ_0 via three different ways, using $\tilde{g}_1$, g_1 and $g_{1,appr}$ respectively. Shot 22621 and bandpass signals.

Discussion. The quality of the obtained fit enables us to get confidence in the model of the islands and its implementation.

The values presented in table 4 show a very small difference between $\rho_{s,appr}$ and ρ_s. Since $\rho_{s,appr}$ can be found in less than a minute while several minutes are required to find ρ_s, $\rho_{s,appr}$ could be used for low computational

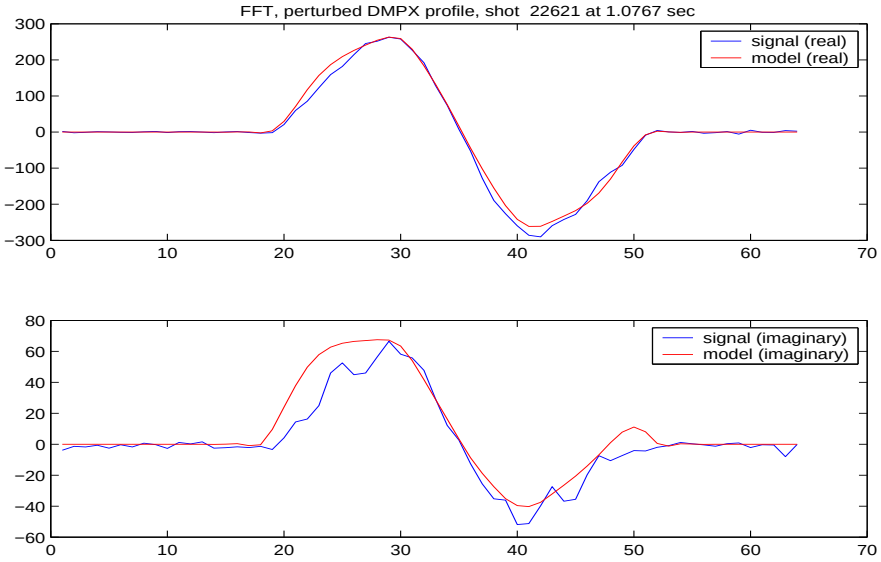

Figure 24: Real and imaginary parts of the dominant frequency component of the FFT of the DMPX signals of shot 22621 at 1.0767 seconds. The signals corresponding to the fitted perturbation emissivity are drawn in red. Note that both scales of the vertical axis are not the same.

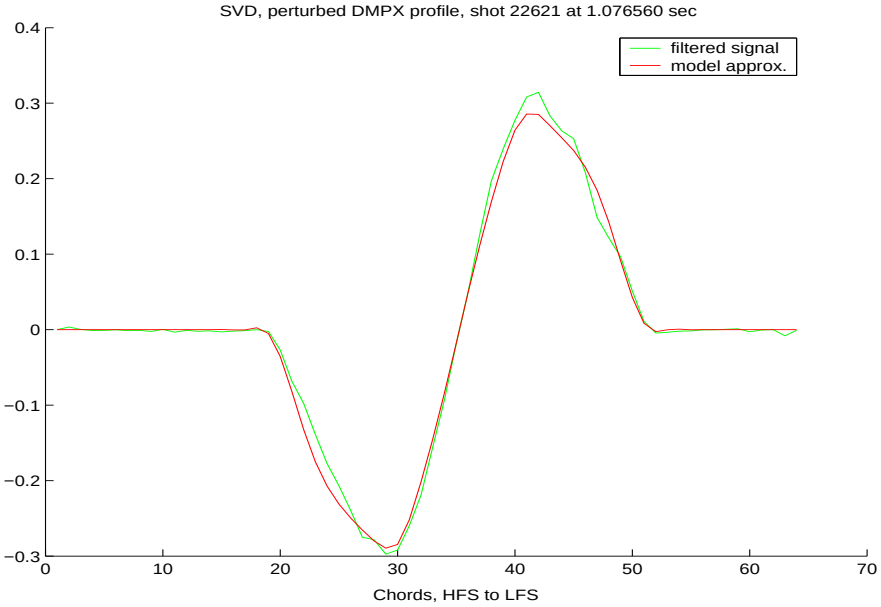

Figure 25: Signal given by the SVD filter of the DMPX signals of shot 22621 at 1.076560 seconds. The signal corresponding to the fitted perturbation emissivity is drawn in red.

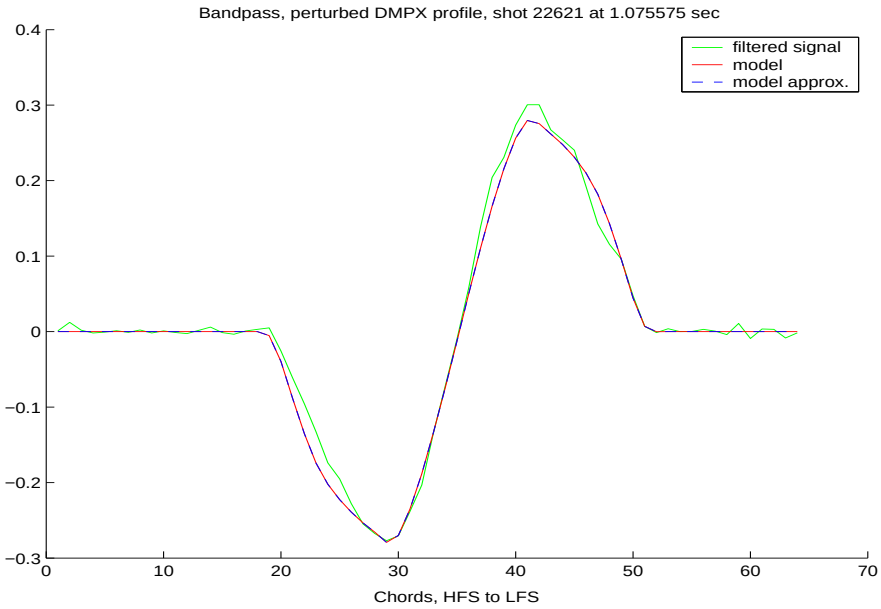

Figure 26: Signal given by the bandpass filter of the DMPX signals of shot 22621 at 1.075575 seconds. The signal corresponding to the fitted perturbation emissivity of type g_1 is drawn in red, and the one corresponding to the fitted emissivity of type $g_{1,appr}$ is represented by the blue dashed line.

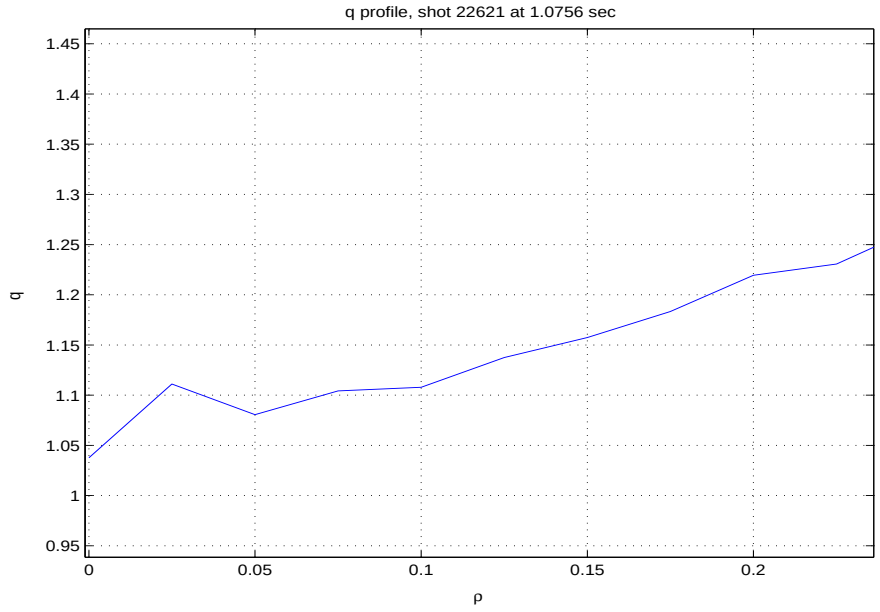

Figure 27: q in function of ρ given by the magnetic equilibrium reconstruction in shot 22621 at 1.0756 seconds.

time applications. Recalling that the uncertainty on ρ_s is set to 0.01, we can see that all the paths of resolution give nearly the same values of ρ_s. This demonstrates the reliability of the process and its accuracy.

Here, according to the parameters of the mode, ρ_1 should be equal to 0. This is not the case because the magnetic axis does certainly not coincide with one of the grid points. Thus, the maximum of ψ_p on the grid does not correspond to $\rho = 0$ but to $\rho = \rho_1$. We also note that the values of ρ_2 agree well with one another. This is also the case for the values of ρ_{lufs}, demonstrating the efficiency of the process of chord selection. ρ_2 and ρ_{lufs} also agree with one another. That shows that ρ_{lufs} is a good choice for the determination of limits or initial values for A and ρ_s.

Here, the determination of the width gives only approximative results (see section 4.10.6). The results are quite relevant with respect to one another despite this approximation.

The only negative aspect, as in the case of the phantom signal, is the fact that the SVD path results in a rotation sense opposed to the others. The origin of this behaviour has not been found in the implementation. It is even more strange when you remember that the bandpass path and the SVD path are the same except in the choice of the signal filter. It is maybe due to an intrinsic behaviour of the SVD itself.

The SVD and the bandpass paths can be subdivided in a path using the approximation $g_{1,appr}$ of g_1 to make a linear fit of Φ_0 and a path using directly g_1 and making a non-linear fit of Φ_0. We have decided to study their difference only with the bandpass path. As we can see in tables 4 and 5 and in figure 26, there are nearly no differences between the results obtained in both ways, except the calculation time that is smaller in the first case. We also note that the Φ_0 found by the rough approximation of g_1 is quite reliable.

As the mode under study is positioned on the surface $q = 1$, it is interesting to have a look at the value of $q(\rho_s)$ where $q(\rho)$ is the profile obtained from the equilibrium reconstruction based on the magnetic field measurements. On figure 27, it can be read $q(\rho_s) \approx 1.16$. When looking at the quality of the obtained fit, we can have enough confidence in the ρ_s found by our process. Therefore, the ρ_s that we find could be used to correct the equilibrium reconstruction, by forcing the q-profile to have the correct value at the given ρ_s.

5.2.4 Shot 24141

Shot 24141 has a mode $m = 2$ with a large amplitude in the vicinity of 1.375 seconds. Its signal frequency is centered at 5350 Hz. This shot has been analysed by our inversion process and the results are presented below.

Parameters	**FFT**	**SVD**	**Bandpass**	**Bandpass approx**
$\mathbf{t_a}$ [s]	1.3738	1.3745	1.374155	1.374155
$\rho_{\mathbf{s,appr}}$	0.640	0.642	0.639	0.639
$\rho_{\mathbf{s}}$	0.658	0.662	0.660	0.660
$\rho_{\mathbf{1}}$	0.474	0.493	0.474	0.465
$\rho_{\mathbf{2}}$	0.777	0.768	0.776	0.777
$\rho_{\mathbf{lufs}}$	0.799	0.863	0.816	0.816
$\mathbf{\Delta}\rho_{\mathbf{lufs}}$	0.065	0.095	0.048	0.048
A	9167	8081	9110	9502
w [m]	0.081	0.072	0.079	0.081
$\mathbf{I_{rms}}$ [A]	9857	8750	9827	10250
P	1.31	2.19	2.01	1.98
γ	+1	-1	+1	+1

Table 6: Table of results for shot 24141 at times close to 1.375 seconds. The results are presented for the fits of signals produced by the FFT, the SVD and the bandpass filters. The second and the last columns correspond to linear fits of Φ_0, i.e. fits realized with $g_{1,appr}$. The parameters are defined in table 2.

Parameter	**Rough linear**	**Non-linear**	**Fine linear**
$\mathbf{\Phi_0}$	3.52	3.36	3.15

Table 7: Results of the determination of Φ_0 via three different ways, using $\tilde{g}_1$, g_1 and $g_{1,appr}$ respectively. Shot 24141 and bandpass signals.

Discussion. The filtered signal is quite noisy with respect to the other shots. Nevertheless, the inversion process does not seem perturbed by this noise.

Most comments are the same as those made for shot 22621. The main differences concern P and A. The P of the FFT path is much smaller than

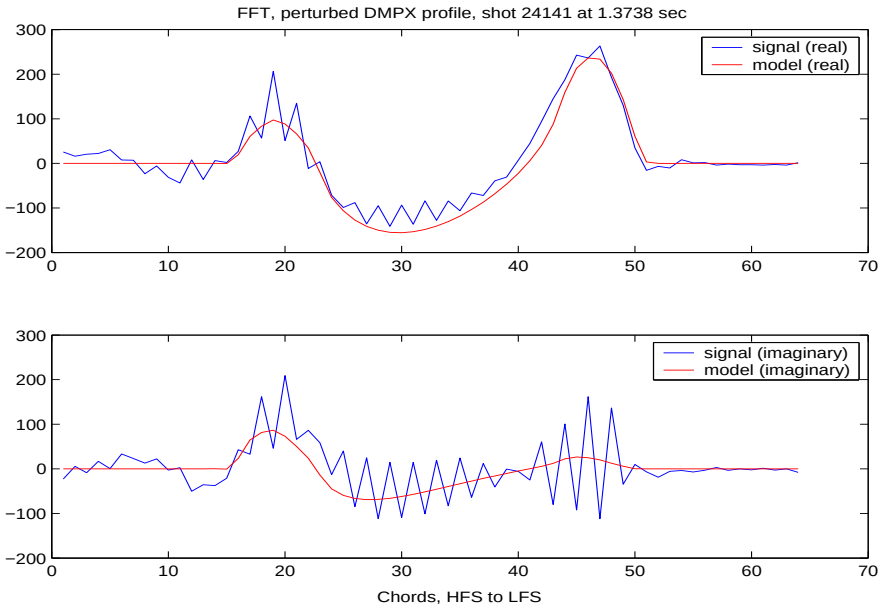

Figure 28: Real and imaginary parts of the dominant frequency component of the FFT of the DMPX signals of shot 24141 at 1.3738 seconds. The signals corresponding to the fitted perturbation emissivity are drawn in red. Note that both scales of the vertical axis are not the same.

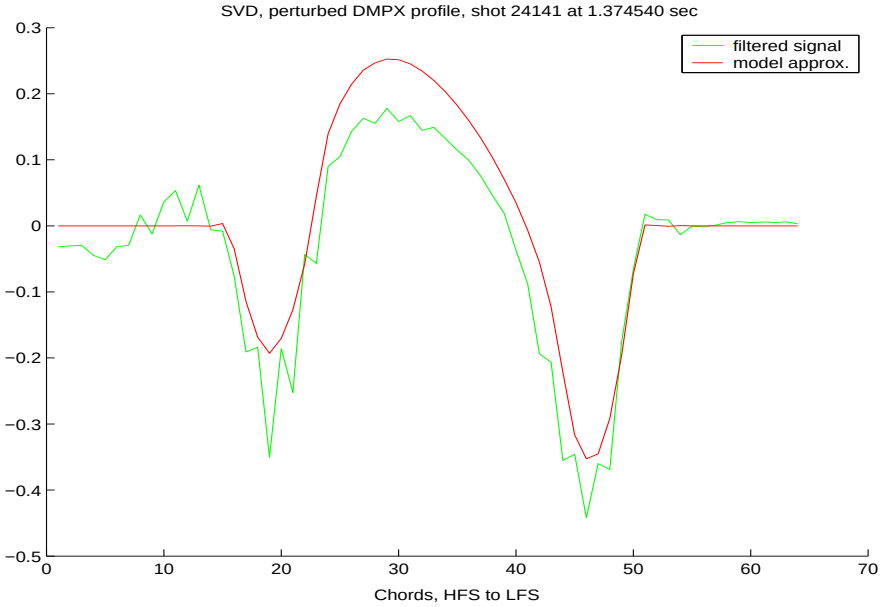

Figure 29: Signal given by the SVD filter of the DMPX signals of shot 24141 at 1.374540 seconds. The signal corresponding to the fitted perturbation emissivity is drawn in red.

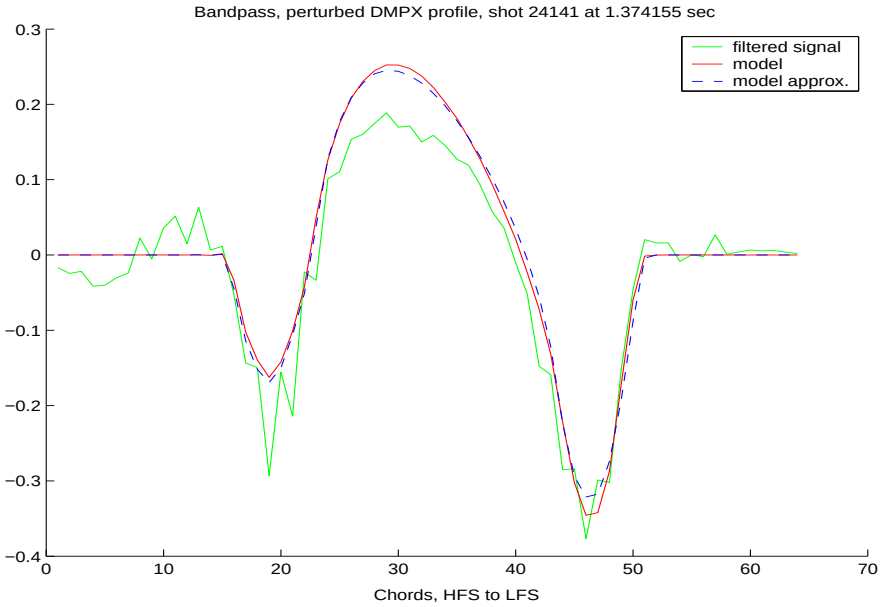

Figure 30: Signal given by the bandpass filter of the DMPX signals of shot 24141 at 1.374155 seconds. The signal corresponding to the fitted perturbation emissivity of type g_1 is drawn in red, and the one corresponding to the fitted emissivity of type $g_{1,appr}$ is represented by the blue dashed line.

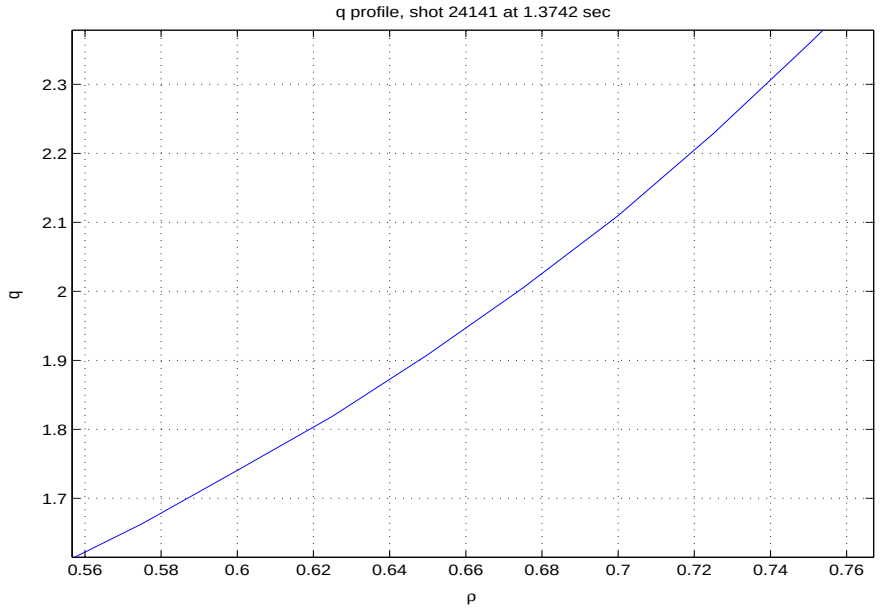

Figure 31: q in function of ρ given by the magnetic equilibrium reconstruction in shot 24141 at 1.3742 seconds.

the others, maybe because of the time dependence of the frequency of the mode. If the latter changes fast, the power at one particular frequency can be underestimated by our method. The small A value of the SVD path can be partly explained by the compensation that occurs through P.

Here, the difference between the Φ_0's determined by the linear fit and the non-linear fit are larger than in shot 22621, but we must keep in mind that the impact of a certain $\Delta\Phi$ on a mode $m = 2$ is twice smaller than on a mode $m = 1$ because Φ must go from 0 to $m \cdot 2\pi$ to achieve a complete round of the cross-section.

5.2.5 Shot 27481 at 0.4 seconds

Shot 27481 has a mode $m = 2$ with a large amplitude in the vicinity of 0.4 seconds. Its signal frequency is centered at 2000 Hz. This shot has been analysed by our inversion process and the results are presented below.

Parameters	**FFT**	**SVD**	**Bandpass**	**Bandpass approx**
$\mathbf{t_a}$ [s]	0.4014	0.3984	0.399130	0.399130
$\rho_{\mathbf{s,appr}}$	0.538	0.516	0.521	0.521
$\rho_{\mathbf{s}}$	0.563	0.548	0.551	0.566
$\rho_{\mathbf{1}}$	0.422	0.411	0.377	0.418
$\rho_{\mathbf{2}}$	0.694	0.660	0.679	0.694
$\rho_{\mathbf{lufs}}$	0.700	0.703	0.703	0.703
$\mathbf{\Delta}\rho_{\mathbf{lufs}}$	0.026	0.027	0.027	0.027
$\mathbf{A}$	4155	3132	4783	4129
$\mathbf{w}$ [m]	0.068	0.062	0.070	0.067
$\mathbf{I_{rms}}$ [A]	4305	3146	4823	4242
$\mathbf{P}$	1.63	2.36	2.21	2.39
γ	+1	+1	+1	+1

Table 8: Table of results for shot 27481 at times close to 0.4 seconds. The results are presented for the fits of signals produced by the FFT, the SVD and the bandpass filters. The second and the last columns correspond to linear fits of Φ_0, i.e. fits realized with $g_{1,appr}$. The parameters are defined in table 2.

Parameter	**Rough linear**	**Non-linear**	**Fine linear**
$\mathbf{\Phi_0}$	3.35	3.21	2.91

Table 9: Results of the determination of Φ_0 via three different ways, using $\tilde{g}_1$, g_1 and $g_{1,appr}$ respectively. Shot 27481 at 0.4 seconds and bandpass signals.

Discussion. Here, the SVD path gives a rotation sense that concords with those of the other paths. Therefore, the error on the rotation sense does not come from a sign inversion in the implementation.

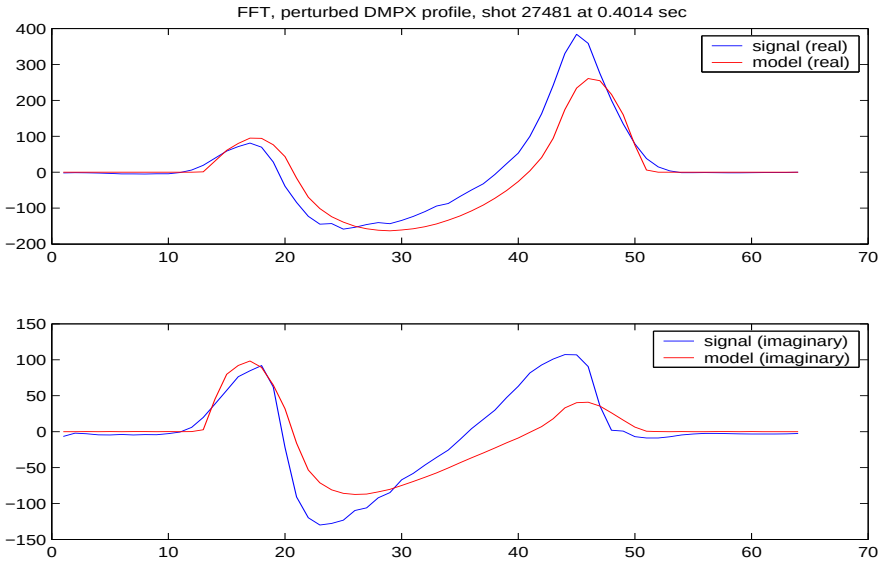

Figure 32: Real and imaginary parts of the dominant frequency component of the FFT of the DMPX signals of shot 27481 at 0.4014 seconds. The signals corresponding to the fitted perturbation emissivity are drawn in red. Note that both scales of the vertical axis are not the same.

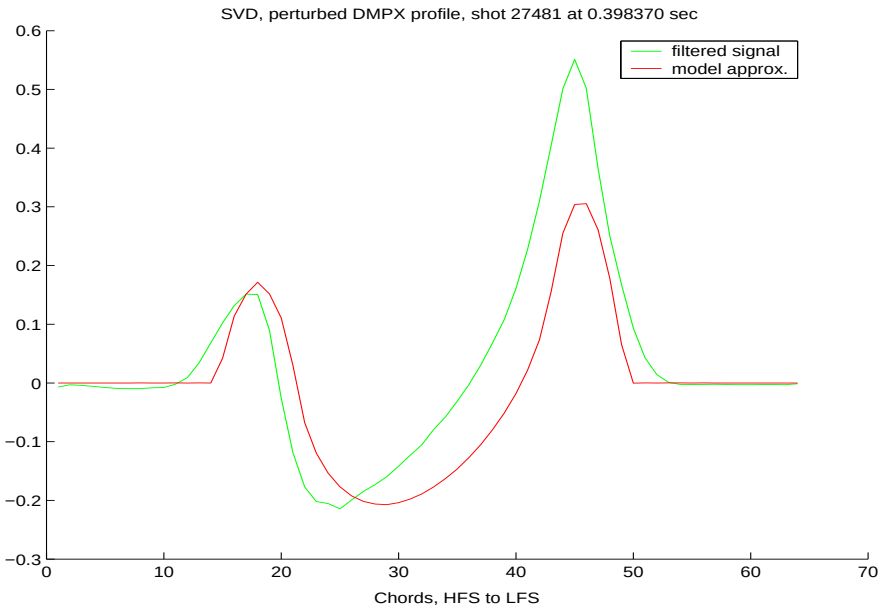

Figure 33: Signal given by the SVD filter of the DMPX signals of shot 27481 at 0.398370 seconds. The signal corresponding to the fitted perturbation emissivity is drawn in red.

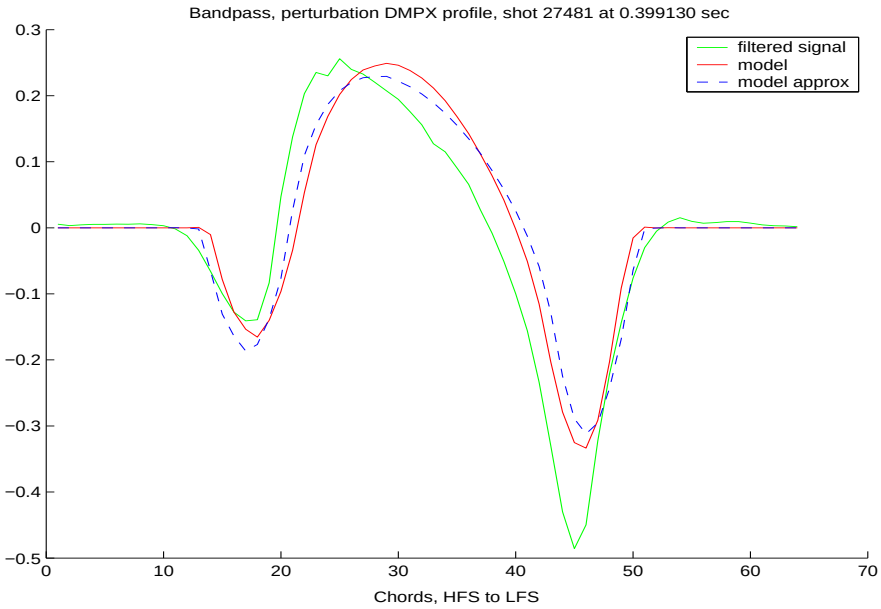

Figure 34: Signal given by the bandpass filter of the DMPX signals of shot 27481 at 0.399130 seconds. The signal corresponding to the fitted perturbation emissivity of type g_1 is drawn in red, and the one corresponding to the fitted emissivity of type $g_{1,appr}$ is represented by the blue dashed line.

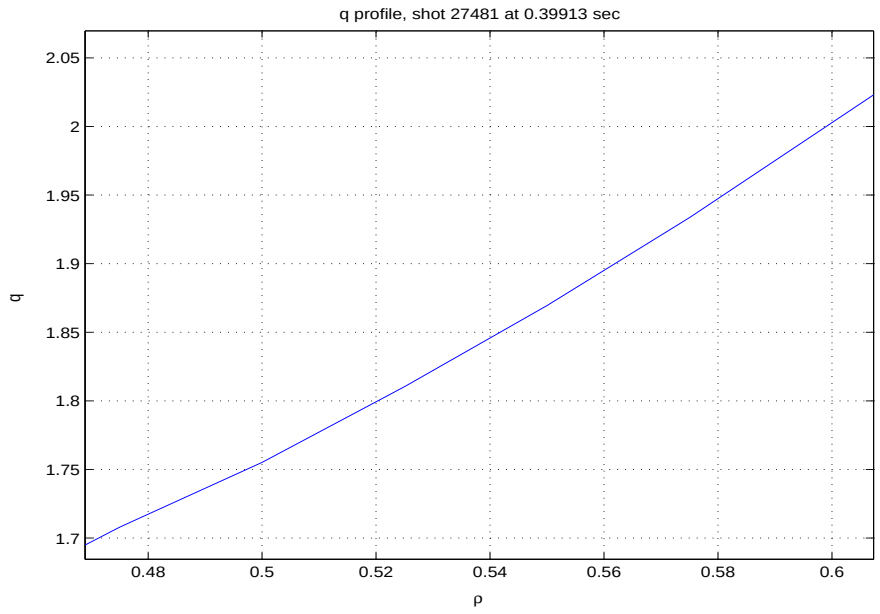

Figure 35: q in function of ρ given by the magnetic equilibrium reconstruction in shot 27481 at 0.39913 seconds.

5.2.6 Shot 27481 at 0.875 seconds

Shot 27481 has a mode $m = 2$ with a large amplitude in the vicinity of 0.875 seconds. Its signal frequency is centered at 3350 Hz. This shot has been analysed by our inversion process and the results are presented below.

Parameters	**FFT**	**SVD**	**Bandpass**	**Bandpass approx**
$\mathbf{t_a}$ [s]	0.8768	0.8768	0.876630	0.876630
$\rho_{\mathbf{s,appr}}$	0.478	0.433	0.431	0.431
$\rho_{\mathbf{s}}$	0.494	0.472	0.482	0.482
$\rho_{\mathbf{1}}$	0.342	0.346	0.344	0.339
$\rho_{\mathbf{2}}$	0.620	0.580	0.581	0.587
$\rho_{\mathbf{lufs}}$	0.610	0.644	0.610	0.610
$\mathbf{\Delta}\rho_{\mathbf{lufs}}$	0.033	0.059	0.033	0.033
A	3129	2048	2126	2488
w [m]	0.065	0.055	0.053	0.057
$\mathbf{I_{rms}}$ [A]	3065	1965	2058	2409
P	0.85	2.99	2.64	2.56
γ	+1	-1	+1	+1

Table 10: Table of results for shot 27481 at times close to 0.875 seconds. The results are presented for the fits of signals produced by the FFT, the SVD and the bandpass filters. The second and the last columns correspond to linear fits of Φ_0, i.e. fits realized with $g_{1,appr}$. The parameters are defined in table 2.

Parameter	**Rough linear**	**Non-linear**	**Fine linear**
$\mathbf{\Phi_0}$	1.05	0.37	0.27

Table 11: Results of the determination of Φ_0 via three different ways, using $\tilde{g}_1$, g_1 and $g_{1,appr}$ respectively. Shot 27481 at 0.875 seconds and bandpass signals.

Discussion. The comments made for the other shots could be applied to this one. Nevertheless, the difference with respect to the original q-profile is more important here than in the other cases.

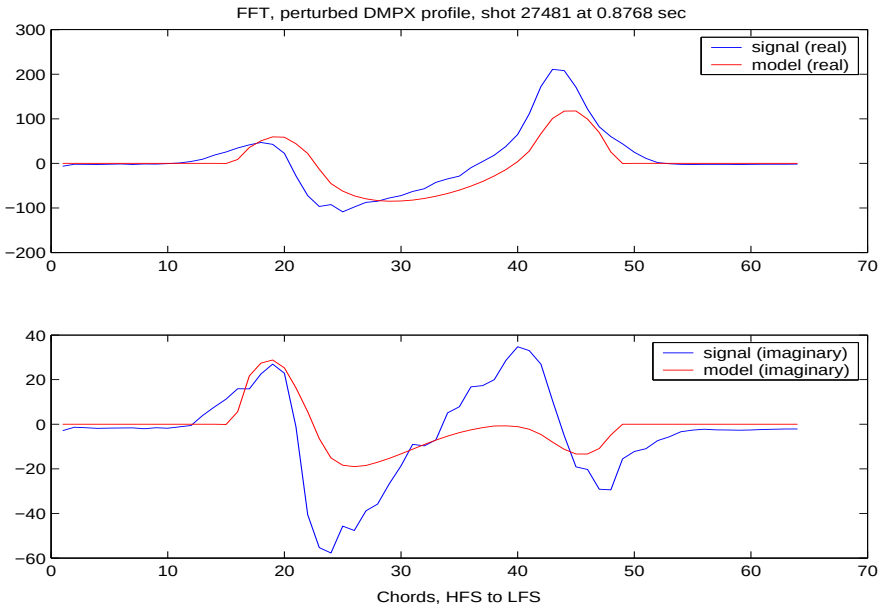

Figure 36: Real and imaginary parts of the dominant frequency component of the FFT of the DMPX signals of shot 27481 at 0.8768 seconds. The signals corresponding to the fitted perturbation emissivity are drawn in red. Note that both scales of the vertical axis are not the same.

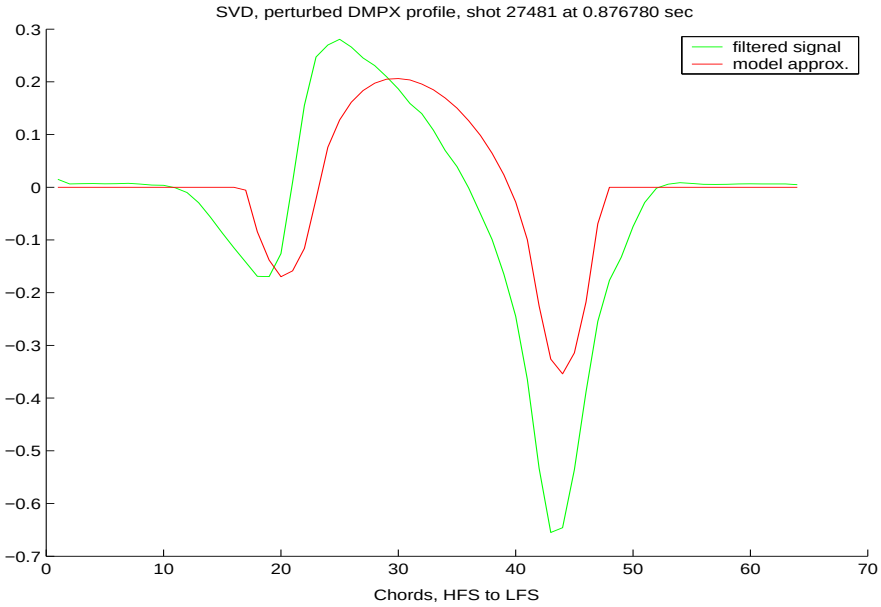

Figure 37: Signal given by the SVD filter of the DMPX signals of shot 27481 at 0.876780 seconds. The signal corresponding to the fitted perturbation emissivity is drawn in red.

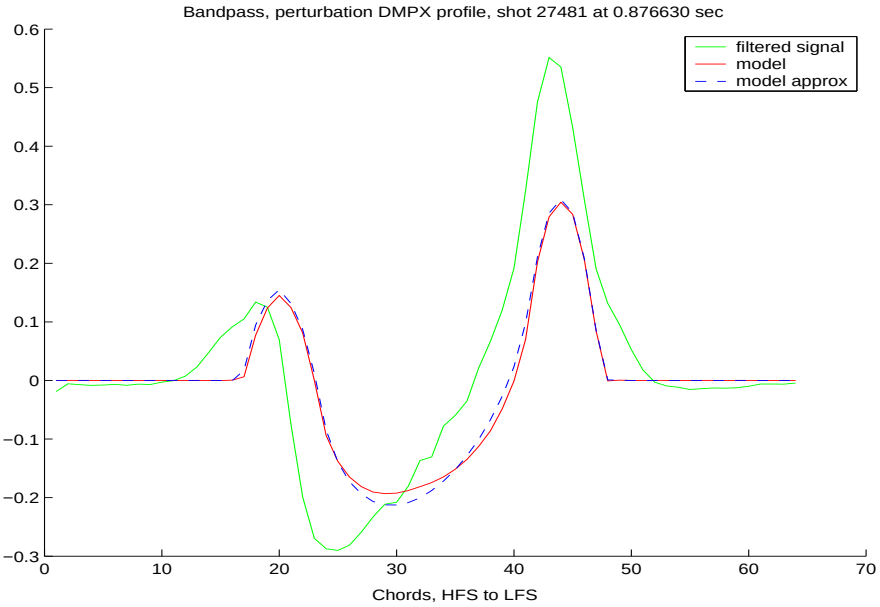

Figure 38: Signal given by the bandpass filter of the DMPX signals of shot 27481 at 0.876630 seconds. The signal corresponding to the fitted perturbation emissivity of type g_1 is drawn in red, and the one corresponding to the fitted emissivity of type $g_{1,appr}$ is represented by the blue dashed line.

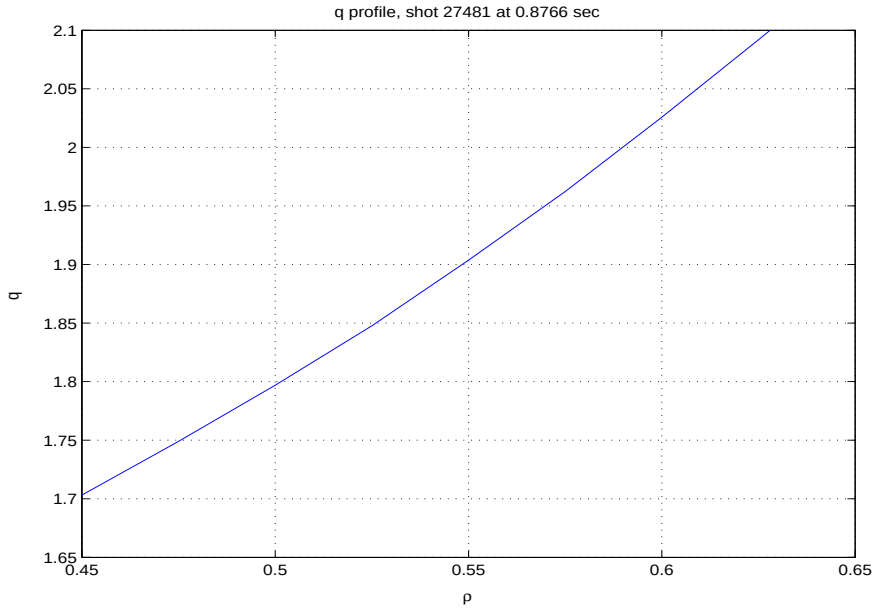

Figure 39: q in function of ρ given by the magnetic equilibrium reconstruction in shot 27481 at 0.8766 seconds.

5.2.7 Discussion of the perturbation inversion process

The results given by the inversion of the phantom have shown that the inversion process is stable and reliable, with a certain reserve for the determination of the rotation sense when using the SVD filter. This last point could be explained as follows: in the SVD filter, only the topos and the chronos corresponding to the second singular value are kept. The perturbation signals are then generated by multiplying the topos and the chronos. If there is originally a phase shift between the chords, it disappears in the operation. Thus, the rotation sense becomes hard to determine. It could be argued that the third topos and chronos should be used in the recombination to avoid this behaviour, but experience has revealed that these components have nothing to see with the desired signals.

The fit obtained in the case $m = 1$ is much better than the fits obtained in the other cases. The model is hence closer to the real perturbation in the case $m = 1$. This behaviour may be due to a better approximation of the helical flux perturbation by a poloidal flux perturbation in the case $m = 1$, where the toroidicity has less impact since the island has less radial extension. It could also be due to the choice of relation between the flux perturbation and the perturbation emissivity. The linear relation is maybe too simple and could be replaced by a power relation.

In our work, ρ_s has always proved to be the best determined parameter. This may be due to the fact that the sharp peaks appearing on the DMPX filtered profile produce well identifiable transition points that are a direct function of ρ_s. This feature is best exploited when the fit of the derivative along the chords is accounted for in χ^2_{mean}.

As far as the introduction of the rotation constraint is concerned, the FFT path is the cleanest way of all the available paths, because the sine and cosine components are intrinsically combined as such in the formulation of $\hat{g}_{1,appr}$. Therefore, the value given by the FFT path for the rotation sense should be considered as the correct one. Since the different examples have shown that the approximation $g_{1,appr}$ can be used as well as g_1, there is no difference of reliability between the FFT path and the others for the other parameters like ρ_s or A. However, the variation in frequency may result in a spreading of the perturbation power among different frequencies, implying a bad estimation of P within the FFT path. Therefore, the bandpass path would be recommended for the determination of P. In conclusion, for reasons of accuracy and computational time, we would advise to use firstly the process of rough approximation of ρ_s, followed by the treatment using the FFT path. The obtained values of ρ_s and A may then be used to obtain P via the signals coming from the bandpass filter. The SVD path should be kept for special

shots where the other procedures failed to find the good parameters. The non-linear fit of Φ_0 could be abandoned.

At present, the determination of the width is not very accurate. This mainly comes from the setting of the dimension of the grid cell. In fact, as we have noted, A must change quite importantly to obtain a variation of w. The only way to detect more finely the impact of small variations of A is to decrease the cell dimension. Unfortunately, this results in an important increase of the computational time. Therefore, we could imagine to design a special routine for the search of A using a very small cell size, with a grid fitted to the dimensions of the islands, and that would be used only when ρ_s is known, as well as a good estimation of A. The number of points along the chords should also be increased, of course.

5.3 Further developments

At the beginning of this work, the question whether it was possible to obtain a simultaneous inversion of the stationary and the perturbation DMPX signals was posed. As described by Ingesson [3], the tomographic inversion is always based on the fitting of some base functions. Starting from what has been done here, we could imagine to make a linear combination of the pixel functions used for the stationary inversion process and of some space functions representing the islands. The fit of the coefficients could be performed under a least square constraint. The functions representing the islands could only be fitted with respect to their amplitude, so that we would need tens of functions to describe the different possible combinations of parameters of a magnetic perturbation. The roughest approximation that could be used for such functions would be $\tilde{\psi}_c$ and $\tilde{\psi}_s$, permitting thus a great reduction of the number of functions since the angular parameter is removed. In our work, we tried to fit the perturbation DMPX signal with all these functions at the same time for 40 values of ρ_s. It failed completely. The fit was good, but the combination of the functions was not physical. To go further, the constraint on the time evolution would be required, but this would correspond to modelize more and more the perturbation. Thus, since the DMPX is a single camera system, we are compelled to use strong assumptions on the 2-D behaviour of the emissivity function, namely the assumption of constant emissivity on flux surfaces and the island model. The inversion process has no advantages in being done simultaneously for the stationary and the perturbation parts.

Further developments could be envisaged in different areas. The first one is the physics of the islands itself. With some cares taken on the determination of the width of the islands, the inversion process could be run at different times of a shot with a slow growing island structure to analyze the dynamics

of the width of the perturbation. The obtained results could also be compared with the results of other diagnostics like *SXR* at TCV (SXR is a complete set of soft X-ray cameras used for tomographic inversion). The equilibrium reconstruction routine could also be modified to use the results of the DMPX analysis. Further developments of the inversion process itself could involve, for instance, the routine that finds the minimum of χ^2_{mean}. A custom routine would be welcome and could decrease the computational time. The model could also be improved by the calculation of a real helical flux perturbation. The choice of a linear relation between the flux perturbation and emissivity could be replaced by a power relation. All these possibilities show that the subject is not exhausted and that some good surprises may result.

6 Conclusion

In this work, we tried to solve the problem of soft X-ray emissivity profile inversion in quasi-axisymmetric equilibria. With this aim in view, we have used the magnetic island model proposed by Reimerdes [5] and developed it to obtain a model of the perturbation emissivity function. Some approximations of this model have also been made to decrease the complexity of the fitting work. In order to achieve the fit of the DMPX data by the model, a whole set of filters have been created. Their main functions are to remove the spikes occurring in the DMPX signals, to select an appropriate time sample, and to obtain the stationary and the perturbation signals. The last developments consist of the procedures of inversion for both types of signals. They involve the determination of the parameters of the poloidal flux modification and some other parameters like the radial flux coordinate of the last perturbed flux surface. These procedures have been optimized to reduce the computational time. Apart from the stationary profile inversion that has been developed from an existing base, the whole work described in this report has been implemented in the form of *Matlab* routines by ourselves (see section 8.3 of the appendix for a dictionary of the routines).

The main results of our work are given below:

- The DMPX is a diagnostic adapted to the study of MHD perturbations, and particularly magnetic islands. The filtered data show clearly the presence of the perturbations and provide a good target for the fitting work.

- The modification of the poloidal flux allows a better fit of the reconstructed DMPX profiles with the experimental data.

- The quality of the obtained fits shows that the model of the magnetic islands corresponds to the experiment to a certain extent, with a best match if $m = 1$. The tests have also revealed that the model is sufficient to obtain a good accuracy on the determination of ρ_s, which is one of the most successful results of this work. The provided estimation of the width of the islands could also be useful for further developments.

- In the actual configuration of the DMPX, it seems useless to develop an inversion process that does not separate the stationary and the perturbation signals. The parameters of the islands are much better determined in our way.

- The developed method has a high degree of automation and may be applied to different shots with a minimal prior work.

To conclude, this project has allowed us to get a better understanding of the problem of magnetic perturbations, and especially magnetic islands. We wish that our work is robust enough to provide a base for further developments. Above all, we hope that it will contribute to the understanding of energy diffusion and to the improvement of the confinement in tokamaks.

7 Acknowledgments

We thank specially Jean-Marc Moret, Yann Camenen and Andrea Scarabosio for their advice, their help, and their availability. We also thank the CRPP direction for their motivation to train students and the quality of the proposed projects.

8 Appendix

8.1 Additional theory

8.1.1 Regularization by the second order derivative

The second order regularization favours a solution of (7) with minimal curvature. It minimizes the norm of a vector containing the Laplacian of the solution $\mathbf{g}$. The object function may hence be defined by:

$$O(\mathbf{g}) = \| \triangle \mathbf{g} \|^2 = (\triangle \mathbf{g})^T \cdot (\triangle \mathbf{g}) \tag{74}$$

If $\triangle$ denotes a matrix representation (finite differences) of the Laplacian, we may write:

$$O(\mathbf{g}) = \mathbf{g}^T \cdot \triangle^T \cdot \triangle \cdot \mathbf{g} =: \mathbf{g}^T \cdot \mathbf{H} \cdot \mathbf{g} \tag{75}$$

The disadvantage of this definition for the object function is that it will always tend to flatten the deduced profile.

8.1.2 Regularization by the Fisher information.

The Fisher information I_F of a probability distribution $p(x)$ is defined by:

$$I_F = \int \frac{p'(x)^2}{p(x)} dx \tag{76}$$

where the prime denotes the derivative with respect to x. By identifying I_F as the soft X-ray emissivity, we see that minimizing the Fisher information of g implies a smoothing localized to the small g regions, regions of the plasma where the information contained in the X-rays is the least accurate. The implementation of the concept is tractable if the latter is reduced to a weighted first order linear regularization. We start by defining $O(\mathbf{g})$ as:

$$O(\mathbf{g}) = (\nabla_\mathbf{x} \cdot \mathbf{g})^T \cdot (\nabla_\mathbf{x} \cdot \mathbf{g}) + (\nabla_\mathbf{y} \cdot \mathbf{g})^T \cdot (\nabla_\mathbf{y} \cdot \mathbf{g}) \tag{77}$$

where $\nabla_\mathbf{x}$ and $\nabla_\mathbf{y}$ are finite-difference matrix representations of the derivatives with respect to x and y. It may be written:

$$O(\mathbf{g}) = \mathbf{g} \cdot ({\nabla_\mathbf{x}}^T \cdot \nabla_\mathbf{x} + {\nabla_\mathbf{y}}^T \cdot \nabla_\mathbf{y}) \cdot \mathbf{g} =: \mathbf{g} \cdot \mathbf{H} \cdot \mathbf{g} \tag{78}$$

The introduction of the weighting, corresponding to the Fisher information, is performed by adding a diagonal weight matrix $\mathbf{W}$, where $W_{ii} > 0$:

$$\mathbf{H} = {\nabla_\mathbf{x}}^T \cdot \mathbf{W} \cdot \nabla_\mathbf{x} + {\nabla_\mathbf{y}}^T \cdot \mathbf{W} \cdot \nabla_\mathbf{y} \tag{79}$$

In order to keep the method linear, an iterative process is used for the definition of $\mathbf{W}$. The starting point is given by $\mathbf{W} = \mathbf{1}$, the identity matrix. Equation (12) is solved with the $\mathbf{H}$ given by (79). The obtained $\mathbf{g}$ is used to determine a new weight matrix $\mathbf{W}$ such that:

$$W_{ij} = \begin{cases} \frac{1}{g_i} \cdot \delta_{ij} & \text{if } g_i > 0 \\ W_{max} \cdot \delta_{ij} & \text{else} \end{cases} \tag{80}$$

where δ_{ij} is the Kronecker symbol and W_{max} is the value obtained for the smaller positive g_i. The new $\mathbf{W}$ is then used for a new solution of equation (12) and so on until the difference between the values of $\mathbf{W}$ become less than a certain value. We can resume this by:

$$\left(\mathbf{K}^T \cdot \mathbf{K} + \alpha \mathbf{H}^{(n)}\right) \cdot \mathbf{g}^{(n+1)} = \mathbf{K}^T \cdot \mathbf{f} \tag{81}$$

where the (n) and $(n+1)$ superscripts correspond to the iteration number. For each iteration, the value of α is chosen to give the best fit as possible. Generally, only 3 or 4 iterations are needed to find a stable expression of $\mathbf{W}$.

8.1.3 Straight field line angle θ^*

In tokamaks, the toroidal geometry implies that the toroidal magnetic field has a strength inversely proportional to the main radius coordinate. Consequently, the angle of a field line with respect to the toroidal direction (*pitch angle*) varies in function of the poloidal angle. In order to exclude the effects of toroidicity and shaping, a poloidal variable $\theta^*(\theta, q)$ is introduced, so that the magnetic field follows straight lines in the $\theta^* - \varphi$ plane, for a given q. It yields:

$$\frac{\mathbf{B} \cdot \nabla \theta^*}{\mathbf{B} \cdot \nabla \varphi} = \frac{1}{q} \tag{82}$$

Generally, an axisymmetric magnetic field $\mathbf{B}$ can be written:

$$\mathbf{B} = I(\psi_p) \nabla \varphi + \nabla \psi_p \times \nabla \varphi \tag{83}$$

where $I(\psi_p)$ is a scalar function, ψ_p is the poloidal flux and φ the toroidal angle coordinate. Replacing (83) into (82) gives:

$$\underbrace{\nabla \psi_p \times \nabla \varphi \cdot \nabla \theta}_{J} \cdot \frac{\partial \theta^*}{\partial \theta} = \frac{1}{q} \frac{I(\psi_p)}{R^2} \tag{84}$$

The $1/R^2$ factor appears because of the $R-$dependence of $\nabla \varphi$, where R is the major toroidal radius. J is the Jacobian of the coordinate transformation

of the flux coordinate system $(\psi_p, \varphi, \theta)$ into the cylindrical coordinate system (R, φ, Z). J is greatly simplified when the toroidal symmetry assumption is taken into account, and may be calculated with the poloidal flux given by the equilibrium reconstruction. Integrating equation (84) over θ and normalising it by the condition $\theta^*(2\pi) = 2\pi$ yields:

$$\theta^*(\theta, q) = 2\pi \frac{\int_0^\theta d\theta \, (R^2 J)^{-1}}{\int_0^{2\pi} d\theta \, (R^2 J)^{-1}} \tag{85}$$

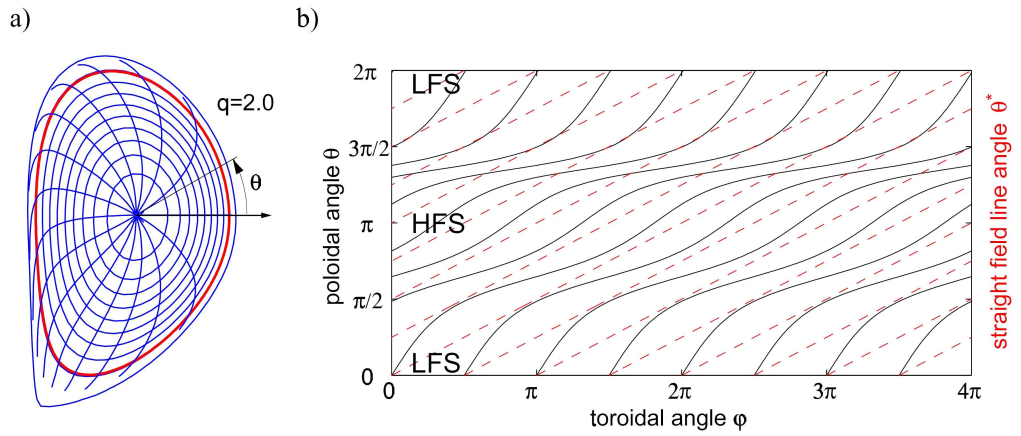

Figure 40: In figure (a), the level curves of θ^* are superposed on the poloidal cross-section of the flux surfaces. The flux surface represented in red is the $q = 2$ surface. In figure (b), the trajectory of the magnetic field lines on that surface are represented in the coordinate systems (φ, θ) and (φ, θ^*). Courtesy of Reimerdes [5].

The flux coordinate system is useful for working in tokamak plasmas because it converts the complicated cross-section of the plasma into a circular one. Now, using the new coordinate θ^* instead of θ enables, in addition, to obtain a circular symmetry in the cross-section. This coordinate is capital in defining the angular periodicity of the magnetic islands, which must take into account the variation of the pitch angle along the field lines. Figure 40 shows the different properties of θ^*. Note that the convention of definition of θ used in our work does not correspond to that appearing in this figure. In fact, for reasons of simplicity in the implementation, our convention defines the position $\theta = 0$ as the high field side of the midplane of the cross-section and the positive sense of θ as the clockwise direction.

Another property of θ^* is the perpendicularity of its level curves to the magnetic field lines. Equation (82) may be rewritten and developed as:

$$\mathbf{B} \cdot \nabla\theta^* = \frac{1}{q}\mathbf{B} \cdot \nabla\varphi = \frac{1}{q}B_\varphi \frac{1}{R} \tag{86}$$

Using the approximation $q = \frac{rB_\varphi}{RB_p}$ where r is the radius measured from the magnetic axis and B_p is the poloidal magnetic field, equation (86) becomes:

$$\mathbf{B} \cdot \nabla\theta^* = B_p \tag{87}$$

As $\nabla\theta^*$ is perpendicular to the level curves of θ^*, the latter are perpendicular to the poloidal magnetic field, and thus to the flux surfaces. This demonstration is done without the approximative expression of q in Miyamoto [4, p. 170].

8.1.4 Toroidal and helical flux

Formally, the *toroidal flux* ψ_t is defined as the magnetic flux through a given poloidal surface. It is logical then to use the flux surfaces defined by ψ_p as the reference surfaces. It yields:

$$\psi_t(\psi_p) := \int_{S(\psi_p)} dS\, B_t \tag{88}$$

where B_t the toroidal magnetic field, and $S(\psi_p)$ is the poloidal surface delimited by the last closed flux surface and the shell corresponding to ψ_p. This odd definition of the surface of integration is due to the desire to have an identical global behaviour between ψ_p and ψ_t. q may be defined by:

$$q := \frac{d\psi_t}{d\psi_p} \tag{89}$$

Expression (89) shows the redundancy occurring between ψ_p, ψ_t and q. At TCV, ψ_t is not stored in the data basis and is calculated with (89).

As it has been seen in section 2.1.4, the magnetic islands are three dimensional phenomena. The islands are modelized by a current perturbation flowing at the resonance surface q_s and along the magnetic field lines. Such a current implies both poloidal and toroidal magnetic field components. The unique way to describe both at the same time is to use the concept of *helical flux*. The helical flux is a magnetic field line invariant that labels the flux surfaces in the presence of an isolated magnetic island chain. It is calculated on surfaces that have a helicoidal geometry corresponding to the magnetic

field lines of the chosen resonance surface. Rosenberg *et al.* [6] give a general way to calculate the helical flux corresponding to a given resonance surface. They find that the helical equilibrium flux ψ_0^* across the whole plasma can be calculated from the poloidal flux ψ_p and the toroidal flux ψ_t as:

$$\psi_0^* = \psi_{p,0} - \frac{1}{q_s}\psi_{t,0} \tag{90}$$

We give now another approach of expression (90) that uses the concept of magnetic field rather than that of flux. The poloidal flux of a zero shear field (i.e. $q = constant$) may be written as $\psi_{p,q=q_s} = \psi_t/q_s$ (see equation (89)). Equation (90) is thus equivalent to subtracting an artificial zero shear field with a safety factor q_s from the equilibrium field. The resulting magnetic field changes sign at the resonance surface (along $\hat{e}_r$). This is a necessary condition for the apparition of the island topology when combining with the field perturbation. In this way, a small current perturbation always creates magnetic reconnection, and thus magnetic islands.

This combination always results in the presence of an extremum of ψ_0^* at q_s. The position of this extremum is mainly determined by q since ψ_t is a function of q. Due to the toroidal symmetry of the equilibrium field, and to the angular periodicity of the perturbation, the nature of the extremum is not important for our work. Therefore, ψ_0^* is redefined after calculation such that the extremum is always a maximum (i.e. turned upside down if needed).

8.2 Additional descriptions of the data processing blocks

8.2.1 Signal pre-processing

The spike removal process operates as follows:

- The routine checks that each detector has a valuable signal. If needed, the missing signals are interpolated by a cubic spline. The interpolation is performed only if there are no consecutive problematic detectors.

- The time derivative of each signal is calculated and for each detector, a level is determined by the standard deviation of the time derivative and the mean of its absolute value. Each point above this level is considered as belonging to a spike.

- As there is no reliable information during spikes, they must be fully removed. From each point labelled as a spike, the time derivative is followed in both temporal directions and the samples are recorded as

belonging to a spike until the derivative changes its sign or goes to zero. In this way, a matrix of the same size as the one of the data is formed, and contains 0 or 1 if the data point is in a spike or not. Only the samples detected as belonging to a spike are replaced by interpolated values.

- In order to have a minimal impact of the filter on the temporal behaviour, the replacement of the data that are in spikes is done by the means of an interpolation along the detection wires only. The latter uses a cubic spline interpolation with a tension of 10 and a constraint on the derivatives at each edge (these parameters correspond to the function *interpos* written for *Matlab* by the CRPP team). This process requires the absence of spikes on the first and last wires. Therefore, those wires are always interpolated along time, before being interpolated along the detector axis.

- In the presence of large spikes along the wires, the above process fails and results in the creation of even larger artificial spikes. To prevent this behaviour, the routine is designed to identify all the spikes that extend over more than seven wires and to replace them by a local two dimensional interpolation performed by the *Matlab griddata* function.

- The routine is also designed in order to pass the signals several times through the filtering process, such that a maximum of spikes are detected and removed and that no artificial spikes are created.

8.2.2 Bandpass filter

The filter uses the *filtfilt* function of *Matlab* with the order set to 2. The advantage of *filtfilt* over a usual filter design is that it implies no phase distortion. This is achieved by passing the signal in one direction in the filter, then passing it a second time in the other direction (starting from the end). Note that this process loses the causality of the signal, but as we are mainly interested in a sine function, it is not really important. This function of *Matlab* also takes care of the edges of the filtered signal and prevent artificial peaks from being created.

8.2.3 SVD

The Singular Value Decomposition (**SVD**) is a mathematical tool used in linear algebra for matrix decomposition. Formally, it is defined by:

$$\mathbf{M} = \mathbf{U} \cdot \mathbf{S} \cdot \mathbf{V}^T \tag{91}$$

where $\mathbf{M}$ is the $L \times C$ matrix that is decomposed, $\mathbf{U}$ and $\mathbf{V}$ are $L \times L$ and $C \times C$ unitary matrices respectively. $\mathbf{S}$ is a diagonal matrix of rank K, the rank of $\mathbf{M}$. By convention, the diagonal elements of $\mathbf{S}$, the *singular values*, are ordered from the largest to the smallest.

This decomposition is equivalent to the so-called *biorthogonal decomposition*, that consists in decomposing a function of two variables into a combination of two sets of functions of only one variable each. Applied to our case, this may be written:

$$s(d,t) = \sum_{k=1,\ldots,K} S_k U_k(d) V_k(t) \tag{92}$$

where $s(d,t)$ is the signal given by the detector (or wire) d at time t. U_k and V_k are the columns of $\mathbf{U}$ and $\mathbf{V}$ respectively. They are called *topos* and *chronos* and are orthogonal eigenmodes. With the SVD, most of the signal is contained in the first terms of the sum, and the truncation of the end of the expansion corresponds to the best approximation of the signal in the least square sense.

8.2.4 Time selection

For our work, the most interesting times are not only the times where the average of the absolute value of the signals across the detectors is maximal, but also the times where the signals show the characteristic signature of the mode, i.e. the times where the orientation of the magnetic islands is such that the mode number m can be easily identified from the analysis of a signal profile along the detectors. Hence, the routine first identifies the times where the number of extrema along the detectors is equal to $m+1$, and then selects the times among them that have the largest signal in absolute value.

The first selection uses an interpolation of the signals along the detectors in order to remove the noise. As the profiles along the detectors must pass by zero between each extremum at the interesting times, the selection is then based on the number of crossing of a given level by the said profiles.

8.2.5 Fourier transform filter

This block operates as follows:

- A fast Fourier transform (**FFT**) of each DMPX signal is performed.
- The unnecessary part of the negative frequencies is removed, as well as the signal under 1 kHz.

- Let us call $< \hat{f}_1 > (\nu)$ the average along the detectors of the amplitude of the signal Fourier transform. An analysis is performed on $< \hat{f}_1 > (\nu)$ in order to determine the dominant frequency of each present mode. This analysis is constructed as follows: the absolute maximum of $< \hat{f}_1 > (\nu)$ is determined and the corresponding frequency stored. Then, $< \hat{f}_1 > (\nu)$ is set to zero on a 3 kHz interval around that frequency, and the next maximum is determined. The loop ends when the value of $< \hat{f}_1 > (\nu)$ at the maximum falls under a level determined by twice the value of the mean of $< \hat{f}_1 > (\nu)$.

- Since the frequency of a magnetic island can evolve with time, as well as its width and amplitude, the time interval used for the calculation of the FFT must be reduced around the most interesting time. Therefore, the bandpass filter block is called with the frequency limits given by a 2 kHz interval around the mode frequency determined above. The time selection block uses the data given by the bandpass filter to define a new time interval for the analysis.

- An FFT is performed on the new time interval.

- The precise frequency limits of the mode are determined with a level test on the new $< \hat{f}_1 > (\nu)$.

8.2.6 Stationary inversion: further considerations

The error of the fit with respect to the measurements is resumed by a parameter χ_2 defined by:

$$\chi^2 := \frac{(\hat{\mathbf{K}} \cdot \mathbf{g} - \hat{\mathbf{f}})^T \cdot (\hat{\mathbf{K}} \cdot \mathbf{g} - \hat{\mathbf{f}})}{\sum_i \sigma_i^2} \tag{93}$$

where the hat means that the weighting relative to the uncertainty is not used. σ is a vector containing the absolute errors on the measurements.

The value of α determines the proportion of smoothing that is allowed. A target value of χ^2 must hence be defined. It should reflect the compromise between the smoothing and the accuracy. The method adopted here operates as follows: a subset of pixels is taken out of the original set such that $N_p = N_c/2$. A new transfer matrix is calculated on the basis of the original $\mathbf{K}$. A direct inversion based on the least square fit and taking the edge conditions into account is performed and results in a certain value of χ^2. The latter may be seen as the value that would correspond to a minimal

smoothing. Including the smoothing, the target value of χ^2 is then defined by:

$$\chi^2_{target} = max\left\{min\left\{2\cdot\chi^2, \chi^2 + \frac{1-\chi^2}{2}, 1\right\}, 0.1\right\} \tag{94}$$

χ^2_{target} is smaller than 1 to avoid false solutions and larger than 0.1 to assure a sufficient smoothness.

At the end of the inversion process, a test of the smoothness is done on the obtained g-profile. It looks for consecutive alternated extrema of g along ρ. If the test routine finds such oscillations, it compares the local average of the derivative of g at these positions with the standard deviation of that derivative along the whole profile. If the local average is larger than the half of the standard deviation, the routine restarts the inversion process with a doubled value of χ^2_{target}. If the test fails again, the process is restarted until χ^2_{target} equals 1. The next step is too increase β until it reaches 1. If the test still fails, the errors on the signal are doubled and the process starts once more with $\chi^2_{target} = 0.1$ and $\beta = 0.1$.

8.2.7 Determination of $\rho_{\mathbf{lufs}}$

Since ρ_{lufs} is one of the crucial parameters of the inversion procedure, it is given by the combination of two different ways of identifying the chords.

The first method calculates the standard deviation along the time coordinate for each chord and compares it with its mean along the chords. Under a certain level, the corresponding chords are identified as being outside the perturbation. If the analyzed signals come from the FFT filter, the standard deviation is simply replaced by the amplitudes of the signals at the frequency corresponding to the maximal mean amplitude.

The second method takes the signal corresponding to the time t_a and analyzes its second derivative along the chords. It identifies the extrema of the latter and compares their values to its standard deviation. The rapid variation of slope along the detectors observed at the transition between outside and inside chords can be thus detected. In order to remove the noise, an interpolation of the signal along the chords is taken with a small tension (value of 1 in the *Matlab interpos* function) for this analysis. If the analyzed signals come from the FFT filter, the amplitude signal is used as before.

The final set of chords is deduced by taking a rounded mean of the transition chord numbers given by both methods. Thus, we obtain a limiting chord on each side of the magnetic axis. This process is not accurate to more than one chord. Therefore, we take also both neighbors of the limiting chords. As the function *psitbxp2p* gives the smallest value of the normalised poloidal flux along each chord, it is then easy to determine a ρ_{min} for each

interesting chords and to finally obtain ρ_{lufs} by taking the mean value of the ρ_{min}'s. The error $\Delta\rho_{lufs}$ on ρ_{lufs} is simply calculated by taking the standard deviation of the ρ_{min}'s.

8.2.8 Fit A to a given radial limit

The routine that fits the value of A to the desired last perturbed flux surface ρ_{target} works as follows:

- For a given A, an island is generated.
- The corresponding flux coordinate of the last unperturbed flux surface, ρ_{max}, is calculated by finding the maximal value of $\psi_{p,01}$ in the zone covered by the island.
- The function *fminsearch* is used to find the value of A that minimizes $(\rho_{target} - \rho_{max})^2$.
- As the variation of ρ_{max} in function of A is weak, it happens quite often that *fminsearch* identifies flat zones (same values of ρ_{max} for different values of A) as minima. To avoid this behaviour, an independent test checks the result. If it fails, the routine is called in a closed loop with different initial values of A. The quality of the first approximation of A given to the routine is thus important.

8.3 Dictionary of the developed *Matlab* routines

We give here a dictionary of the *Matlab* routines developed within our project. Most of them can be called independently, but for each, the main calling routine is given.

A_by_rho finds the value of A that corresponds to a given maximal radial extension of the islands in flux coordinates (see section 8.2.8). It is called by **fit_real_isl**.

chi2_rhos returns a value of χ^2_{mean} for a given set of island parameters and signals coming from the SVD or the bandpass filters. It uses $\tilde{g}_1$, the rough approximation of g_1 (see section 4.10.4). It does not use the constraint on the phase shift. It is called by **fit_rhos**.

chi2_rhos_fft returns a value of χ^2_{mean} for a given set of island parameters and signals coming from the FFT filter. It uses $\tilde{g}_1$, the rough approximation of g_1 (see section 4.10.4). It is called by **fit_rhos**.

chi2_rhos_t uses $\tilde{g}_1$, the rough approximation of g_1, and the periodicity constraint. It is mainly used to obtain the first estimation of Φ_0 (see section 4.10.2). It is called by **fit_real_isl**.

chi2mean_A returns a value of χ^2_{mean} for a given set of island parameters. The signals come from the SVD or the bandpass filters. chi2mean_A also returns the fitted parameters. It uses $g_{1,approx}$, the fine approximation of g_1 (see section 4.10.5). It checks the input value of A. It is called by **fit_real_isl**.

chi2mean_A_fft returns a value of χ^2_{mean} for a given set of island parameters and signals coming from the FFT filter. It also returns the fitted parameters. It uses $g_{1,approx}$, the fine approximation of g_1 (see section 4.10.3). It checks the input value of A. It is called by **fit_real_isl**.

chi2mean_A_phase returns a value of χ^2_{mean} for a given set of island parameters and signals coming from the SVD or the bandpass filters. It also returns the fitted parameters. It uses g_1 (see section 4.10.2). It checks the input value of A. It is called by **fit_real_isl**.

data_preproc calls **mpxdata** to load the DMPX data and processes them as described in section 4.3. It is called by the filters, or by **filt_data**.

filt_data generates a data structure containing the raw data given by **data_preproc** or **gen_mpx_sig**, the filtered data, the time basis, the frequency basis and some other useful parameters. It is mainly called by **real_isl_prep**.

find_dR returns a value of d_p (see section 4.9.2) for a given modification of the poloidal flux. It is called by **mpx_inv_stat**.

FishSecMix solves equation (43) and returns the obtained stationary emissivity profile (see sections 4.9.1 and 8.2.6). It is called by **prof_inv**.

fit_real_isl fits A, Phi_0 and P for a given ρ_s using g_1 or $g_{1,appr}$ (see section 4.10). The input signals can come from all the filters. It is called by **fit_real_isl_all**.

fit_real_isl_all is the basic routine for the fit of the perturbation DMPX signals. It generates all the results. It is called by you!

fit_rhos returns the value of $\rho_{s,appr}$, the approximative value of ρ_s found with $\tilde{g}_1$. The input signals can come from all the filters. See section 4.10.4. It is called by **fit_real_isl_all**.

gen_mpx_sig generates a comprehensive DMPX phantom. It is called by **filt_data**.

gen_mpx_sig_statio generates a stationary DMPX phantom. It is called by **gen_mpx_sig** or **filt_data**.

gmapping returns the 2-D cylindrical coordinate stationary emissivity corresponding to a profile given as $g(\rho)$. It is called by **gen_mpx_sig_statio**.

integ_chords returns the integrals on the DMPX chords of a function defined on a poloidal cross-section. The geometry factor accounting for the slit of the DMPX is used. This routine is called by nearly everything.

isl_av returns the average of an island structure on the orientation. It is mainly called by **chi2mean_A_phase**.

isl_basis_fct returns the function g_r and g_i defined in equation (62). It is called by **chi2mean_A_fft**.

isl_constr calculates the stationary helical flux and the total helical flux for a given set of island parameters. It also isolates the islands and checks their size. It fits the grid cell dimensions to a specified island width. It is called in all the routines relative to **fit_real_isl**.

isl_width calculates the width of the islands and their extension in flux coordinates. It is called by **fit_real_isl**.

min_chi2 solves equation (43) with $\alpha = 0$. It is mainly used to obtain a value of χ^2_{target} (see sections 4.9.1 and 8.2.6). It is called by **FishSecMix**.

modif_pert returns the functions $\tilde{\psi}_c$ and $\tilde{\psi}_s$ of equation (55)(see section 4.10.2). It is called by **chi2_rhos** for instance.

mpx_inv_stat inverses the stationary DMPX profile and searches the best poloidal flux modification. It is called by **real_isl_prep**.

mpx_transf_mat calculates the transfer matrix **K** of equation (43) (see section 4.9.1). It is called by **prof_inv**.

mpxdata loads the calibrated DMPX signals and the DMPX geometry. It is called by **data_preproc**.

new_minfisher solves equation (43) with $\beta = 0$ and returns the obtained stationary emissivity profile (see section 4.9.1). It may be called by **prof_inv**.

pert_flux calculates the flux perturbation base functions ψ_c and ψ_s defined in equations (32) and (33) of section 3.4.

plas_grid redefines the grid on which the poloidal flux is defined. The grid may be set to be tangent to a desired flux surface, and the grid cell dimensions can be specified. It is called by **real_isl_prep** and **isl_constr**.

PO_fit solves equation (49) of section 4.10. It is called in many places.

prof_inv inverses the stationary DMPX profile. It is called by **mpx_inv_stat**.

real_isl_prep loads the filtered DMPX signals and the magnetic data. If required, it also searches the best modification of the poloidal flux. It determines the value of ρ_{lufs} (see section 8.2.7). It is called by **fit_real_isl_all**.

sig_fft corresponds to the block described in section 4.8. It is called by **filt_data**.

sig_filter corresponds to the block described in section 4.5. It is called by **filt_data**.

sig_SVD corresponds to the block described in section 4.6. It is called by **filt_data**.

sim_rot constructs an island structure corresponding to a specified width. It also simulates the DMPX signals produced by the rotation of this structure. It is called **gen_mpx_sig**.

SndOrdReg solves equation (43) without the Fisher object function and returns the obtained stationary emissivity profile (see section 4.9.1). It may be called by **prof_inv**.

time_sel corresponds to the block described in section 4.7. It is called by **filt_data**.

References

[1] M. Bessenrodt-Weberpals *et al.*, MHD activity as seen in soft X-ray radiation, Plasma Phys. Control. Fus., Vol. 38 (1996)

[2] R. S. Granetz, M. C. Borrás, Is X-ray emissivity constant on magnetic flux surfaces?, Fus. Eng. and Des., 34-35 (1997) 153-157

[3] L. C. Ingesson *et al.*, Soft X-ray tomography during ELMs and impurity injection in JET, Nucl. Fus., Vol. 38, No. 11 (1998)

[4] K. Myamoto, Plasma Physics for Nuclear Fusion, MIT Press, 1980

[5] H. Reimerdes, MHD stability limits in the TCV tokamak, Thèse 2399, EPFL, Lausanne, 2001

[6] A. L. Rosenberg *et al.*, Modeling of neoclassical tearing mode stability for generalized toroidal geometry, Phys. of Plasmas, Vol. 9, Nř 11 (2002)

[7] M. Schittenhelm *et al.*, Analysis of coupled MHD modes with Mirnov probes in ASDEX upgrade, Nucl. Fus., Vol. 37, No. 9 (1997)

[8] S. Yoshimura *et al.*, Investigation of coupling of MHD modes by soft X-ray computer tomography on the WT-3 tokamak, Phys. of Plasmas, Vol. 9, Nř 8 (2002)